Analysis and Design of Air-Core Transformer Based on Internal Magnetic Flux Density Distribution for High-Frequency Power Converter

Kazuki Hashimoto

Analysis and Design of Air-Core Transformer Based on Internal Magnetic Flux Density Distribution for High-Frequency Power Converter

A Dissertation

Presented to the Graduate School of Engineering

of Kyoto University

in Partial Fulfillment of the Requirements for the Degree of

Doctor of Philosophy

by

Kazuki Hashimoto

March 2021

Abstract

Transformers transfer electrical energy without a conductive connection between the two circuits or multiple circuits. The use of transformers in DC-DC converters not only provides isolation between the power source and the load, but also improves the flexibility of the power conversion system, for example, series-parallel connection of converters. One of the challenges is how to miniaturize the size of the transformers. Megahertz operation of power converters is a key technology for miniaturizing them. The size of the transformers governs the size of power converter, depending on the amount of the energy in a switching cycle. The high-frequency switching can reduce the energy stored in a switching cycle. Thus, megahertz operation permits to use smaller transformers in power converters.

In the frequency range above megahertz, air-core configurations in magnetic components have become the popular option. This is because the iron losses of the conventional magnetic materials such as Mn-Zn and Ni-Zn are not practically negligible in that frequency range. Since air-core magnetic components do not use a magnetic material, air-core magnetic components are free from magnetic material iron losses. The application of air-core magnetic components to high-frequency power converters has many challenging tasks that need to be solved. Among them, this dissertation investigates the high-frequency characteristics of the air-core transformer and their effects on the power conversion operation. The contribution of this dissertation is summarized as follows.

Firstly, the fundamental characteristics of the air-core transformer are analyzed on the basis of its frequency responses. The air-core transformer is fabricated by printed circuit boards (PCBs) and pin headers. In order to investigate the high-frequency characteristics, eight kinds of measurements are conducted. Several resonances are confirmed in the frequency range of several tens of megahertz. In addition, it is clarified that the high-frequency characteristics strongly depend on the air-core transformer structure. This supports the motivation of this dissertation to investigate the high-frequency characteristics and provides direction for the following investigations.

Secondly, the methods for the analysis of the air-core transformer are developed. The high-frequency equivalent circuit is derived from analogy with the coupled transmission lines. The air-core transformer is modeled as the distributed parameter model, which can consider the distribution of the physical quantity. The proposed equivalent circuit enables us to simulate the operation of power converters in the frequency range above megahertz. Then, the measurement method for the internal magnetic flux density distribution is presented. The magnetic flux density is measured with the fabricated search coil. The internal magnetic flux density distribution is measured and analyzed when the air-core transformer is excited by 1 MHz sinusoidal waveform. As a result, the validity of the measurement method is confirmed.

Thirdly, the behavior of the internal magnetic flux density under high-frequency switching conditions is investigated. The air-core transformer is excited by the triangle current, which includes many harmonic components. Since the air-core transformer has several resonant frequencies in several tens of megahertz, the measured waveforms oscillate at high frequency. The high-frequency oscillation shows a different distribution from the low-frequency oscillation. This implies that the behavior of the magnetic flux density changes at that frequency. The cause of the high-frequency oscillation is discussed, and it is found that the oscillation is caused by the second resonant frequency. Similar oscillation is also observed in the high-frequency flyback converter. It is found that the oscillation leads to the low power conversion efficiency. In order to improve the power conversion efficiency, the secondary circuit is modified, and the efficiency is improved by 20%. These results indicate that understanding the magnetic flux density as a vector quantity is important for designing high-frequency flyback converters.

Lastly, design guidelines for air-core transformers are presented on the basis of the investigations given by this dissertation.

Acknowledgments

First of all, I would like to express my most sincere gratitude to Professor Takashi Hikihara for his continuous and attentive supervision, invaluable advice and suggestions, and ceaseless encouragement through fruitful discussions. He gave me the opportunity to start the research of internal magnetic flux density, which I had never thought of measuring when I started my research. Moreover, he provided me many precious opportunities to grow up as a researcher.

I would also like to extend my gratitude to the members of my dissertation committee: Professor Tetsuji Matsuo and Professor Taketsune Nakamura. They gave me valuable comments and suggestions to improve this dissertation, and also provided me with opportunities for fruitful discussions.

I am especially obliged to Dr. Takafumi Okuda (Iwata Fukushima SiC Applied Engineering Inc.). He was a former staff in the laboratory, and his door was always open for discussions whenever questions arose and help was needed.

I would like to acknowledge all the former and current members of Advanced Electrical Systems Theory Laboratory, Kyoto University, for providing me with a comfortable research environment. In particular, present and former staff, including Assistant professor Shiu Mochiyama (Kyoto University), Associate Professor Ryo Takahashi (Kyoto University of Advanced Science), and Professor Alberto Castellazzi (Kyoto University of Advanced Science) offered helpful comments and valuable discussions, as well as encouragement. Ms. Yoshiko Deguchi helped my research activities with administrative support and warm encouragement. I would also like to thank all the students in the laboratory, which include Dr. Hikaru Hoshino, Dr. Shinya Nawata, Dr. Fredrik Raak, Dr. Manuel Antonio Sánchez Tejada, Dr. Toko Mannari, Ms. Rutvika Nandan Manohar, Mr. Seongcheol Baek, Mr. Naomitsu Yoshida, Mr. Shinji Katayama, Mr. Yuma Murakawa, and Mr. Yuki Araki for their supports and encouragement.

This work was supported in part by the Program on Open Innovation Platform with

Enterprises, Research Institute and Academia of Japan Science and Technology Agency, Cross-ministerial Strategic Innovation Promotion Program of New Energy and Industrial Technology Development Organization. This work was also supported by JST-OPERA Program Grant Number JPMJOP1841 and JSPS KAKENHI Grant Number 20H02151.

Last but not least I sincerely wish to thank my family and all of my friends for their understanding, support, and heartfelt encouragement.

Contents

Chapter 1

Introduction

A transformer is a passive component used to transfer electrical energy from one electrical circuit to another, or to multiple circuits. The history of a transformer dates back to 1831 in which Michael Faraday discovered "Faraday's law of induction," the fundamental operating principle of transformers [1]. The transformer consists of at least two coils. A varying current in any one coil produces a varying magnetic flux. The magnetic flux interlinking with any other coils induces a varying electromotive force across them. Thus, a transformer allows to transfer electrical energy without a conductive connection between the two circuits or multiple circuits. Transformers are used to isolate between circuits and to convert voltage or current. They are applied in a wide range of applications, from high to low power, and from commercial to RF frequencies. For example, they are used for voltage conversion in grids and for insulation of signal processing circuits. Since the invention of the first transformer in 1885 [2], transformers have become an indispensable part of electrical systems.

A DC-DC converter is one of the circuits in which a transformer plays an important role. The DC-DC converter is an electronic circuit that converts the voltage level of a DC source into another level [3]. The voltage and current for suitable operation differ depending on the load. The DC-DC converter solves that mismatch between the load and the power source. In recent years, there has been an increase in the number of electrical systems consisting of various power sources and loads, such as electric vehicles [4–6]. In such systems, isolation between circuits is often required to ensure safety and to manage the ground. The transformer gives the DC-DC converter isolation, and such a DC-DC converter is called an isolated DC-DC converter. The isolation provided by the transformer also allows the series-parallel configuration of DC-DC converters. A

series-parallel configuration is one in which the inputs or outputs of multiple low-power DC-DC converters are connected in series or parallel. The salient features include: 1) ease of selecting power devices; 2) increased overall system reliability; 3) shortened design process and lowered cost of system; 4) ease of capability expansion of power conversion system [7–10]. Thus, the transformer not only provides isolation to the DC-DC converter, but also improves the flexibility of the power conversion systems.

However, the size and weight of the transformer used in current DC-DC converters are one of the factors that prevent the construction of the system described above. In such a system, the number of required DC-DC converters increases as the number of types of power sources and loads or the number of series-parallel connection. This leads to the physical size of the system becoming huge, making it difficult to construct a practical system. Since transformers govern the size and weight of converters, high-frequency power converters have been investigated in order to reduce the size of DC-DC converters. Wide-bandgap power devices such as Silicon Carbide (SiC) and Gallium Nitride (GaN) are suitable for high-frequency DC-DC converters. That is because they have superior device characteristics such as high-withstand voltage, low on-resistance, high-frequency operation capability, and high-temperature durability, compared to silicon power devices [6, 11–16]. Thus, the switching frequency has been improved to megahertz range owing to them, leading to the miniaturization of DC-DC converters [17–29].

Still, the magnetic components such as transformers and inductors present difficult obstacles in achieving megahertz operation. One of the issues is the frequency characteristics of the conventional magnetic materials such as Mn-Zn and Ni-Zn. Conventional magnetic components employ magnetic materials of high-permeability, in order to confine the magnetic flux. However, they cannot be utilized in the megahertz-class operation because their iron losses are not practically negligible in the frequency above megahertz [30]. Air-core configurations in magnetic components become the popular option in the frequency range above megahertz because they are free from magnetic material iron losses. For this reason, many high-frequency power converters using air-core inductors and transformers have been reported [20, 31–40].

In this dissertation, we aim at developing the high-frequency power converter with an air-core transformer. Through implementing it in the power converter, design guidelines for air-core transformers are presented. In the rest of this chapter, detailed reviews on some key concepts of this dissertation are given. Section 1.1 introduces a flyback converter,

which is the power conversion circuit topology covered in this dissertation. Section 1.2 describes the miniaturization of power converters by high-frequency switching. In Section 1.3, the challenges for designing an air-core transformer are explained. Section 1.4 overviews the structure of the whole dissertation.

1.1 Flyback converter

This dissertation addresses the implementation of an air-core transformer in a flyback converter. The flyback converter is one of the isolated power converters. It has a wide range of applications such as consumer electronics, industrial electronics, communications equipment, and computers. Figure 1.1 shows a schematic of a flyback converter. It is equivalent to that of a buck-boost converter, with the inductor split to form a transformer. It consists of a transformer, an active switch, a diode, and an output capacitor.

Figure 1.2 shows the two configurations of a flyback converter in operation. The operation of the flyback converter during the on-time period (left of Fig. 1.2) is explained as follows. The primary of the transformer is directly connected to the input voltage source. The primary current and magnetic flux in the transformer increases, storing energy in the transformer. The diode is reverse-biased because the voltage in the secondary side in the transformer is negative. The output capacitor supplies energy to the load. When the active switch is turned off (right of Fig. 1.2), the primary current drops and the secondary voltage is positive. The diode is forward-biased, allowing current to flow from the transformer. The energy stored in the transformer recharges the capacitor and is supplied with the load. The voltage gain for the flyback converter is given by Eq. (1.1) from application of the volt-sec balance condition to the transformer.

$$\frac{V_\mathrm{o}}{V_\mathrm{i}} = \frac{D}{1-D}n \tag{1.1}$$

Where V_o denotes the output voltage, V_i the input voltage, D the duty ratio, and n the turns ratio.

The characteristics of a flyback converter are summarized as follows.

- Amenable to step-down and step-up configurations
- Simplicity of configuration with a minimum number of components
- Suitable for switching power supplies up to 100 W

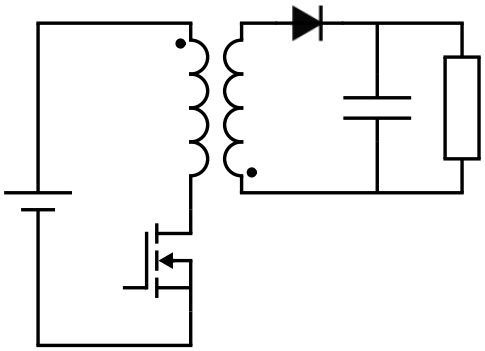

Figure 1.1: A schematic of flyback converter.

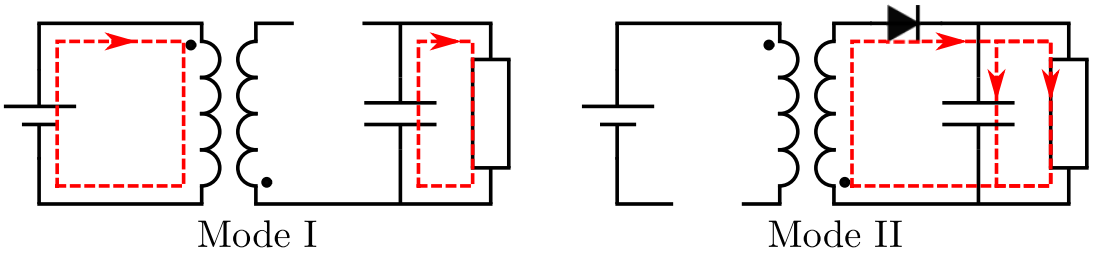

Figure 1.2: Schematics of two configurations of a flyback converter in operation: (a) on-state and (b) off-state.

The second feature is of great advantage for miniaturization and integration of power converters as compared with other isolated power converter topologies. In a series-parallel configuration, the simpler the individual converters are, the easier it is to reap the benefits of that configuration. This is why this dissertation investigates the flyback converter. This simple configuration is due to the fact that the transformer in the flyback converter plays multiple roles, including isolation, energy storage, and voltage/current conversion. A multi-output configuration can be also realized by increasing the number of transformer windings. Thus, the transformer is an important device in flyback converters, and the improvement of the transformer performance is a significant issue for the high-frequency operation of flyback converters.

1.2 Miniaturization of transformer by high-frequency switching

As mentioned above, the size of the power converter is governed by passive components such as inductors and capacitors. This section first describes the principle of the minia-

turization of power converters by high-frequency switching.

Figure 1.3 shows a photograph of the inside of a commercial AC adapter. The passive components are indicated by the red dotted circles. It can be seen that the passive components dominate the size of the power converter. In an inductor, its size mainly depends on the inductance and the current rating. The current rating is determined by the current rating of the switch. The large current rating makes the size of the inductor larger.

Here let us focus on the inductance. Figure 1.4 shows the photographs of three types of inductors. All of them have a current rating of more than 10 A. The inductance differs by up to 10 times. As the inductance decreases, the size of the inductor decreases. The inductance in the power converters is strongly related to the switching frequency. Triangular current flows through the inductor of power converters as shown in Figure 1.5. Suppose that the inductor current of the power converter is designed as shown in Figure 1.5(a). If the inductance is decreased, the ripple of the inductor current per switching becomes larger as shown in Figure 1.5(b). In this case, the current rating of the switch $i_{\mathrm{ds,lim}}$ is exceeded, and the power converter does not operate. Figure 1.5(c) shows the waveform of the inductor current when the switching frequency is increased with the same inductance as in Figure 1.5(b). An increase in the rate of the inductor current is the same as in Figure 1.5(b). However, the ripple is the same as in Figure 1.5(a) owing to the high switching frequency. This indicates that the high-frequency switching can decrease the inductance required by the power converter. As a result, the high-frequency switching leads to the miniaturization of the inductor. The above argument is also valid for transformers and capacitors.

However, as the switching frequency increases, frequency-dependent losses, such as iron losses in the core and copper losses in the windings (e.g., [41, 42]), cannot be practically negligible. These not only reduce the power conversion efficiency of the power converter, but in the worst case, the heat generation could lead to the inoperability of the power converter. How the effective size of the magnetic device varies with the switching frequency is a complex question. In [30], it is reported that how the inductor size varies with the switching frequency. It has been pointed out that cored AC inductors always have a frequency limit in terms of miniaturization by increasing the switching frequency. On the other hand, it has been shown that air-core designs can always make significant benefits in size, required energy storage, and magnetic losses by scaling up the frequency,

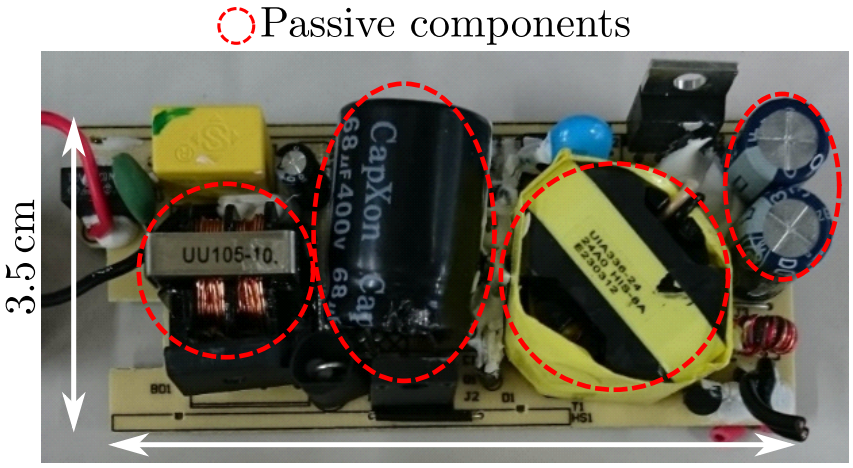

Figure 1.3: A photograph of inside of commercial AC adapter. The passive components are indicated by the red dotted circles.

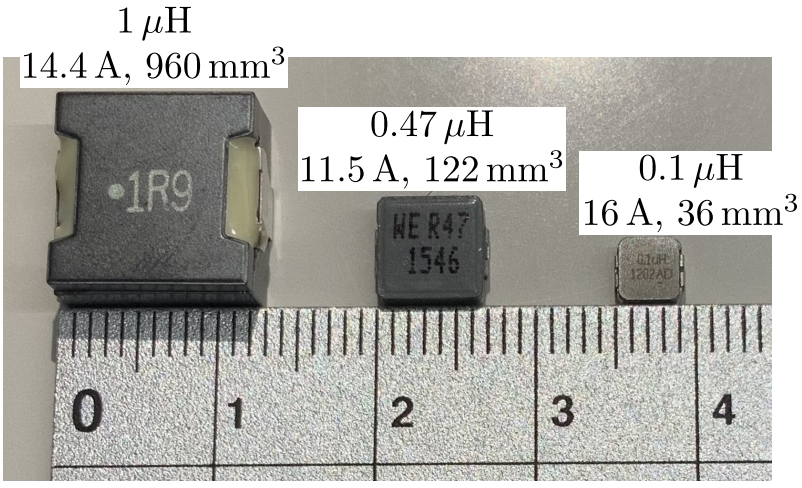

Figure 1.4: Photographs of inductors.

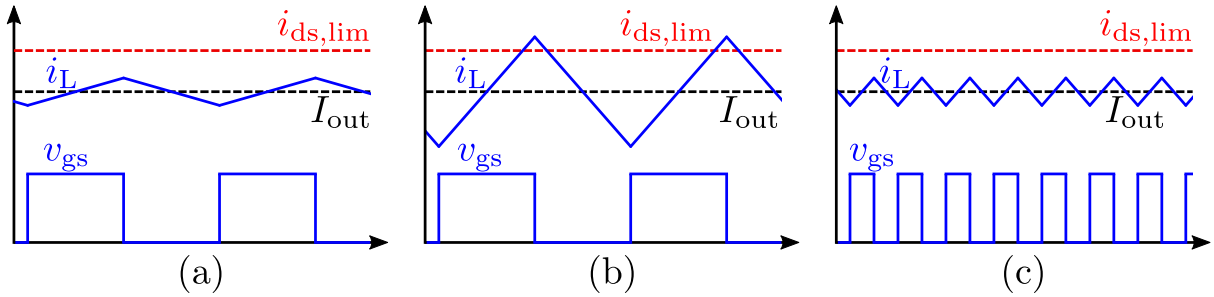

Figure 1.5: Schematics of waveform flowing through inductor: (a) low frequency and large inductance configuration, (b) low frequency and low inductance configuration, and (c) high frequency and low inductance configuration.

provided that sufficient high frequencies can be obtained within the constraints. Thus, this dissertation investigates an air-core transformer.

1.3 Challenges for designing air-core transformer

A large quantity of prior literature has studied the design of air-core inductors. In [43], the relationship between the toroidal structure and the inductance is investigated. Air-core toroidal inductor designs are optimized for maximum Q in [44]. In [32], various designs of toroidal air-core inductor utilizing a 3-D printing technique are presented. In analysis of the high-frequency characteristics, the parasitic capacitance between windings is investigated [45], and the inductor with electromagnetic shield is implemented [46].

In high-frequency power converters, zero-voltage switching (e.g., [37, 47–49]) is used to reduce the switching loss. The inductance and capacitance in the converter play an important role in these techniques because they utilize resonance. The parasitic components of switches and passive components are also included in design. The design of parasitic components of passive components is an important issue for high-frequency power converters. As reviewed above, air-core inductors have been widely discussed from low-frequency to high-frequency characteristics. However, the majority of the literature has placed little emphasis on air-core transformer designs, and few reports are available on their high-frequency characteristics. For low-frequency characteristics, the design tool for the air-core transformer [50] and the examples of its implementation in the high-frequency power converter [35] have been reported. Therefore, the purpose of this dissertation is to provide a design guideline for high-frequency characteristics of air-core transformers.

1.4 Overview of this dissertation

This dissertation addresses the analysis of an air-core transformer, with a particular focus on its high-frequency characteristics. As mentioned above, few reports are available on the high-frequency characteristics. Measurement and evaluation methods for the high-frequency characteristics have not been established. Therefore, in the first half of this dissertation, the evaluation methods for the high-frequency characteristics are developed. In the second half of this dissertation, the air-core transformer is implemented into a high-frequency flyback converter. Finally, through summarizing the studies in this dissertation, the direction for designing air-core transformers is presented. The rest of this section gives an overview of each chapter in this dissertation.

In Chapter 2, we investigate the fundamental characteristics of the fabricated air-core transformer based on their frequency responses. The device structure investigated in this dissertation is introduced. The different kinds of the air-core transformer are fabricated in order to discuss the relationship between the device structure and the frequency response. Through the comparison of their frequency responses, it is confirmed that the high-frequency characteristics strongly depend on the device structure. This provides the motivations and guidelines in the following chapters for the developments of the equivalent circuit and the measurement method.

In Chapter 3, we construct the high-frequency equivalent circuit of the air-core transformer. The equivalent circuit aims at representing the frequency response measured in Chapter 2. Since the high-frequency characteristics depend on the device structure, the air-core transformer is modeled as a distributed parameter model, which can consider the distribution of the physical quantity. In the first half of the chapter, we identify the dominant parasitic capacitance in the air-core transformer. This is obtained by comparison with the frequency response of the air-core inductor. In the second half, we derive the equivalent circuit from analogy with the coupled transmission lines. The validity of the equivalent circuit is confirmed through the circuit simulation.

In Chapter 4, we develop the measurement method for the internal magnetic flux density distribution in the air-core transformer. This dissertation focuses on the magnetic flux density in order to discuss the distribution of the physical quantity in the device. That is because the magnetic flux density is a key factor governing the performance of a transformer, in addition, it is difficult to measure the distribution of the voltage and cur-

rent owing to the measurement technique issues. The magnetic flux density is measured with the fabricated search coil. The magnetic flux density distribution is measured and analyzed when the air-core transformer is excited with 1 MHz sinusoidal wave. The effect of measurement equipment impedance is discussed. Through the analysis and discussion, we confirm the validity of the proposed measurement method under high-frequency switching conditions. The proposed method enables us to investigate the high-frequency characteristics.

In Chapter 5, we analyze the behavior of the internal magnetic flux density under the high-frequency switching conditions. This chapter focuses on the high-frequency oscillation observed in Chapter 4. After comparison with the air-core inductor, we confirm that the high-frequency oscillation is unique to the air-core transformer. The behavior of the magnetic flux density changes in the high-frequency oscillation. Specifically, the magnetic flux density near the secondary winding becomes larger than that near the primary winding. The cause of the high-frequency oscillation is discussed by the comparison of the magnetic flux density with the frequency response.

In Chapter 6, we design the high-frequency flyback converter with the air-core transformer. The active clamp flyback converter is introduced in order to handle the energy owing to the leakage flux. The input-output characteristics is measured, and the cause of the low power conversion efficiency is discussed based on the analysis of the search coil voltage. The secondary circuit is modified to improve the power conversion efficiency. As a result, the power conversion efficiency is increased by more than 20%. The behavior of the internal magnetic flux density is discussed in the active clamp flyback converter. The rotating magnetic flux density is confirmed, and it is found that the area of its trajectory corresponds to the amount of the output power. This shows the importance of investigating the magnetic flux density as a vector quantity in the design of air-core transformers for high-frequency power converter applications.

Chapter 2

Fundamental characteristics of air-core transformer

This chapter investigates the fundamental characteristics of the air-core transformer based on its frequency response. The fundamental operation of transformers is governed by the magnetic flux. Behaviors of magnetic flux are expressed by self-inductance and mutual inductance in circuit theory. These inductances are obtained from low-frequency characteristics. As is mentioned in Chapter 1, the analysis of the high-frequency characteristic is also important for designing high-frequency power converter applications. This dissertation aims at designing the high-frequency flyback converter which operates at 5 MHz in Chapter 6. If the air-core transformer has a resonant frequency at several tens of megahertz, we have to consider it to design the flyback converter because the operation waveforms include many harmonics. This dissertation discusses the high-frequency characteristics ranging up to 110 MHz.

In Section 2.1, the structure of the fabricated air-core transformer is explained. In order to discuss the relationship between the device structure and the frequency response, different kinds of the air-core transformer are fabricated. Then, in Section 2.2, the measurement setup is described. In Section 2.3, we discuss the frequency responses of the fabricated air-core transformer.

2.1 Device structure

This dissertation investigates the air-core transformer with a toroidal topology, which is suitable for confining the magnetic flux. Figure 2.1 shows the schematic of the fabricated air-core transformer and the photograph of its top view. The air-core transformer is

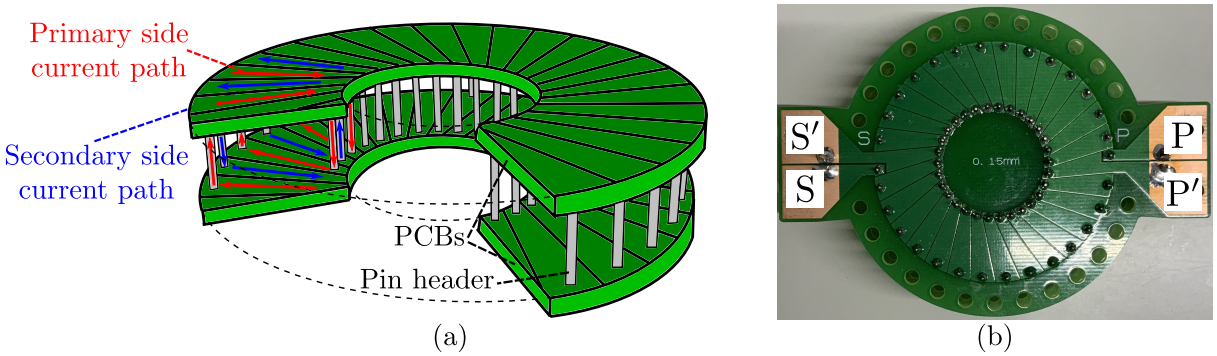

Figure 2.1: Fabricated air-core transformer: (a) schematic diagram and (b) photograph of top view.

Table 2.1: List of physical dimensions and number of turns for air-core transformer

Parameter	Value
Outer diameter [mm]	50.0
Inner diameter [mm]	24.0
Height [mm]	11.2
Number of turns per winding	15

fabricated by printed circuit boards (PCBs) and pin headers. The windings of the air-core transformer are wound so that the secondary winding is interleaved between the primary winding. Therefore, the air-core transformer has a symmetrical structure, viewed from each terminal. The physical dimensions and the number of turns are explained in Table 2.1. These parameters are kept fixed.

In order to investigate the relationship between the device structure and the frequency response, the air-core transformers with varying copper coverage and relative angle between the terminals were fabricated. A magnetic component needs to confine magnetic flux inside to prevent unnecessary coupling with surrounding components and wiring. The copper coverage is associated with confining magnetic flux. In this dissertation, the copper coverage is defined as the amount of the air-core transformer covered by the PCBs and pin headers. Figure 2.2 shows the schematic of the relationship between the magnetic flux and the device structure. In a toroidal structure, the magnetic flux occurs by the current flowing through the PCBs and pin headers. The magnetic flux of a toroidal transformer ideally exists only on the inside. Focusing on the magnetic flux associated with the PCBs, two types of magnetic flux occur as shown in Fig. 2.3. One is the magnetic flux that passes through the slit, and the other is the magnetic flux that dissipates in

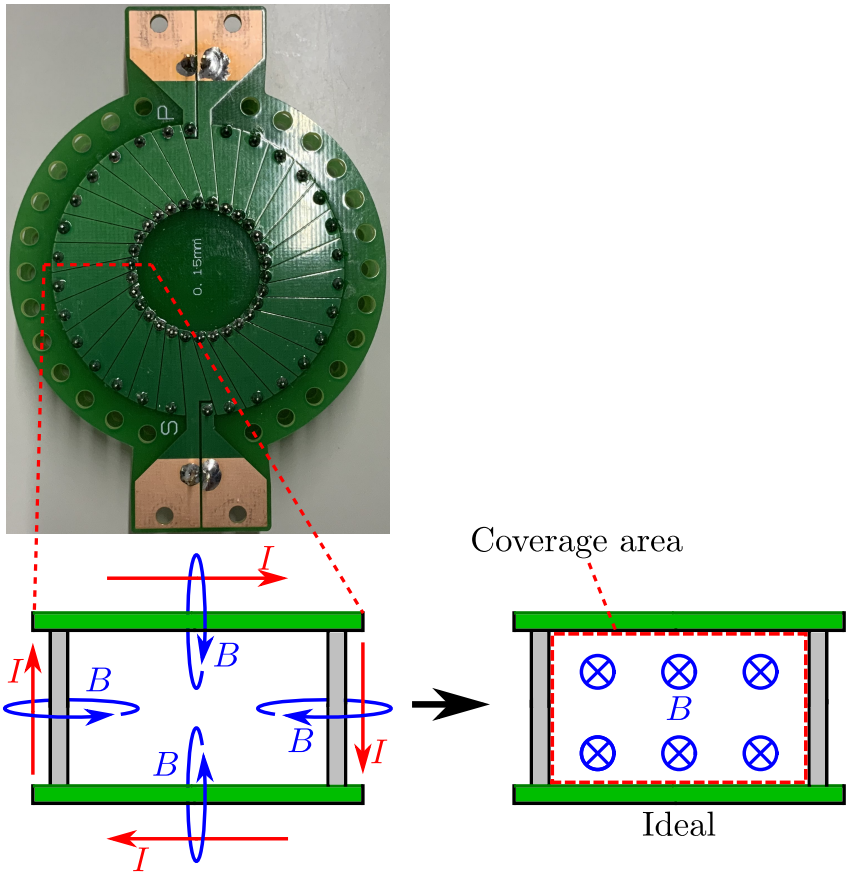

Figure 2.2: A schematic of relationship between magnetic flux and device structure.

the PCBs as eddy currents. The magnetic flux leaking to the outside increases when the slit width is increased. Since the magnetic flux leaking to the outside could be coupled to the surrounding components, it is better to reduce it as much as possible. However, an increase in the copper coverage leads to an increase in the parasitic capacitance between windings. Since this is related to the high-frequency characteristics, it is necessary to investigate it systematically. This dissertation focuses on the copper coverage of the PCBs. The copper coverage was modified by changing the slit widths of the upper and lower PCBs. When the slit width is increased, the copper coverage decreases. When the slit width is decreased, the copper coverage increases. We measure the frequency responses for each air-core transformer with five different slit widths (0.15, 0.3, 0.5, 0.7, and 0.9 mm). As examples, Fig. 2.4 shows the photographs of the top view in the fabricated air-core transformer with the slit width of 0.15 and 0.9 mm. The air-core transformers with varying the slit widths are fixed at the relative angle of 180 deg.

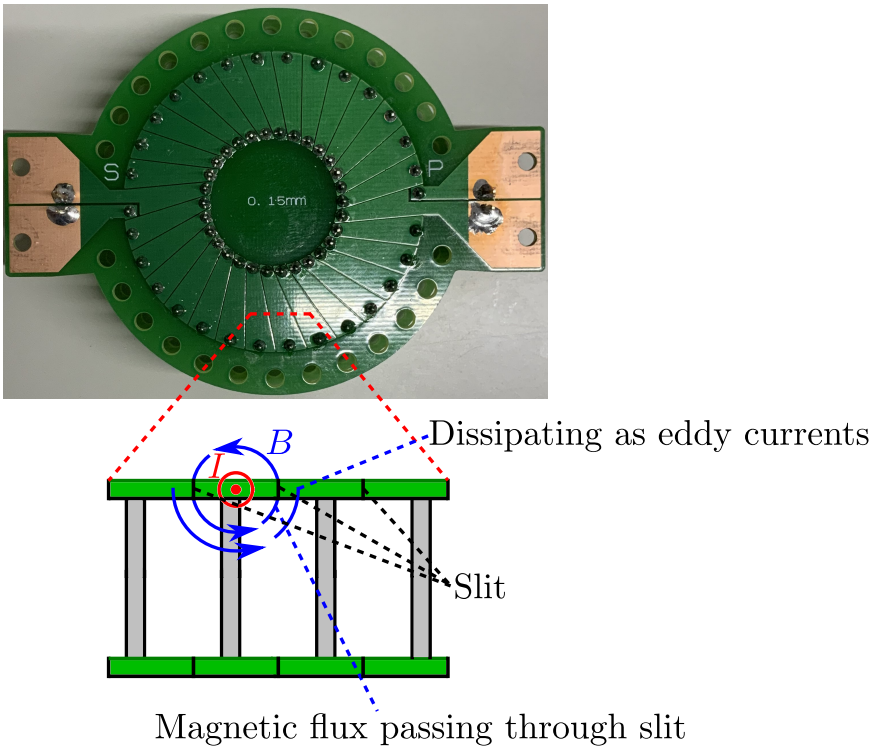

Figure 2.3: A schematic of relationship between magnetic flux and slit in PCBs.

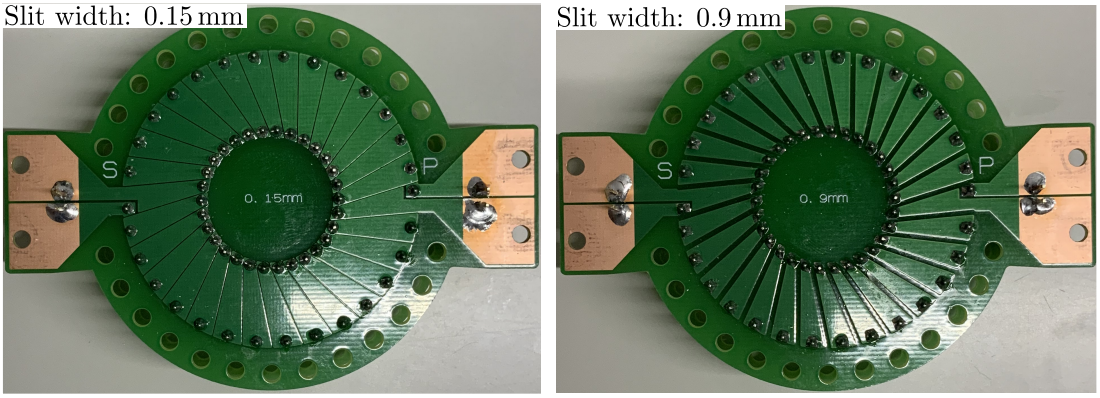

Figure 2.4: Photographs of top view of air-core transformer with different slit width. The left photograph shows the air-core transformer with 0.15 mm slit width, and the right one the air-core transformer with 0.9 mm slit width.

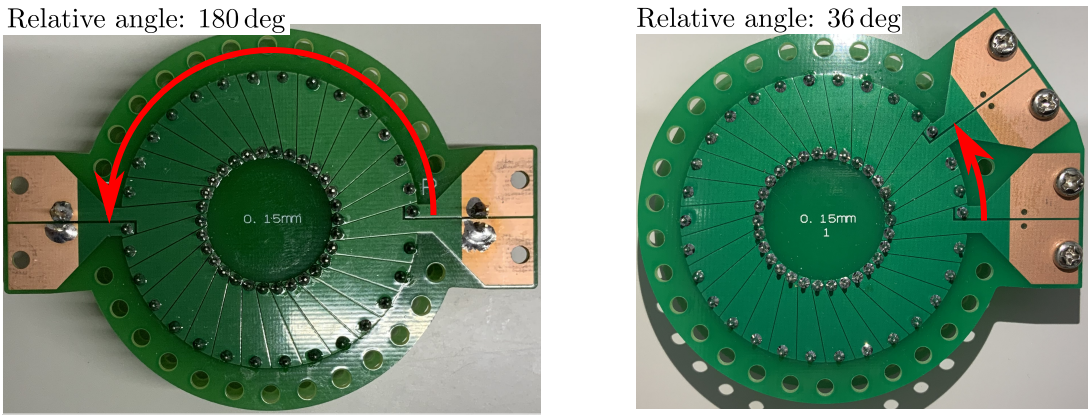

Figure 2.5: Photographs of top view of air-core transformer with different relative angle between terminals. The left photograph shows the air-core transformer with 180 deg relative angle, and the right one the air-core transformer with 36 deg relative angle.

Then, let us move on to the description of the relative angle between terminals. Since the placement of each component must be considered for miniaturization, it is necessary to change the position of the primary and secondary winding terminals. The wavelength-dependent phenomena such as $\lambda/4$ resonance occur in the high-frequency region. These phenomena strongly depend on the device structure because they are caused by the distribution of the physical quantities in the device. In the air-core transformer, the relative angle could become one of the factor. For this reason, changing the terminal position could affect the high-frequency characteristics. The relative angle between the terminals corresponds to the consideration. The relative angle was changed as shown in Fig. 2.5. We measure the frequency responses for each air-core transformer with six different relative angles (36, 60, 84, 108, 132, and 156 deg). The air-core transformers with varying the relative angle are fixed at the slit width of 0.15 mm.

2.2 Measurement setup

The frequency responses are measured using an impedance analyzer (Keysight Technologies, 4294A, measurable frequency range: 40 Hz to 110 MHz) with a test fixture (Keysight Technologies, 16047E). Open and short calibrations are performed accordingly. The air-core transformers are excited in the frequency range from 0.1 to 110 MHz, and the number of measured points is set to 801.

Figure 2.6 shows the schematics of the measurement setup. We measure eight kinds of

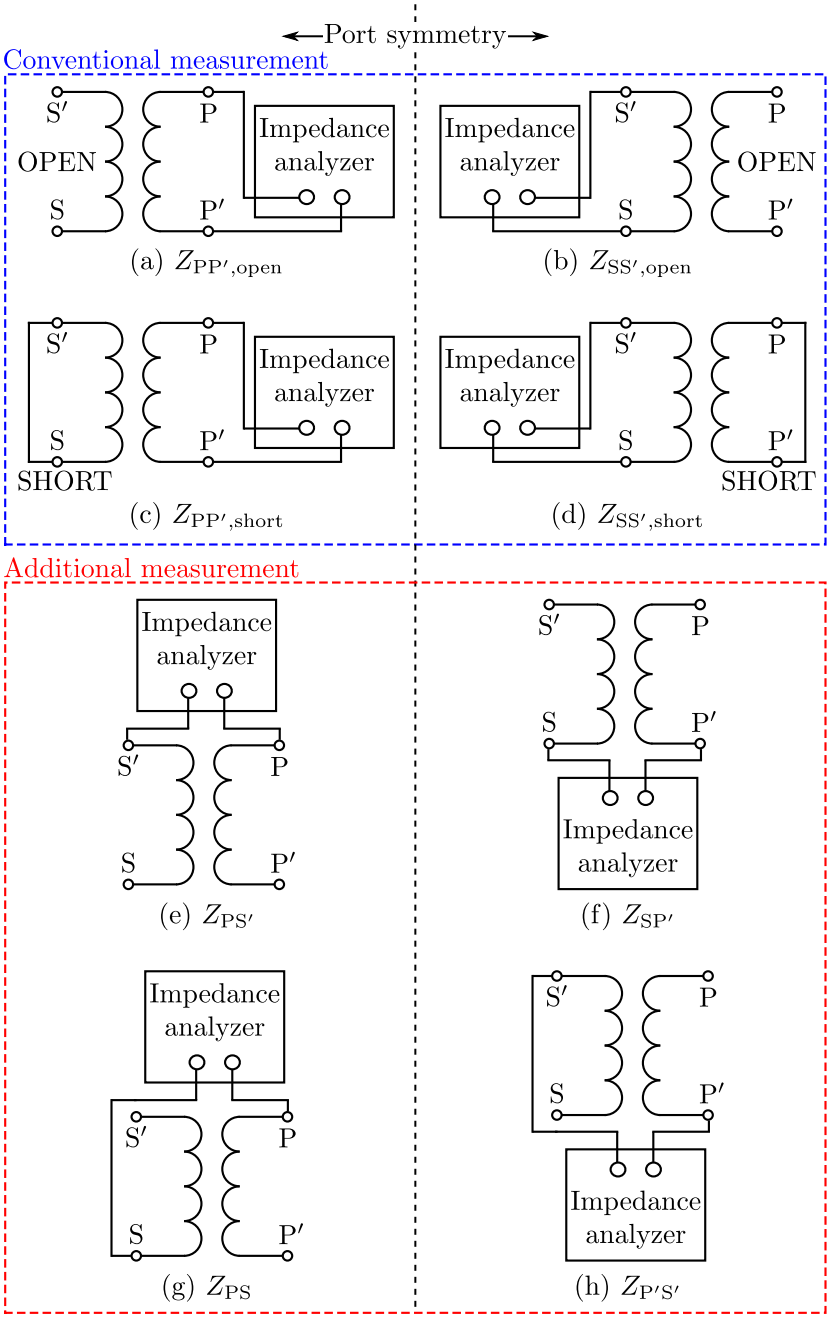

Figure 2.6: Measurement setup schematics.

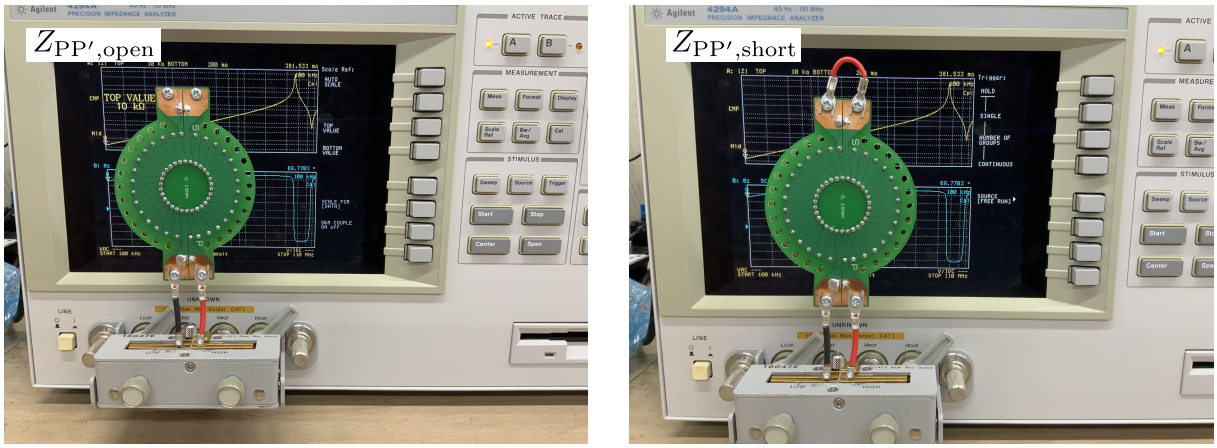

Figure 2.7: Photographs of measurement for frequency response of air-core transformer. The left photograph shows the measurement for $Z_{\mathrm{PP'},\mathrm{open}}$, and the right one the measurement for $Z_{\mathrm{PP'},\mathrm{short}}$.

frequency responses for each air-core transformer. The frequency response in Fig. 2.6(b) is measured from the opposite port in Fig. 2.6(a). These frequency responses are essentially the same measurements because the transformer structure is symmetrical. Similarly, Fig. 2.6(c) corresponds to (d), Fig. 2.6(e) to (f), and Fig. 2.6(g) to (h). Figures 2.6(a) to (d) show the conventional measurement setup to estimate the self-inductance and mutual inductance in a transformer. The others are the additional measurement for evaluating the high-frequency characteristics of the air-core transformer. Figure 2.7 shows the photographs of the frequency response measurement. The air-core transformer was connected to the test fixture with wires. For the measurement such as $Z_{\mathrm{PP'},\mathrm{short}}$, the terminal was shorted with a wire.

2.3 Measured frequency response

Herein, we discuss the frequency response of the air-core transformer. We first investigate the air-core transformer which has the slit width of 0.15 mm and the relative angle of 180 deg. Figure 2.8 shows the frequency responses of the air-core transformer. The impedances of the relationships described in Section 2.2, such as $Z_{\mathrm{PP'},\mathrm{open}}$ and $Z_{\mathrm{SS'},\mathrm{open}}$, are shown with the blue and red lines in the same figure. It can be seen that the blue line is identical to the red line in every figure. This shows that the air-core transformer is symmetrical for the measured port. Hereinafter, we consider the measurement based on $Z_{\mathrm{PP'},\mathrm{open}}$, $Z_{\mathrm{PP'},\mathrm{short}}$, $Z_{\mathrm{PS'}}$, and Z_{PS}.

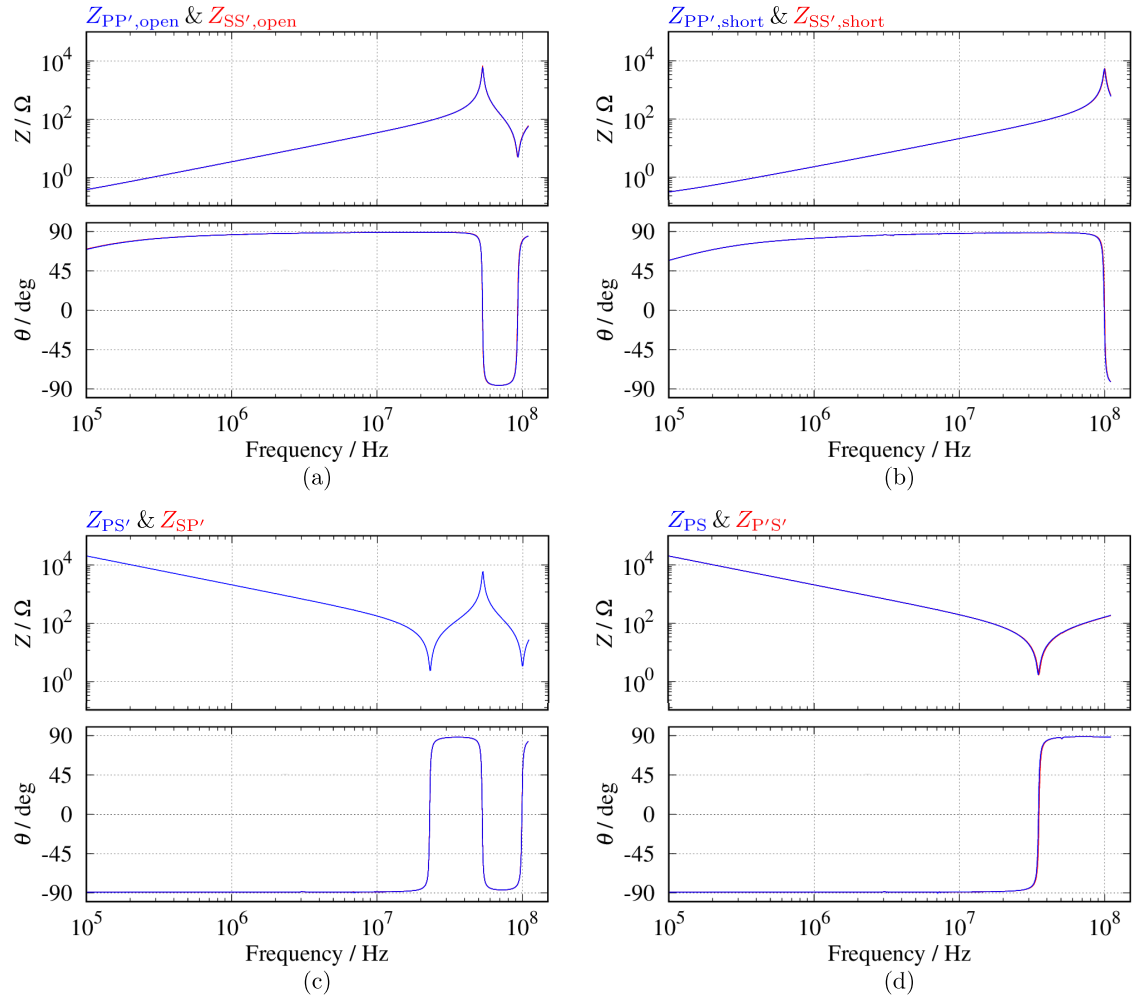

Figure 2.8: Measured frequency responses of air-core transformer: (a) $Z_{PP',open}$, $Z_{SS',open}$, (b) $Z_{PP',short}$, $Z_{SS',short}$, (c) $Z_{PS'}$, $Z_{SP'}$, and (d) Z_{PS} and $Z_{P'S'}$. The slit width is set at 0.15 mm, and the relative angle between terminals at 180 deg. The impedances are shown with the blue and red lines.

In Figs. 2.8(a) and (b), it is seen that $Z_{PP',open}$ and $Z_{PP',short}$ are linearly increased with reference to logarithm of the frequency range below 10 MHz. These phases are about 90 deg. These impedances correspond to the inductance components of the air-core transformer. Hereinafter, the inductance component obtained from $Z_{PP',open}$ is referred to as $L(Z_{PP',open})$, and the inductance component obtained from $Z_{PP',short}$ to as $L(Z_{PP',short})$. In Figs. 2.8(c) and (d), it is seen that $Z_{PS'}$ and Z_{PS} are linearly decreased with reference to logarithm of the frequency range below 10 MHz, and the phases are constant at -90 deg. These impedances correspond to the capacitance components of the air-core transformer. Hereinafter, the capacitance component obtained from $Z_{PS'}$ is referred to as $C(Z_{PS'})$, and

the capacitance component obtained from Z_{PS} to as $C(Z_{\mathrm{PS}})$.

In the frequency range above 10 MHz, several resonances are confirmed. These resonances show that the transformers are affected by the parasitic capacitance. As mentioned at the beginning of this chapter, this result implies that we have to consider the resonant frequency to design the flyback converter if the air-core transformer is implemented into the megahertz power converter. In design theory of power converters, the characteristics of each component is assumed to be ideal. In transformers, the resonance does not appear in their frequency response because the parasitic capacitance is not considered. That is, the effect of the resonance is not taken into account in the design theory. The converter operation would vary from what is designed in advance owing to the resonance because the operation waveforms include many harmonic components. If the relationship between the device structure and the resonant frequency can be clarified, it could be useful for designing filters and determining the critical operating frequency of converters.

2.3.1 Copper coverage dependence

Figure 2.9 shows the change in the frequency responses as the copper coverage is changed. The estimated parameter values in the frequency range below 10 MHz are listed in Table 2.2. The parameter values are estimated in the frequency range below 10 MHz with the least-squares method. $L(Z_{\mathrm{PP'},\mathrm{open}})$ and $L(Z_{\mathrm{PP'},\mathrm{short}})$ do not change for the copper coverage. We can also confirm it from Fig. 2.9 because the all impedances are identical in the frequency range below 10 MHz. This implies that $L(Z_{\mathrm{PP'},\mathrm{open}})$ and $L(Z_{\mathrm{PP'},\mathrm{short}})$ do not depend on the copper coverage. In other words, the copper coverage does not play a significant role in the design of the self-inductance and mutual inductance.

It can be seen that $C(Z_{\mathrm{PS'}})$ and $C(Z_{\mathrm{PS}})$ change for the copper coverage in the frequency range below 10 MHz. The estimated capacitance component is different by a factor of about 2 between 0.15 and 0.9 mm slit width. This implies that the parasitic capacitance in the air-core transformer strongly depends on the copper coverage. In the high-frequency characteristics, several resonances are confirmed. In particular, $C(Z_{\mathrm{PS'}})$ shows three resonant frequencies. Multiple resonances do not appear in a pair of the inductance and capacitance. It indicates that the air-core transformer is a system with multiple combinations of the inductance and capacitance. The resonant frequency becomes low with increasing $C(Z_{\mathrm{PS'}})$ and $C(Z_{\mathrm{PS}})$ in every figure. The resonant frequency qualitatively becomes low when the inductance is constant and the capacitance becomes

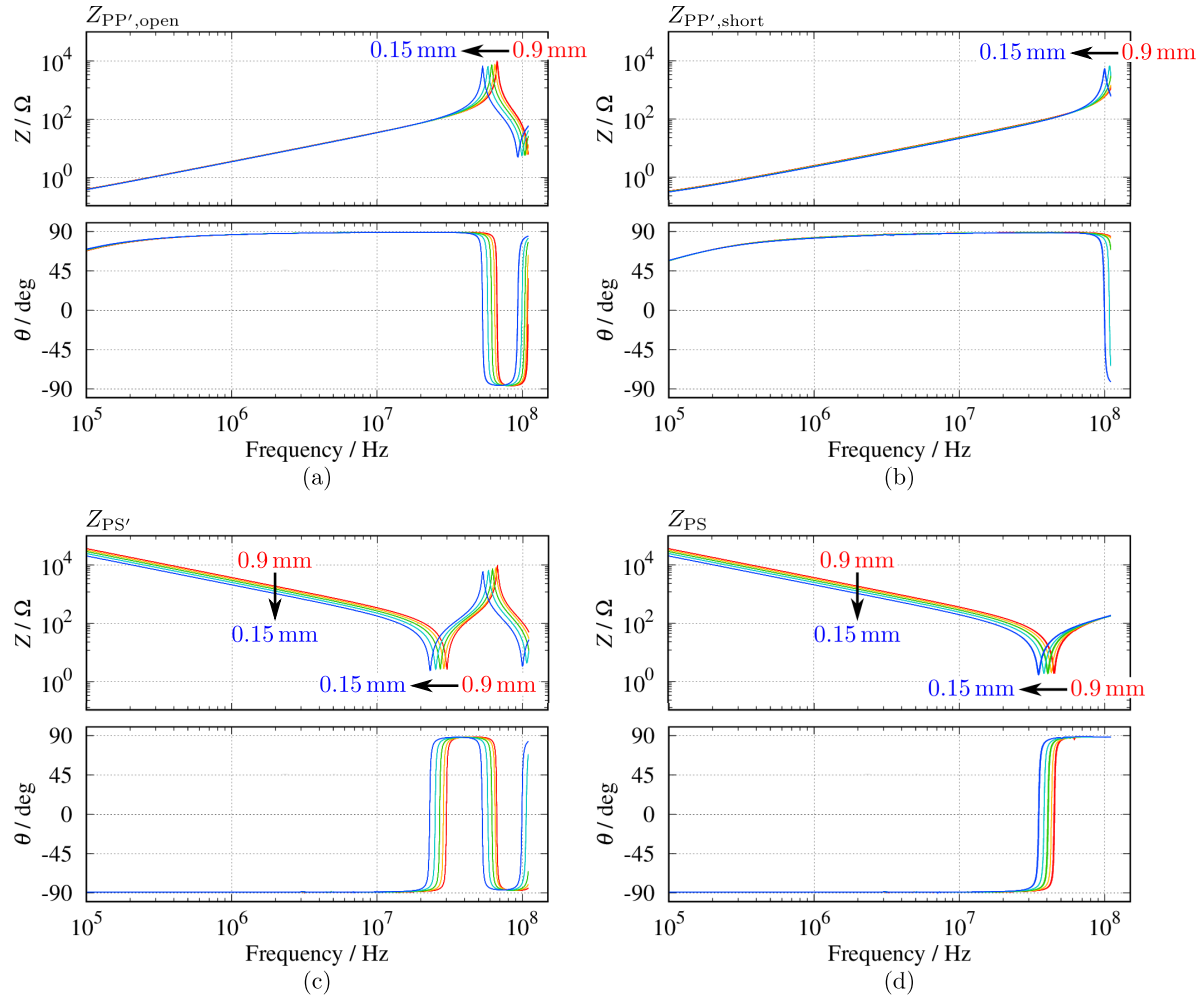

Figure 2.9: Measured frequency responses of air-core transformer: (a) $Z_{PP',open}$, (b) $Z_{PP',short}$, (c) $Z_{PS'}$, and (d) Z_{PS}. The slit width is set at 0.15 to 0.9 mm, and the relative angle between terminals at 180 deg.

Table 2.2: List of estimated parameter values of air-core transformer with different copper coverage

Parameter	Slit width [mm]				
	0.15	0.3	0.5	0.7	0.9
$L(Z_{PP',open})$ [nH]	547	548	553	555	564
$L(Z_{PP',short})$ [nH]	340	349	328	321	322
$C(Z_{PS'})$ [pF]	76.7	63.4	54.2	48.0	43.0
$C(Z_{PS})$ [pF]	76.8	63.3	54.2	48.0	43.0

large. The measurement results are consistent with the estimated values. This result supports the validity of the measurement in this chapter. Since $C(Z_{\mathrm{PS}'})$ and $C(Z_{\mathrm{PS}})$ depend on the copper coverage and change the high-frequency characteristics, the copper coverage plays a significant role for the design of the high-frequency characteristics.

2.3.2 Relative angle between terminalas dependence

Figure 2.10 shows the change in the frequency responses as the relative angle is changed between the terminals. The estimated parameter values in the frequency range below 10 MHz are listed in Table 2.3. As with the copper coverage case, $L(Z_{\mathrm{PP}',\mathrm{open}})$ and $L(Z_{\mathrm{PP}',\mathrm{short}})$ do not change for the relative angle. $C(Z_{\mathrm{PS}'})$ and $C(Z_{\mathrm{PS}})$ also do not change for the relative angle, unlike the copper coverage case. These results imply that the low-frequency characteristics in the air-core transformer do not depend on the relative angle between terminals. In other words, the relative angle does not play a significant role in the design of the low-frequency characteristic.

On the other hand, the frequency responses in the frequency range above 10 MHz change for the relative angle except for $Z_{\mathrm{PP}',\mathrm{short}}$, although the low-frequency characteristics is identical for the all relative angles. This implies that the layout of the terminals must also be considered in the air-core transformer discussed in this dissertation. As the device dimension approaches the wavelength, the resonance occurs owing to the non-uniformity of the physical quantity in the device. The winding length of the air-core transformer is calculated to be 0.741 mm. It corresponds to about a quarter of the wavelength at 100 MHz. Since PCB includes a dielectric substance, the practical wavelength is shorted further. This implies that the resonance occurs in the frequency range several tens of megahertz. The change of the resonant frequency indicates that the physical quantity distribution changes owing to varying the relative angle. Therefore, these results indicate that it is necessary for the analysis of the high-frequency characteristics to consider the distribution of the physical quantity such as current and voltage in the air-core transformer.

The frequency responses in $Z_{\mathrm{PP}',\mathrm{short}}$ do not change for the relative angle. Since the terminal is shorted in the measurement of $Z_{\mathrm{PP}',\mathrm{short}}$, the secondary winding becomes a closed winding. For that reason, even if the relative angle changes, the same winding appears to be coupled from the primary side. This is also obvious based on the high-frequency equivalent circuit of the air-core transformer introduced in Chapter 3.

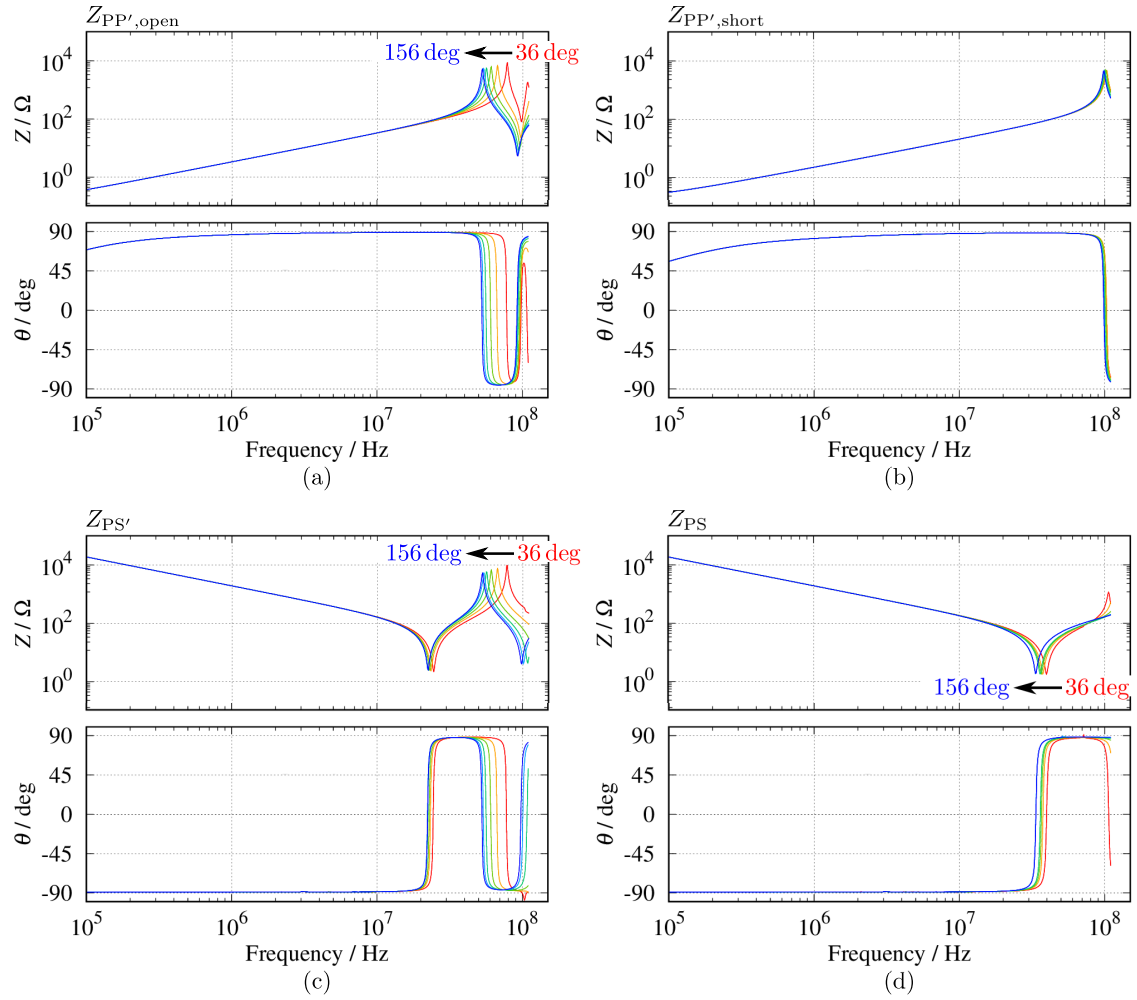

Figure 2.10: Measured frequency responses of air-core transformer: (a) $Z_{PP',open}$, (b) $Z_{PP',short}$, (c) $Z_{PS'}$, and (d) Z_{PS}. The slit width is set at 0.15 mm, and the relative angle between terminals at 36 to 156 deg.

Table 2.3: List of estimated parameter values of air-core transformer with different relative angles

Parameter	Relative angle [deg]					
	36	60	84	108	132	156
$L(Z_{PP',open})$ [nH]	529	530	530	533	534	533
$L(Z_{PP',short})$ [nH]	323	324	326	328	330	330
$C(Z_{PS'})$ [pF]	83.1	83.3	82.5	83.1	83.3	83.1
$C(Z_{PS})$ [pF]	83.4	83.6	82.6	83.3	83.4	83.4

2.4 Summary

This chapter analyzed the fundamental characteristics of the fabricated air-core transformer based on the measured frequency responses. In particular, to apply the air-core transformer to high-frequency power converters, we focused on the analysis of the high-frequency characteristics. First, the device structure was explained. To investigate the relationship between the device structure and the frequency response, the air-core transformers with varying copper coverage and relative angle between the terminals were fabricated. Then the measurement setup was described. In addition to the conventional measurements for estimating the self-inductance and mutual inductance, four additional measurements were conducted in this dissertation. Lastly, we discussed the measured frequency responses. The obtained frequency responses showed the port symmetry, copper coverage dependence, and relative angle between the terminals dependence. These results indicate that the high-frequency characteristics of the air-core transformer must be investigated considering the distribution of the physical quantity.

Chapter 3

High-frequency equivalent circuit of air-core transformer

In this chapter, we construct the high-frequency equivalent circuit of the air-core transformer, which is able to represent the frequency response shown in Chapter 2. Many nonlinear devices, such as MOSFETs and diodes, are used in converters. The use of circuit simulation is indispensable for the analysis and design of converters. There have been many studies on the models of MOSFETs and diodes considering the parasitic components for circuit simulation [51–56]. On the other hand, the transformer model only considering the self-inductance and mutual inductance is often used. This dissertation's air-core transformer has several resonances in the frequency range of several tens of megahertz. These resonances do not appear in the model that considers only the self-inductance and mutual inductance. Since these resonances could affect the converter operation, it is necessary to evaluate these effects beforehand by circuit simulation. Therefore, the high-frequency equivalent circuit of the air-core transformer is indispensable for the design of high-frequency power converters by circuit simulation.

From the results of Chapter 2, it is found that the high-frequency characteristics of the air-core transformer depend on its parasitic capacitance. This result indicates that the equivalent circuit needs to take into account the parasitic capacitance, which is one of the parasitic components. Transformers are modeled by the self-inductance and mutual inductance in the low-frequency region. There are several types of equivalent circuits [57–59]. These equivalent circuits do not consider the parasitic capacitance. In the frequency ranging up to several hundred kilohertz, the equivalent circuits considering the parasitic capacitance are derived on the basis of the resonant frequencies or the electrostatic energy

stored in the transformer [60–66]. These equivalent circuits are the lumped model. The lumped model is based on the assumption that the physical quantities such as voltage and current distribute uniformly in the windings. The parasitic capacitance in transformers distributes along the windings. Since the inductance also distributes along the windings, the transformer windings essentially form an LC ladder circuit. An LC ladder circuit shows the non-uniformity of the voltage and current depending on the excitation frequency. The above-mentioned assumption would not be satisfied with the high-frequency analysis in which the wavelength-dependent phenomena cannot be neglected. In addition, in Chapter 2, it is found that the high-frequency characteristics of the air-core transformer depend on the distribution of the physical quantity. This implies that they are dominated by the wavelength-dependent phenomena. Therefore, the lumped model is not suitable to investigate the high-frequency characteristics of the air-core transformer.

On the other hand, the distributed model takes into account the spatial and the time variation of the voltage and current. This model allows us to discuss the non-uniformity of the voltage and current distribution in windings. The distributed model of the transformer is crucial to investigate the non-uniformity in addition to the wavelength-dependent phenomena. Therefore, we aim at constructing the distributed model of the air-core transformer.

Based on the above points, we first discuss the modeling direction in Section 3.1. In Section 3.2, the parameter estimation method is described, and the modeling parameter related to the parasitic capacitance is identified. In Section 3.3, the high-frequency equivalent circuit is derived from analogy with the coupled transmission lines. The validity of the derived equivalent circuit is confirmed through the comparison of the measured results with the circuit simulation in Section 4.4.

3.1 Modeling direction

There have been many studies on how to construct a circuit network that reproduces the desired frequency response [67, 68]. These methods use the high-frequency characteristics such as resonant frequency. The physical correspondence between the network and the actual device is unclear although these methods allow us to easily construct a circuit network from the frequency response. We construct the equivalent circuit in which the physical relationship to the air-core transformer is clarified. This section discusses the

parameters which is necessary to construct an equivalent circuit based on the frequency response. There are given as follows.

- Inductance components
  - Self-inductance: L_{p} & L_{s}
  - Mutual inductance: L_{m}
- Capacitance components
  - Winding self capacitance: C_{p} & C_{s}
  - Winding-to-ground capacitance: C_{pg} & C_{sg}
  - Mutual capacitance: C_{m}

The inductance components of the air-core transformer are modeled by the self-inductance and mutual inductance. From the result of Chapter 2, the primary and secondary winding self-inductance is set to be the same value in the equivalent circuit because the air-core transformer has the symmetry structure. The components of the inductance are estimated from the conventional measurements. The details are described in Section 3.2.1.

The high-frequency characteristics change depending on the copper coverage and relative angle between terminals. The copper coverage implies that the parasitic capacitance has to be considered in the equivalent circuit. Assuming that the parasitic capacitance distributes along the windings, the parasitic capacitance is illustrated as shown in Fig. 3.1. The transformer's parasitic capacitances are classified into three types of capacitances, which are the mutual capacitance C_{m}, winding self capacitances, C_{p} and C_{s}, and winding-to-ground capacitances, C_{pg} and C_{sg}. If all capacitances are taken into account in the distributed model, the equivalent circuit becomes complex. In particular, it is difficult to separate these three on the basis of the impedance obtained from windings. Therefore, for constructing the equivalent circuit, it is important to identify the dominant parasitic capacitances in the applied frequency range. The details are described in Section 3.2.2.

The relative angle requires a clear relationship between the topology of the equivalent circuit and the relative angles. If the air-core transformer is represented by the distributed model, the equivalent circuit is constructed by taking into account the winding length. In other words, since the equivalent circuit considers the concept of spatial variation, the change in the relative angles between terminals can be represented by the change in the circuit topology. The above approach cannot be used for the lumped model. In the

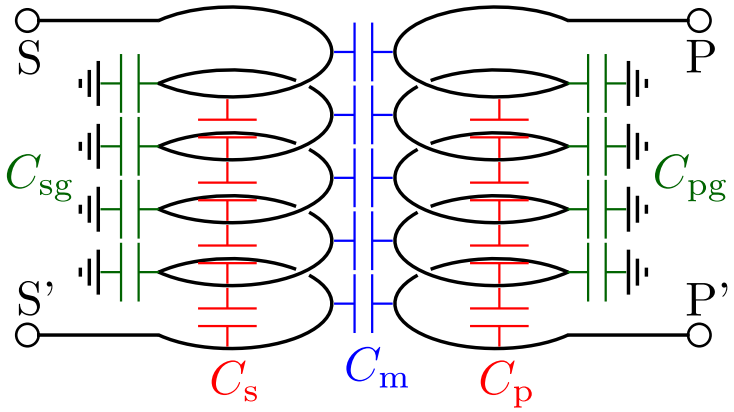

Figure 3.1: A schematic of parasitic capacitance in transformer.

lumped model, the effect of the relative angle can be modeled by changing the parameter values. However, from the result of Chapter 2, it is found that changing the relative angle does not affect the low-frequency characteristics. If the parameter values are modified to represent the high-frequency characteristics, the equivalent circuit would not be able to represent the low-frequency characteristics.

3.2 Parameter estimation method

3.2.1 Inductance component

This subsection describes the estimation method of the inductance components in the air-core transformer. The relationships between the modeling parameter and measured values are given as follows.

$$L_{\mathrm{p}} = L_{\mathrm{s}} = L(Z_{\mathrm{PP'},\mathrm{open}}) \tag{3.1}$$

$$L_{\mathrm{m}} = kL_{\mathrm{p}} = \sqrt{1 - \frac{L(Z_{\mathrm{PP'},\mathrm{short}})}{L(Z_{\mathrm{PP'},\mathrm{open}})}} \tag{3.2}$$

Where k denotes the coupling coefficient, and $L(Z)$ the inductance component estimated from the impedance shown in Chapter 2. The inductance components are estimated with the least-squares method. The estimated parameter values are listed in Tables 3.1 and 3.2. The estimated inductances and coupling coefficient showed constant values even when the slit width and the relative angle were changed. Table 3.2 also shows the mean values. As mentioned in Section 3.1, the change in the high-frequency characteristics due to the

Table 3.1: List of estimated parameter values of inductance component for varying copper coverage

Parameter	Slit width [mm]				
	0.15	0.3	0.5	0.7	0.9
L_p & L_s [nH]	547	548	553	555	564
L_m [nH]	337	330	328	321	322
k	0.615	0.602	0.592	0.579	0.570

Table 3.2: List of estimated parameter values of inductance component for varying relative angle

Parameter	Relative angle [deg]						Mean
	36	60	84	108	132	156	
L_p & L_s [nH]	529	530	530	533	534	533	532
L_m [nH]	323	324	326	328	330	329	327
k	0.609	0.612	0.614	0.615	0.618	0.617	0.614

relative angle is represented by modifying the equivalent circuit topology. In order to remove the effect of changing the parameter value, the equivalent circuit is constructed using the average value to confirm its validity for varying the relative angle. This also applies to the capacitance components.

3.2.2 Capacitance component

As mentioned in Section 3.1, we identify the dominant parasitic capacitance based on the frequency responses of the air-core inductors. The air-core inductor is not affected by the mutual capacitance because it does not have the secondary winding as shown in Fig. 3.2(a). Therefore, we can investigate the effect of the mutual capacitance compared to the air-core transformer with the air-core inductor. We fabricated two air-core inductors. The air-core inductors are fabricated based on the PCB patterns of the air-core transformers with slit widths of 0.15 and 0.9 mm. They are made by removing the secondary winding from the air-core transformers as shown in Fig. 3.2(b).

Figure 3.3 shows the measured frequency responses of the air-core inductors. The blue line shows the impedance of the 0.15 mm slit width-based air-core inductor, and the red line the impedance of the 0.9 mm slit width-based air-core inductor. Figure 3.3 indicates that the effects of the winding self capacitance and winding-to-ground capacitance can

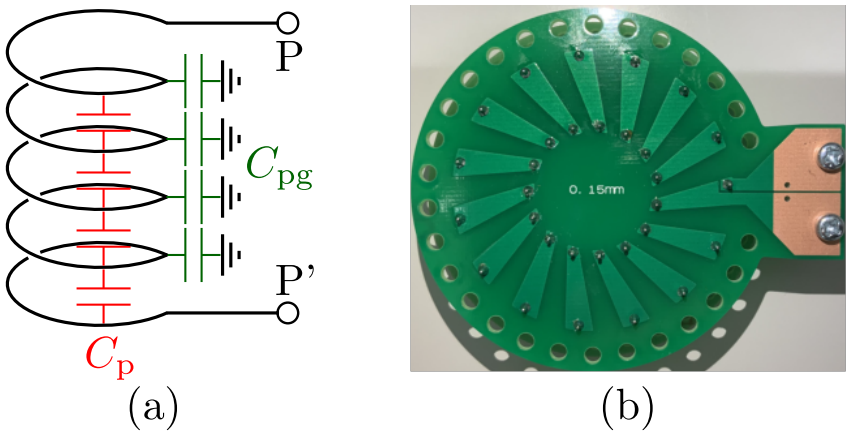

Figure 3.2: A schematic of parasitic capacitance in air-core inductor and a photograph of fabricated 0.15 mm slit width-based air-core inductor.

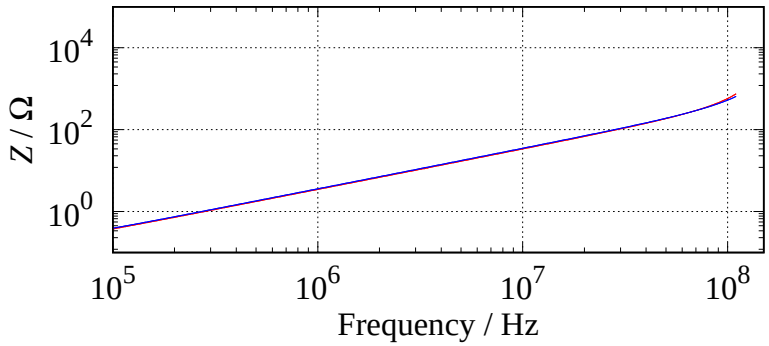

Figure 3.3: Frequency responses of the fabricated air-core inductor. The blue line shows the impedance of the 0.15 mm slit width-based air-core inductor, and the red line the impedance of the 0.9 mm slit width-based air-core inductor.

Table 3.3: List of estimated parameter values of capacitance component for varying copper coverage

Parameter	Slit width [mm]				
	0.15	0.3	0.5	0.7	0.9
$C_{\mathrm{ps'}}$ [pF]	76.7	63.4	54.2	48.0	43.0
C_{ps} [pF]	76.8	63.3	54.2	48.0	43.0

Table 3.4: List of estimated parameter values of capacitance component for varying relative angle

Parameter	Relative angle [deg]						Mean
	36	60	84	108	132	156	
$C_{\mathrm{ps'}}$ [pF]	83.1	83.3	82.5	83.1	83.3	83.1	83.1
C_{ps} [pF]	83.4	83.6	82.6	83.3	83.3	83.4	83.3

be neglected because no clear resonance is confirmed in the measured frequency range. Therefore, $Z_{\mathrm{PS'}}$ and Z_{PS} correspond to the mutual capacitance. We estimate the capacitance components with the least-squares method. As a result, we obtained the same values of the mutual capacitance estimated from $Z_{\mathrm{PS'}}$ and Z_{PS} as shown in Tables 3.3 and 3.4. This result supports the validity of the measurement in this dissertation because only mutual capacitance dominates the air-core transformer. The difference between the frequency responses of $Z_{\mathrm{PS'}}$ and Z_{PS} in the high-frequency region was caused by the changing polarity of the transformer coupling owing to the difference in connecting the terminals.

3.3 Derivation from analogy with coupled transmission lines

The high-frequency equivalent circuit of the air-core transformer is derived in this section. Figure 3.4 shows the schematic of the coupled transmission lines and its equivalent circuit. The equivalent circuit of the coupled transmission lines is represented by Fig. 3.4(b). From the results of Section 3.2, it was found that the winding self capacitance and winding-to-ground capacitance can be neglected in the air-core transformer. Since the mutual capacitance is distributed between the primary and secondary windings, the air-core transformer viewed from the port P–S and P–S' can be regarded as the coupled

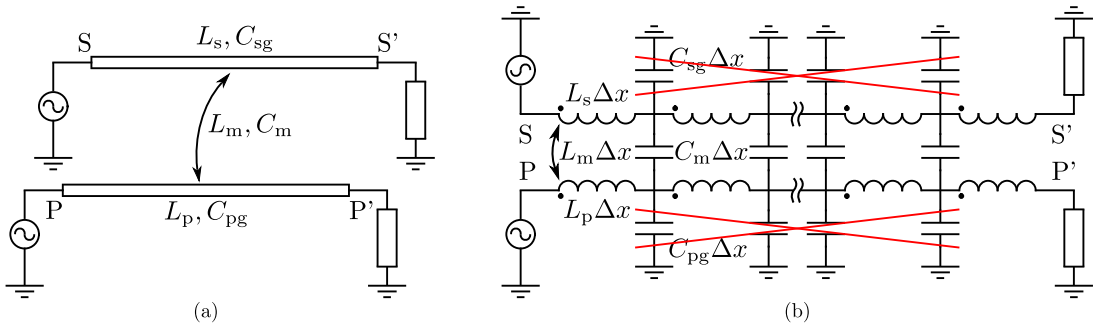

Figure 3.4: A schematic of coupled transmission lines and its equivalent circuit.

transmission lines. Therefore, the propagation velocity v is given by Eq. (3.3).

$$v = \frac{1}{\sqrt{L_{p'} C_{m'}}} = \frac{1}{\sqrt{L_{s'} C_{m'}}} \tag{3.3}$$

Where $L_{p'}$ denotes the self-inductance of the primary winding per unit length, $L_{s'}$ the self-inductance of the secondary winding per unit length, and $C_{m'}$ the mutual capacitance between the primary and secondary windings per unit length.

A circuit element can be regarded as a lumped element when the physical dimensions are small enough compared to the wavelength. The general consensus is when the dimension is smaller than about 1/20 of the wavelength [69]. The relationship between the wavelength λ, frequency f, and propagation velocity v is given by Eq. (3.4).

$$v = f\lambda \tag{3.4}$$

The wavelength is calculated to be 1.05 m when the transformer is excited at 110 MHz. Since the winding length is calculated to be 0.741 mm, the transformers cannot be represented until 110 MHz by the lumped element equivalent circuit as shown in Fig. 3.5 (a) (hereinafter referred as lumped model).

In this dissertation, we represent the distributed parameter model of the transformer with the lumped element approximation. Fig. 3.5 (b) shows the equivalent circuit of an arbitrary section of the transformer. Suppose that the self-inductance, mutual inductance, and mutual capacitance are uniformly distributed along the length of the windings. We can derive the equivalent circuit of the air-core transformer by connecting the equivalent circuits of an arbitrary section, considering the transformer structure. The number of the transformer divisions N is set to 16 for the verification in the copper coverage, so that the symmetry and Eq. (3.5) are satisfied.

$$N \geq \frac{20\ell}{\lambda} \tag{3.5}$$

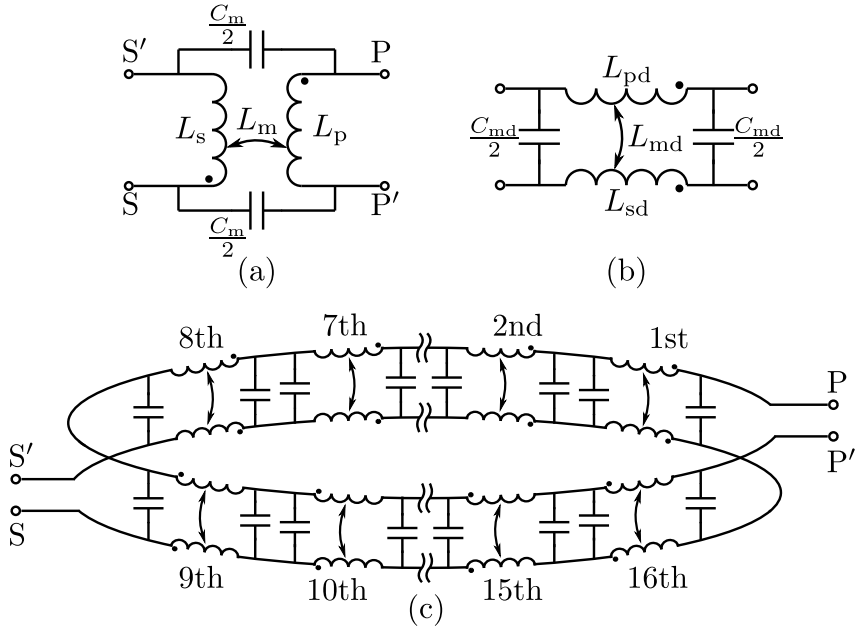

Figure 3.5: Schematics of equivalent circuit of interleaved air-core toroidal transformer: (a) lumped model, (b) an arbitrary section, and (c) distributed model.

The number of the transformer divisions N is reset to 32 for the verification in the relative angle, in order to increase the number of the relative angles that can be represented. The equivalent circuit is obtained as shown in Fig. 3.5 (c) (hereinafter referred as distributed model).

3.4 Verification of equivalent circuit

We verify the distributed model through comparisons with circuit simulations. The circuit simulations are conducted using a commercial circuit simulator (SIMetrix Technologies, SIMetrix Ver. 7.2). The terminals that are not connected to the voltage source are floated with a 10 MΩ resistor. The consideration implies that the reference potentials of the primary and secondary windings are different, that is, the primary winding is isolated from the secondary winding. First, we compare the distributed model with the lumped model. Figure 3.6 shows the comparisons of the measurement with the circuit simulation for the air-core transformer with 0.15 mm slit width and 180 deg relative angle. The black lines denote the measured results, the red dotted lines the circuit simulation obtained from the distributed model, and the blue dotted lines the circuit simulation obtained from the lumped model. The distributed model represents the frequency responses accurately.

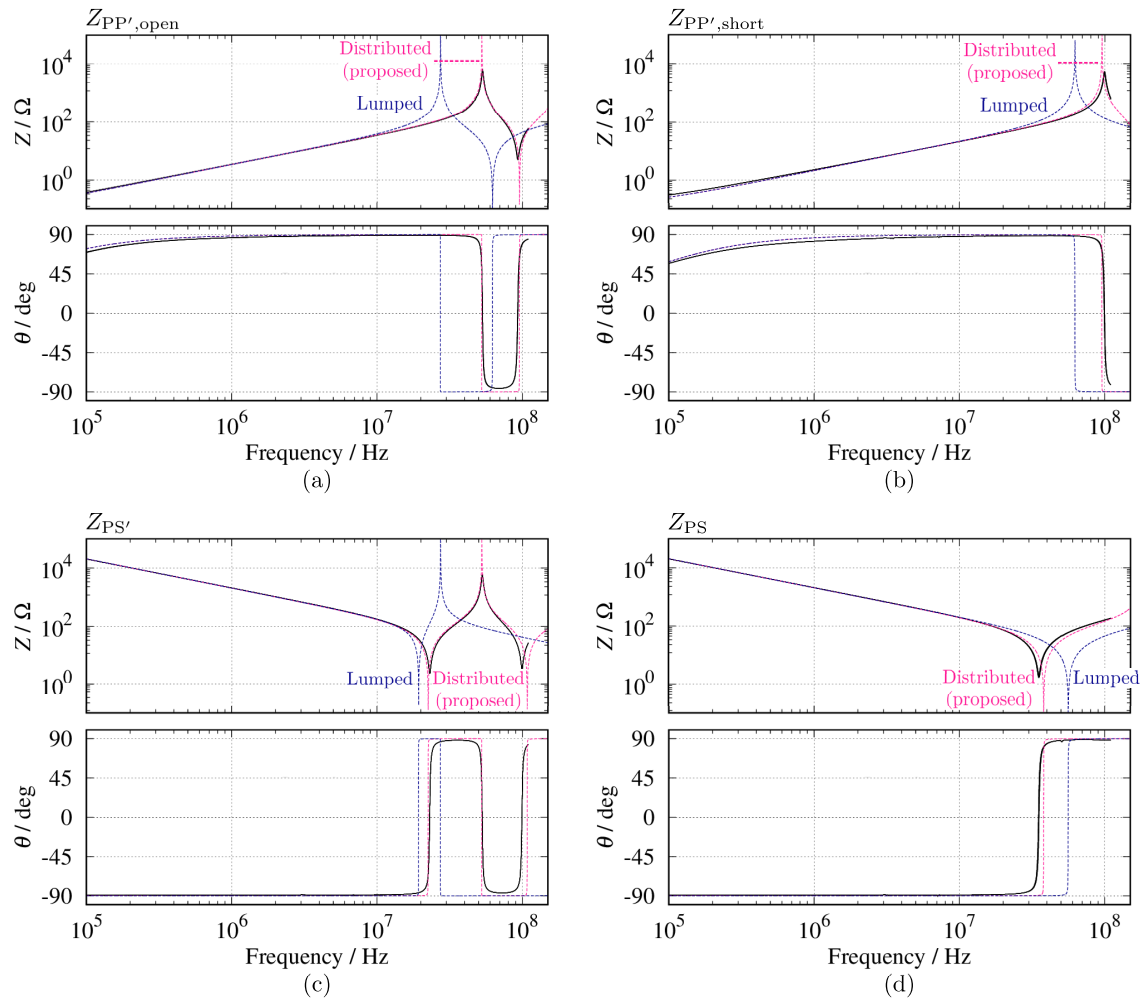

Figure 3.6: Comparisons of measurement with circuit simulation. The black lines show the measured results, the red dotted lines the circuit simulation based on the distributed model, and the blue dotted lines the circuit simulation based on the lumped model.

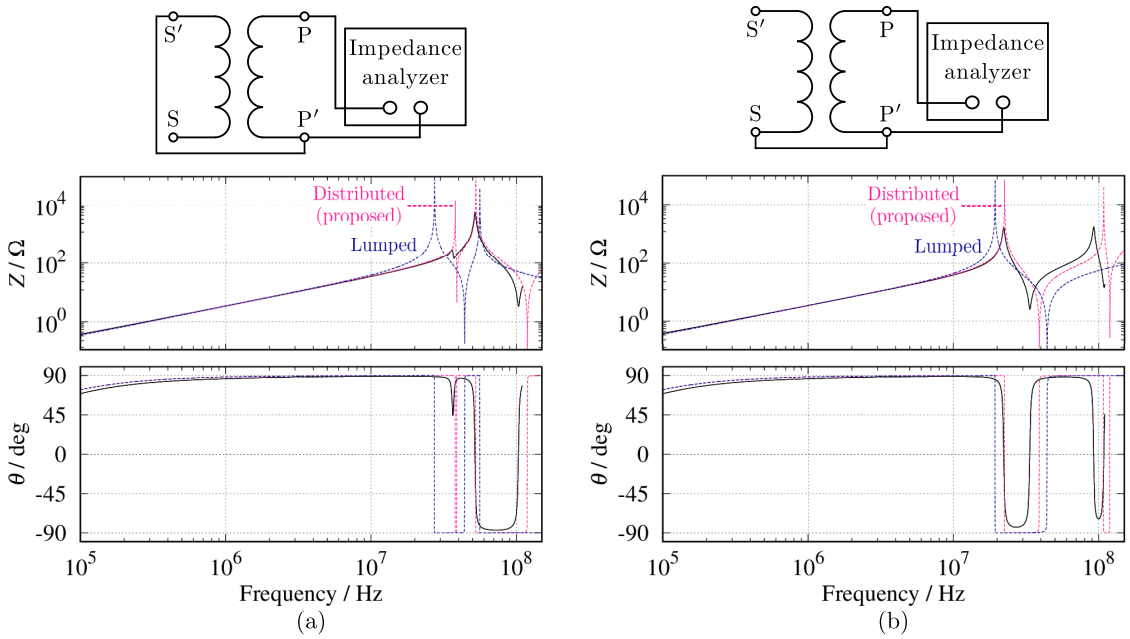

Figure 3.7: Comparisons of measurement with circuit simulation at same reference potential between primary and secondary windings. The black lines show the measured results, the red dotted lines the circuit simulation based on the distributed model, and the blue dotted lines the circuit simulation based on the lumped model. The above schematics show the measurement setup.

The difference between the measurement and circuit simulation to the lumped model gradually increases in the frequency range above 10 MHz. This is due to the frequencies, which are not less than 1/20 of the wavelength, are calculated to be 7.7 MHz. In addition, the lumped model does not represent the third resonant frequency in Fig. 3.6(c). These results indicate the limit of the lumped model at high-frequency region. Therefore, the distributed model is suitable for modeling the air-core transformer.

Let us also consider the frequency response when the reference potentials of the primary and secondary windings are the same. Figure 3.7 shows the comparisons of the measurement with the circuit simulation at the same reference potential between the primary and secondary windings. The black lines show the measured results, the red dotted lines the circuit simulation based on the distributed model, and the blue dotted lines the circuit simulation based on the lumped model. The above schematics show the measurement setup. The distributed model represents the frequency responses accurately in these conditions. The circuit simulation requires that there be the same reference potential on the primary and secondary sides, respectively. When the secondary winding is grounded,

the frequency response changes significantly. The change is caused by the effect of the mutual capacitance. Care must also be taken in handling the potential of the secondary winding when considering the effect of mutual capacitance.

Then Fig. 3.8 shows the comparisons of the measurement with the circuit simulation for varying the slit width. The solid lines show the measured results, and the dotted lines the circuit simulation based on the distributed model. The proposed equivalent circuit represents the frequency responses accurately.

Figure 3.9 shows the comparisons of the measurement with the circuit simulation for varying the relative angle. The solid lines show the measured results, and the dotted lines the circuit simulation based on the distributed model. The proposed equivalent circuit represents the frequency responses accurately. As with the result of Chapter 2, $Z_{\mathrm{PP'},\mathrm{short}}$ does not change for varying the relative angle in the circuit simulation as well. This supports the explanation given in Chapter 2. However, the circuit simulation shows the resonance of Z_{PS} although this cannot be confirmed clearly in the experiment.

In order to discuss this resonance, Fig. 3.10 shows the enlarged views of the frequency response in Z_{PS} from 40 to 80 MHz. In Fig. 3.10(b), the circuit simulation shows the resonance. On the other hand, the experiment shows the rapid phase change. This change seemingly corresponds to the resonance in the circuit simulation. Even though this measurement is for a passive component, the measured phase exceeds 90 deg. This does not happen in passive component measurements theoretically. This is also a result showing the limit of measurement by an impedance analyzer. The resonance is seemingly caused by the symmetry breaking in the air-core transformer. That is because the signs of resonance can be confirmed experimentally in the frequency response for varying the slit width as shown in Fig. 3.10(a). It can be inferred that this symmetry breaking was caused by the manufacturing accuracy of the air-core transformer.

3.5 Summary

In this chapter, we derived the high-frequency equivalent circuit of the air-core transformer from analogy with the coupled transmission lines. It was found that the frequency responses of the air-core transformer were mainly affected by the mutual capacitance depending on the slit width. The air-core transformer can be modeled on the basis of analogy with the coupled transmission lines when the winding self capacitance and winding-to-

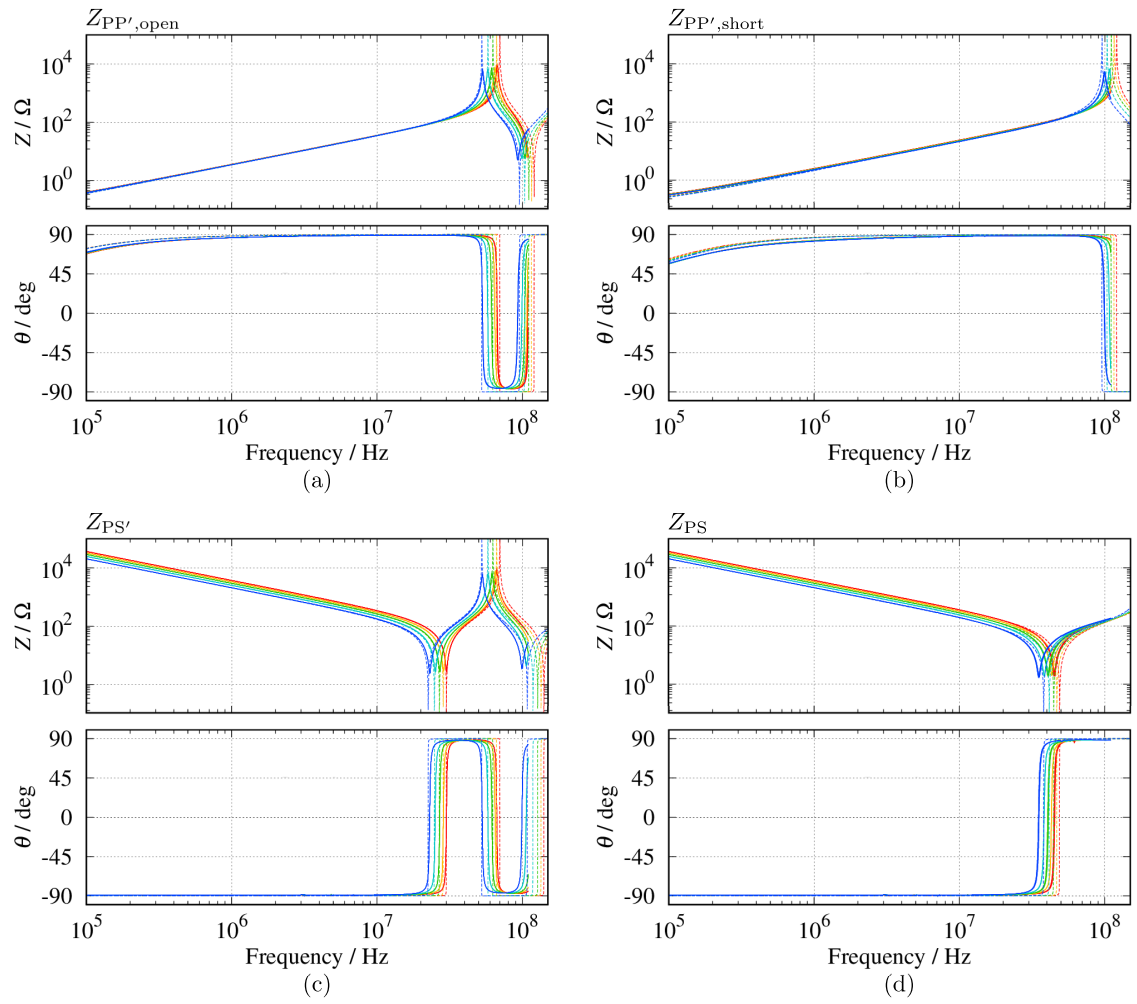

Figure 3.8: Comparisons of measurement with circuit simulation for varying slit width. The solid lines show the measured results, and the dotted lines the circuit simulation based on the distributed model.

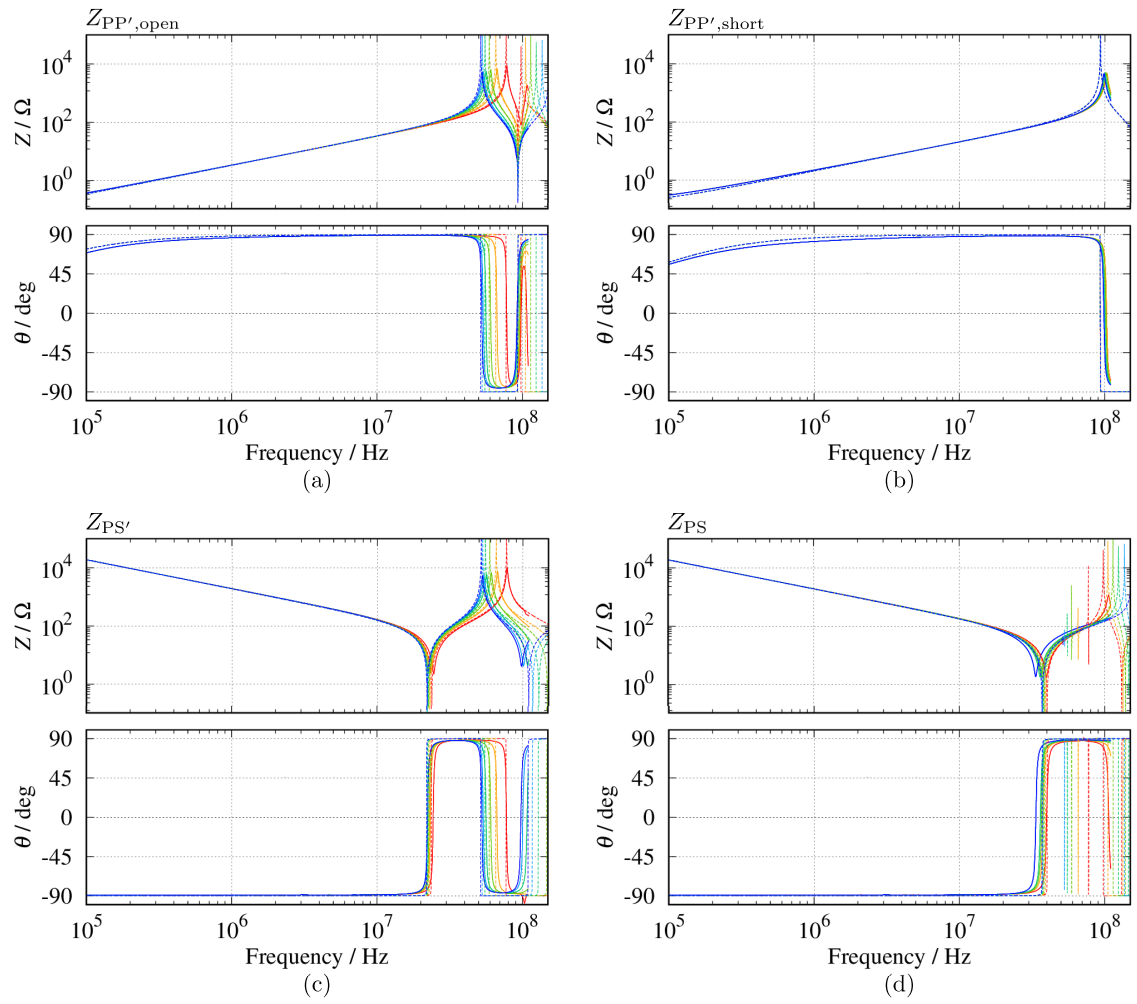

Figure 3.9: Comparisons of measurement with circuit simulation for varying relative angle. The solid lines show the measured results, and the dotted lines the circuit simulation based on the distributed model.

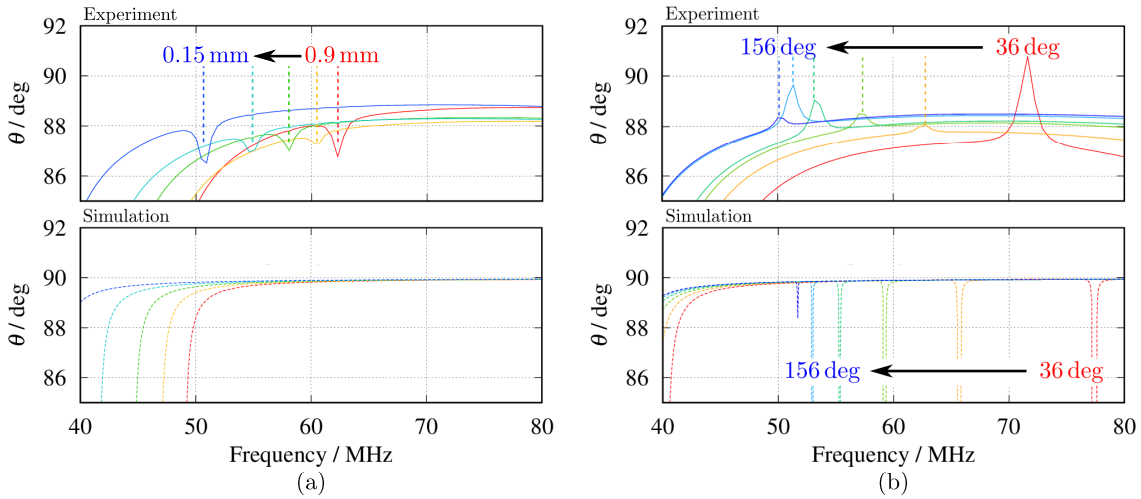

Figure 3.10: Enlarged views of frequency response in Z_{PS} from 40 to 80 MHz: (a) for varying slit width and (b) for varying relative angle.

ground capacitance are negligible. The derived distributed equivalent circuit represented the frequency responses accurately, whereas the lumped model was not able to represent the high-frequency characteristics. Both equivalent circuits were constructed with the same parameter values estimated from the low-frequency characteristics. Only the circuit topology is different in both models. In addition, the proposed equivalent circuit did not use the high-frequency characteristics such as the resonant frequency. This is inherently different from methods such as Foster's reactance theorem [67], which uses high-frequency characteristics in order to construct the frequency response. These results show the importance of the mutual capacitance to be implemented as a distributed parameter.

We confirmed that the derived equivalent circuit was able to represent the frequency responses of the air-core transformer for varying the slit width and the relative angle. The frequency responses of the air-core transformer for the relative angle cannot be represented by the lumped model without changing the parameter values. The proposed model was able to represent the frequency responses only by modifying the equivalent circuit topology without changing the parameter values. This result indicated that it is necessary for the analysis of the high-frequency characteristics to consider the distribution of the physical quantity such as current and voltage in the air-core transformer.

Wavelength-dependent phenomena such as $\lambda/4$ resonance and directivity appear in the coupled transmission lines. The equivalent circuit was derived from analogy with the coupled transmission lines. The fact implies that the phenomena cannot be avoided due

to the switching of the power converter. That is because there are many high-frequency components during switching transients.

In this chapter, we conclude that the proposed equivalent circuit enables us to simulate the operation of power converters in the frequency range above megahertz. The author also expects that the model can clarify the relationship between the high-frequency components and the spatial magnetic flux distribution in air-core transformers.

Chapter 4

Measurement method for internal magnetic flux density distribution

In this chapter, we develop the measurement method for the internal magnetic flux density distribution under high-frequency excitation. From the results of the previous chapters, it is found that the approach based on the physical quantity distribution is necessary to analyze the high-frequency characteristics of the air-core transformer. In general, it is difficult to measure the internal state of the device under test (DUT) directly. The air-core transformer in this dissertation is mainly dominated by the mutual capacitance in the frequency ranging up to 110 MHz. Since the maximum mutual capacitance was calculated to be several tens of pF, the mutual capacitance per turn is of the order of pF. The input capacitance of the passive probe is typical of the order of pF. The voltage distribution cannot be measured by connecting the passive probe directly to the windings because the input capacitance is of the same order of magnitude as the parasitic capacitance. The current probe cannot be installed because of its size. Therefore, it is difficult to analyze the distribution of the voltage and current in the air-core transformer.

In this dissertation, we focus on the internal magnetic flux density distribution. The magnetic flux density is a key factor governing the performance of a transformer. The magnetic flux is generated by the current flowing along the windings. As the current distribution changes, the magnetic flux density distribution also changes. A previous study reported that in a toroidal inductor, the external magnetic flux density distribution changes depending on the excitation frequency [70]. Specifically, the distribution is different if it is below or above the resonant frequency. This implies that the internal magnetic flux density also changes. Therefore, the magnetic flux density has the potential to be a

physical quantity for analyzing the high-frequency characteristics.

There have been studies on the internal magnetic flux density distribution of the magnetic components used in the below-kilohertz frequency range [71–75]. However, it is difficult to apply these methods to this dissertation's target for the following reasons. First, these studies do not aim at the megahertz frequency range. In the megahertz frequency range, the measurement equipment affects the operation of the measured circuit owing to its impedance. For example, connecting a passive probe is equivalent to adding an extra capacitor to the circuit. In the low-frequency range, the impedance of the passive probe can be neglected. On the other hand, in the high-frequency range, the impedance cannot be neglected because the impedance of the capacitor is inversely proportional to the frequency. Thus, high-frequency measurements are inaccurate with passive probes. To measure the distribution in the megahertz frequency range, it is necessary to make sure that the effect of the measurement equipment on the DUT can be neglected. Second, these studies focus on the distribution inside the magnetic materials. In the below-kilohertz frequency range, transformers use magnetic materials such as Mn-Zn and Ni-Zn. To measure the internal magnetic flux requires the processing of the magnetic materials. For example, a hole is needed in the magnetic materials to install the magnetic sensor. Since this dissertation investigates the air-core transformer, which does not use magnetic materials, it is difficult to apply these methods directly. Therefore, it is necessary to develop a measurement method that meets the purpose of this study.

In Section 4.1, the magnetic flux density sensor and the measurement principle are explained. The experimental setup is described in Section 4.2. In Section 4.3, the measured magnetic flux density distribution is analyzed. The measured distribution is verified through a comparison with numerical estimation in Section 4.4. In Section 4.5, the effect of the measurement equipment impedance is discussed.

4.1 Magnetic flux density sensor

In this dissertation, we measure the internal magnetic flux density of the air-core transformer with a search coil sensor. The search coil is inserted easily in the inside of the air-core transformer because of the air-core configuration. It can be manufactured directly by the user as opposed to other magnetic sensors [76]. Thus, almost everyone can perform the investigation carried out in this dissertation using a simple and very low-cost,

yet accurate search coil sensor.

The search coils are manufactured for two kinds of measurements: the tangential component and the normal component as shown in Fig. 4.1. Figure 4.2 shows the photographs of the fabricated search coil for measuring the tangential component. The search coil consists of Bakelite boards and copper wires ($\phi = 0.25\,\mathrm{mm}$). The Bakelite board has the holes made with a PCB manufacturing machine (Mits, Seven Mini) to thread the copper wires. The search coil is fabricated by threading the copper wire into the hole. Therefore, the cross-section of the search coil is rectangular in shape.

Let us move on to the implementation method for the search coil. In this chapter, an air-core transformer, which is different from the one used in other chapters, is fabricated for experiments to confirm the validity of the measurement method. Figure 4.3 shows the photographs of the air-core transformer in this chapter. The air-core transformer is fabricated using printed circuit boards (PCBs) and contact probes. The inner and outer diameters are set to be the same values as used in Chapter 2. The number of turns in both the primary and secondary windings is also set to be the same value. The height of the air-core transformer is different and changed to 9.6 mm. By using the contact probe, the air-core transformer can be divided into two parts. The search coil can be mounted inside the air-core transformer by sandwiching the coil between the two parts. The contact probes pass through the holes, which are made in the outer circumference of the Bakelite board. Therefore, the position of the search coil is determined as shown in Fig. 4.4. The implementation method is used in the first half of this chapter. Another method is adopted in the second half of this chapter.

The principle behind the search coil is Faraday's law of induction. When the air-core transformer is excited, a magnetic flux arise in the air-core transformer. The search coil voltage is induced by the variation in the magnetic flux passing through the search coil cross-section. Assuming that the cross-sectional area in the search coil is sufficiently smaller than in the air-core transformer, the relationship between the voltage of the search coil v_{search} and the internal magnetic flux density B can be estimated by Eq. (4.1).

$$B = \frac{1}{\mathrm{AT}} \int v_{\mathrm{search}} \mathrm{d}t \tag{4.1}$$

The area-turn product, denoted AT, is determined from the number of turns and the cross-sectional area of the search coil. The number of turns in the search coil is set to 6 turns and the cross-section to $9.6\,\mathrm{mm}^2$. We determine the area-turn product from these

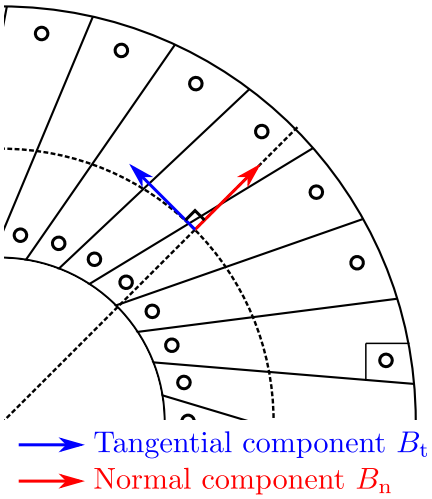

Figure 4.1: Definition of tangential and normal components.

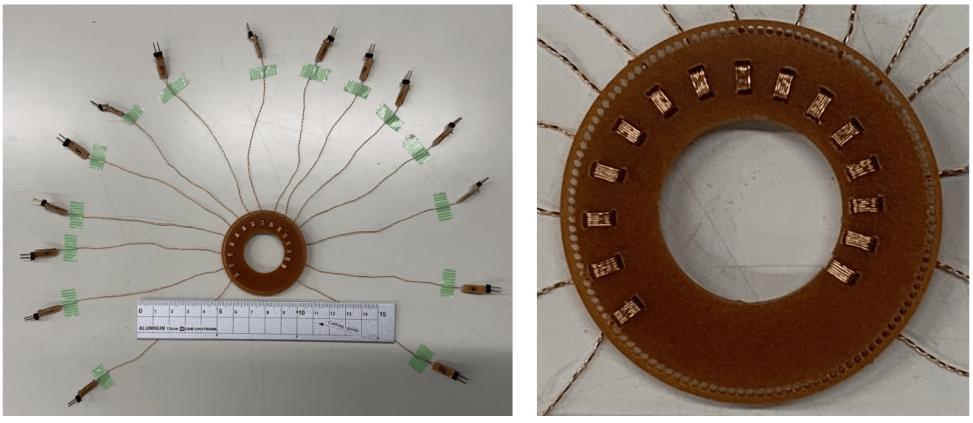

(a) (b)

Figure 4.2: Photographs of search coil for measuring tangential component: (a) overall photograph and (b) enlarged photograph.

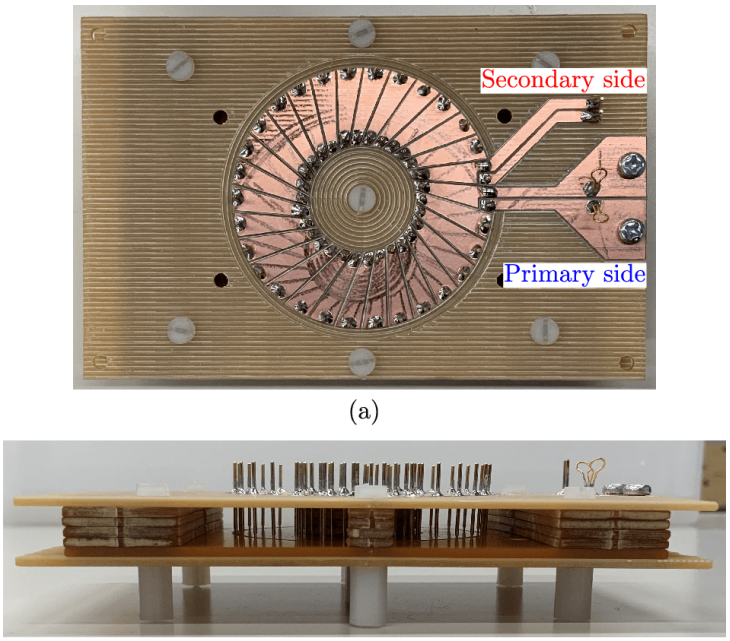

Figure 4.3: Photographs of air-core transformer: (a) top view and (b) side view.

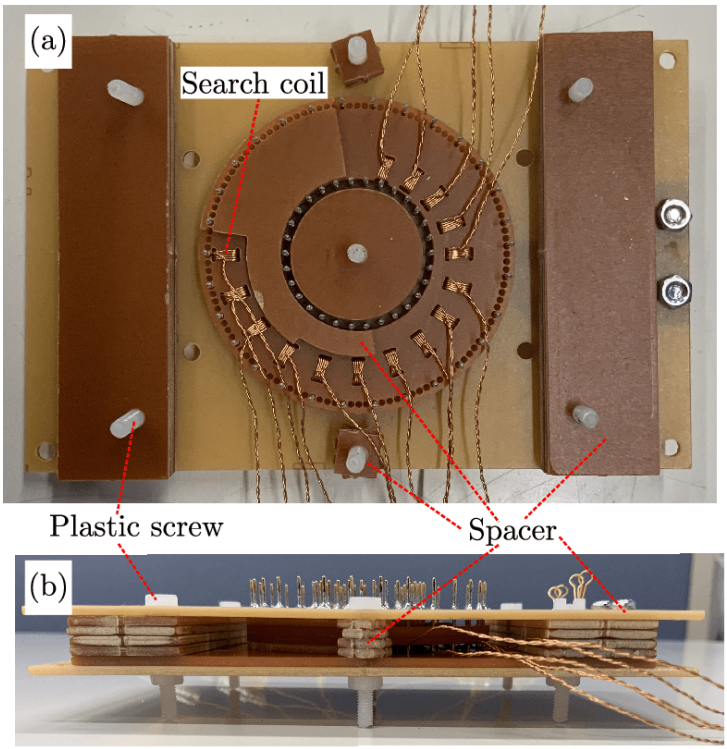

Figure 4.4: Photographs of air-core transformer with search coil part: (a) inside view and (b) side view.

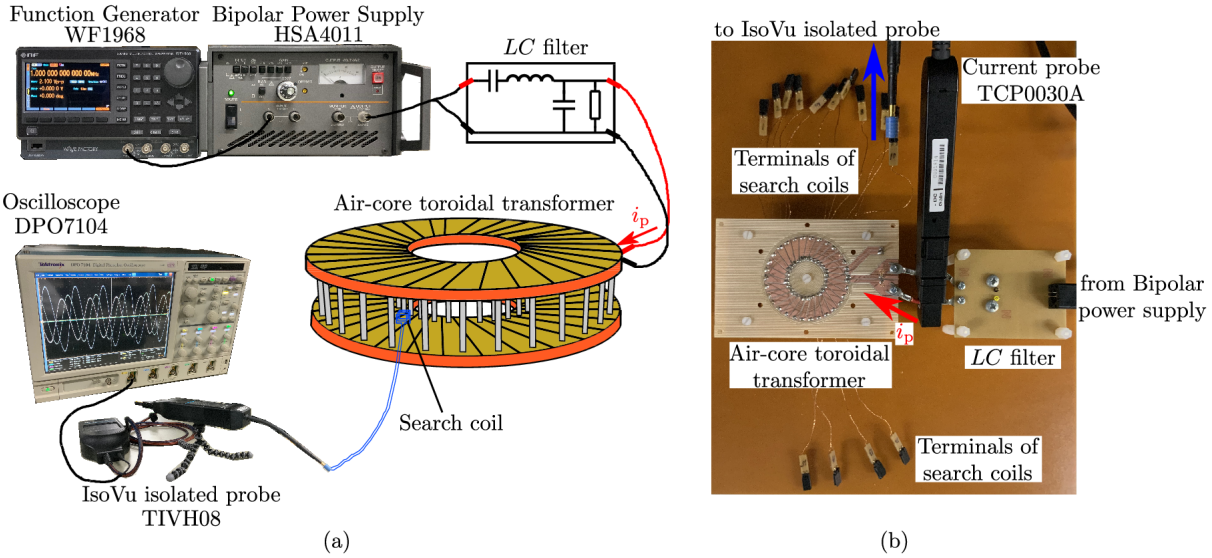

Figure 4.5: Experimental setup for measuring internal magnetic flux density distribution in air-core transformer: (a) measurement setup schematic and (b) photograph of the equipment surrounding air-core transformer.

values. The cross-section of the search coil satisfies the previously stated assumption as it has a value less than 1/10 of that of the transformer. The voltage of the search coil is measured by using an isolated probe (Tektronix, TIVH08) and an oscilloscope (Tektronix, DPO7104). Therefore, the internal magnetic flux density can be obtained by measuring voltage of the search coil and integrating it numerically in the trapezoidal rule.

4.2 Experimental setup

Figure 4.5 shows the experimental setup schematic for measuring the internal magnetic flux density distribution. A sinusoidal current is fed to the air-core transformer as an excitation current. The excitation current is generated with a function generator (NF CORPORATION, WF1968), a bipolar power supply (NF CORPORATION, HSA4011), and an *LC* filter. The bipolar power supply amplifies the signal from the function generator, however, the amplified signal is slightly distorted because of the characteristics of the bipolar power supply. Therefore, an *LC* filter was inserted between the bipolar power supply and the air-core transformer to remove the distortion in the amplified signal. The generated excitation current i_p is then fed to the primary side of the air-core transformer.

The purpose of this chapter is to demonstrate the effectiveness of the proposed method

in the megahertz range. First, we investigate whether the fabricated search coil can measure the magnetic flux density at 1 MHz. Since the principle of the search coil is based on Faraday's law of induction, the magnitude of the search coil voltage depends on the rate of change of the magnetic flux. Thus, the sensitivity of the search coils is proportional to the excitation frequency. If the excitation frequency is too low, the search coil voltage could be lower than the voltage that can be measured by the oscilloscope. To increase the search coil voltage, the area-turn product needs to be increased. This corresponds to the increase in the number of turns and the cross-sectional area. However, this leads to an increase in the parasitic capacitance of the sensor and the sensor size. An increase in the parasitic capacitance is related to the maximum measurable frequency, which is determined by its self-resonant frequency. The detailed discussions are shown in Section 4.5. An increase in the sensor size makes its spatial resolution to degrade. For this reason, if the sensor is fabricated so that the measurement range of the sensor is within the range of the oscilloscope, the distribution may not be obtained correctly. Therefore, we investigate whether the internal magnetic flux density distribution under 1 MHz excitation can be measured using the search coil fabricated in the previous section. The validity of the measurement results at 1 MHz implies that it is possible to measure higher frequency components without changing the dimensions of the search coil. It is because the magnitude of the search coil voltage at 1 MHz is the lowest in the megahertz frequency excitation. Therefore, an excitation current i_p with an amplitude of 1.5 A and a frequency of 1 MHz is fed into the air-core transformer. We measure the magnetic flux density B for four cycles. The search coils are located at the middle height of the air-core transformer ($z = 4.8\,\mathrm{mm}$). Figure 4.6 shows the measurement points used in this study. The sampling frequency of the oscilloscope is set to 5 GHz, and the excitation current i_p is measured with a current probe (Tektronix, TCP0030A).

4.3 Internal magnetic flux density distribution under 1 MHz sinusoidal excitaiton

This section presents the experimental results of the internal magnetic flux density distribution for the air-core transformer. First, we discuss the magnetic fluxes measured at point A in Fig. 4.6.

Figure 4.7 shows the waveforms of (a) the excitation current, (b) the search coil volt-

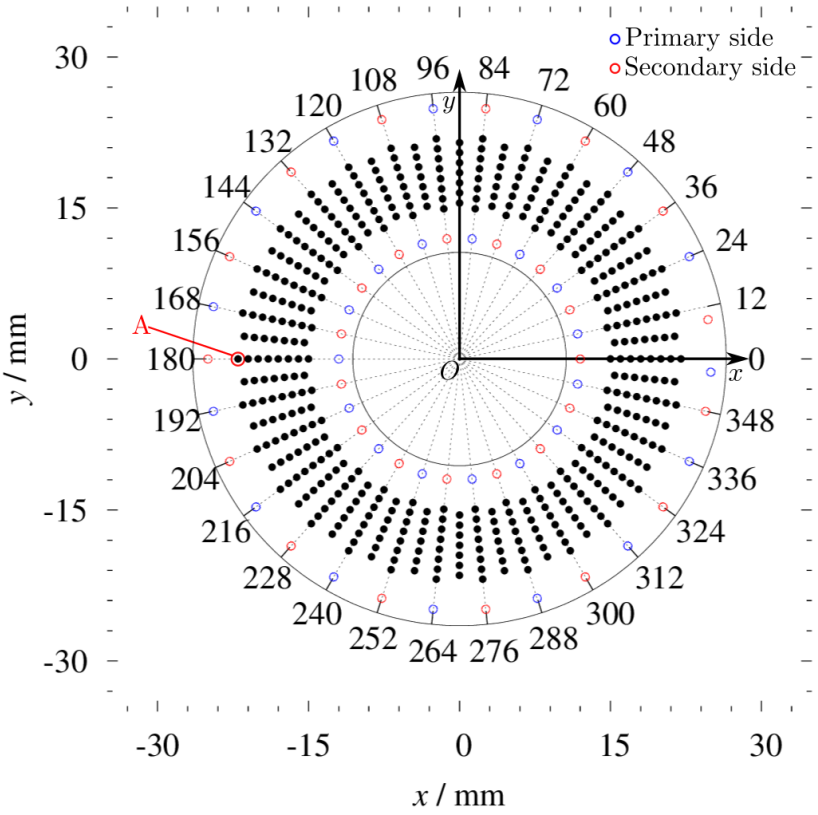

Figure 4.6: Measurement points in the air-core transformer. Numbers around the circle denote angle. Blue circles denote primary side contact probes, and red circles secondary side contact probes.

age, and (c) the magnetic flux density calculated from the search coil voltage measured at point A in Fig. 4.6. The blue and red lines indicate the tangential and normal components, respectively. In Fig. 4.7(a), the excitation currents of the tangential and normal components exhibit the same amplitude. However, the search coil voltage does not display the coincidence between the tangential and normal components. The tangential component is larger in magnitude than the normal component of the search coil voltage. The search coil voltage is of the order of several tens of mV in the tangential component. Since the search coil voltage is clearly confirmed, AT can be decreased a little. In the second half of this chapter, the physical dimension of the search coil is modified on the basis of this result in order to increase the spatial resolution and decrease the parasitic capacitance. The calculated magnetic flux density exhibits a similar result to that of the search coil voltage. This result indicates that the tangential component is dominant in the internal magnetic flux density.

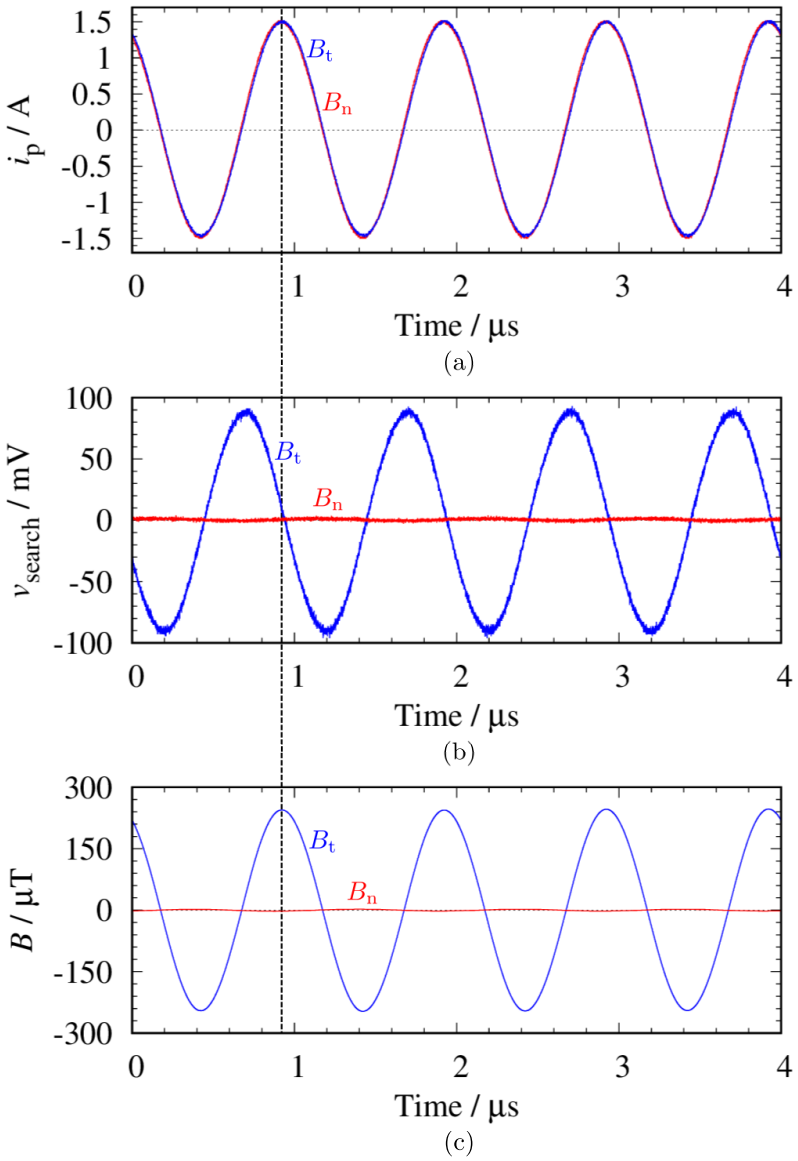

Figure 4.7: Experimentally obtained waveforms: (a) excitation current i_p, (b) search coil voltage v_{search}, and (c) magnetic flux density B calculated from search coil voltage. Blue line shows tangential components, and red line normal components.

Next, we discuss the internal magnetic flux density distribution in the air-core transformer. Figure 4.8 shows the vector field and the contour plot of the measured magnetic flux. The tangential component of the internal magnetic flux density is dominant at every measured point. The magnetic flux density is not uniform in the tangential and normal directions. In a toroidal coil, non-uniformity in the normal direction is apparent from Eq. (4.2) derived from Ampere's law.

$$B = \frac{\mu_0 \mathrm{NI}}{2\pi r} \tag{4.2}$$

Where μ_0 denotes the permeability in a vacuum, N the number of turns in the toroidal coil, I the excitation current, and r the distance from the center of the toroidal coil. Equation (4.2) implies that the magnetic flux density decreases with increasing distance from the center of a toroidal coil. In Fig. 4.8, the inner magnetic flux densities are clearly larger than the outer magnetic flux densities. The experimental results are qualitatively consistent with Eq. (4.2). Therefore, the non-uniformity of the magnetic flux density in the normal direction is caused by the toroidal winding structure.

Subsequently, we consider the non-uniformity of the magnetic flux density in the tangential direction. Equation (4.2) can only discuss the magnetic flux density for the normal direction. That is because Eq. (4.2) is derived under the assumption that the magnetic flux density is uniform for the tangential direction. However, the measured distribution showed the non-uniformity for the tangential direction. In order to verify the validity of the proposed method, it is necessary to clarify whether the non-uniformity in the tangential direction is caused by the measurement method or the transformer structure.

Figure 4.9 shows the magnetic flux density as a function of the angle in the air-core transformer. The physical relationship between the air-core transformer structure and the radius plotted in Fig. 4.9 is shown in Fig. 4.10. The magnetic flux density changes periodically with a spatial period of 24 degrees except in Fig. 4.9(c). The air-core transformer is wound with a spatial period of 24 degrees, because the number of turns in the primary and secondary windings is 15 turns each. Therefore, the spatial period of the non-uniformity in the tangential direction is consistent with the structure of the air-core transformer.

The spatial phases of non-uniformity show a 180-degree difference between the outer side (Fig. 4.9(a) and (b)) and the inner side (Fig. 4.9(d)) of the air-core transformer. The structure of the air-core transformer has a 180-degree difference in a spatial phase between

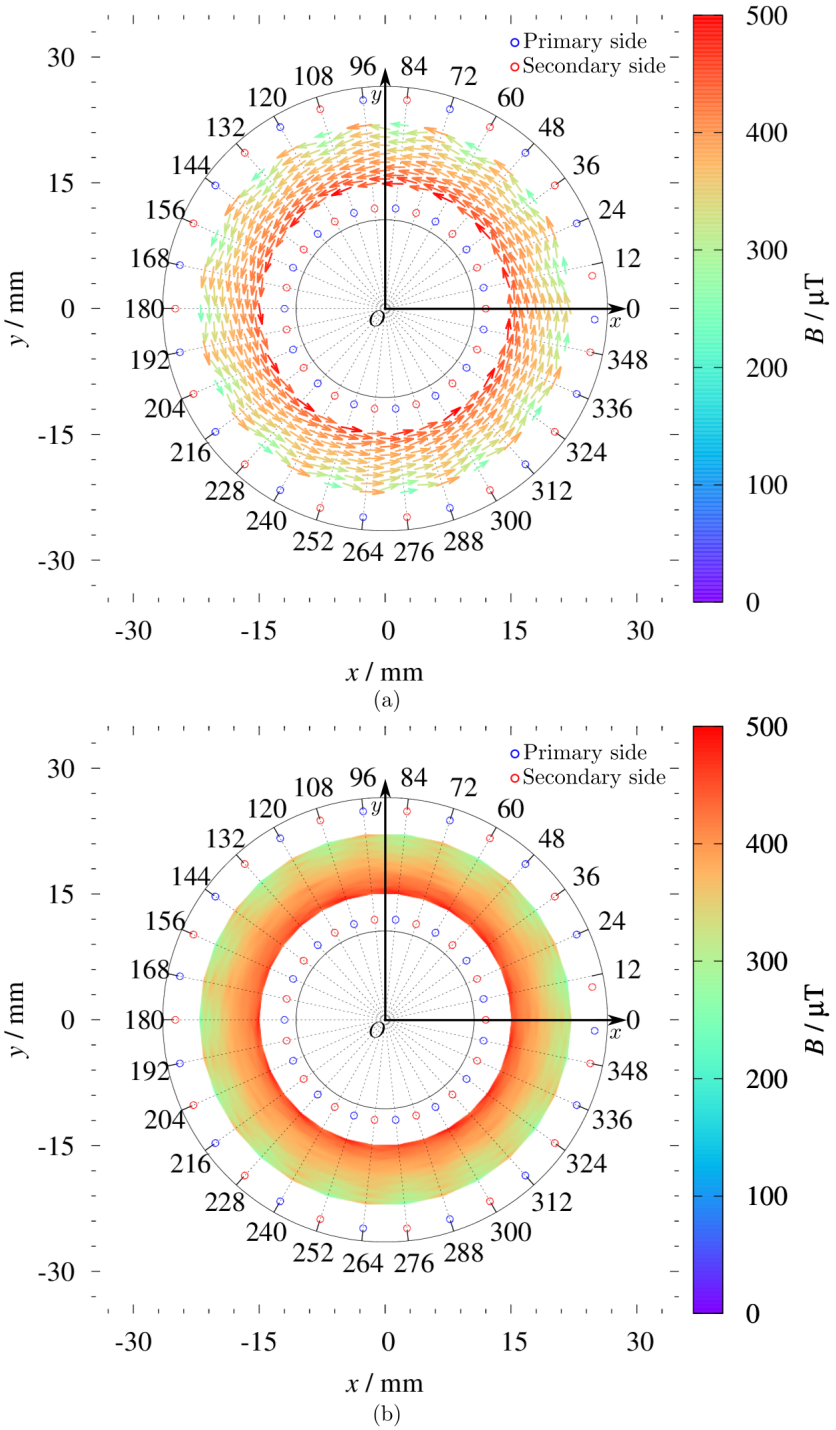

Figure 4.8: Experimentally obtained internal magnetic flux density distribution in air-core transformer: (a) vector field and (b) contour plot. Numbers around the circle denote angle. Blue circles denote primary side contact probes, and red circles secondary side contact probes.

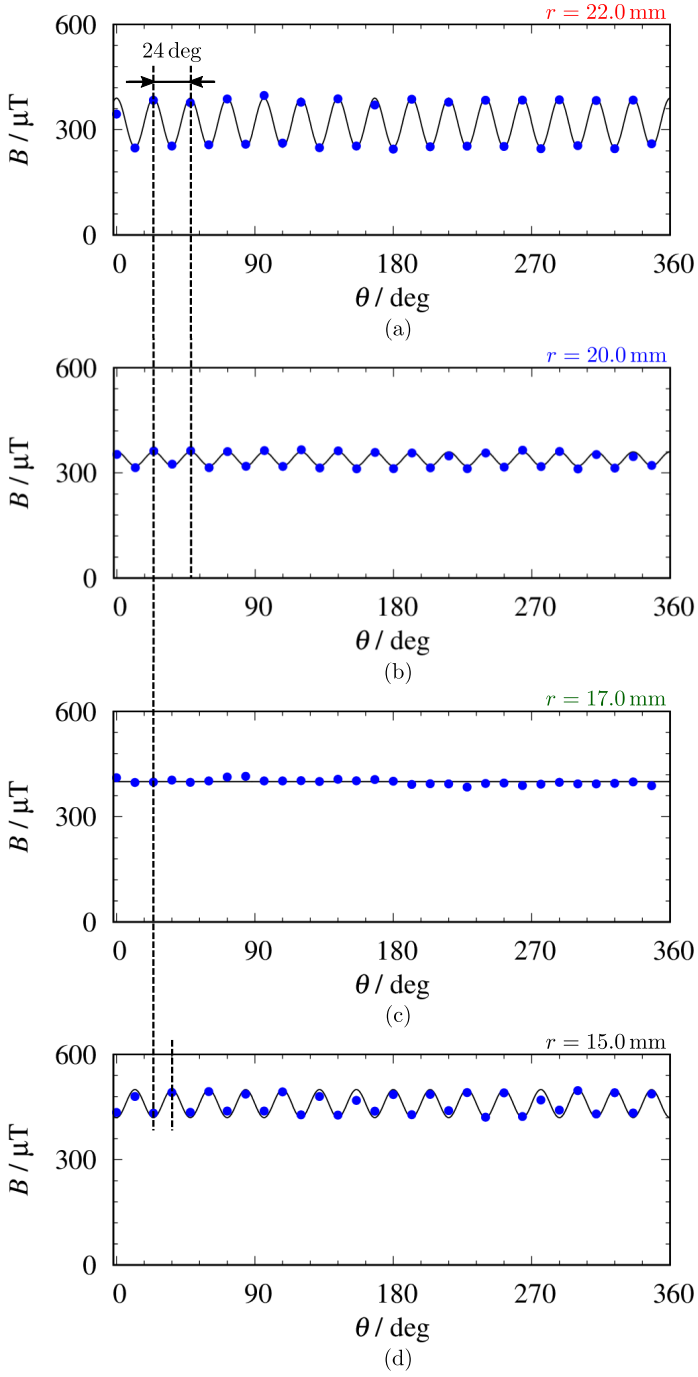

Figure 4.9: Non-uniformity in magnetic flux density in tangential direction for: (a) $r = 22.0\,\mathrm{mm}$, (b) $r = 20.0\,\mathrm{mm}$, (c) $r = 17.0\,\mathrm{mm}$, and (d) $r = 15.0\,\mathrm{mm}$ in order to compare experimentally obtained internal magnetic flux densities as function of angle in air-core transformer.

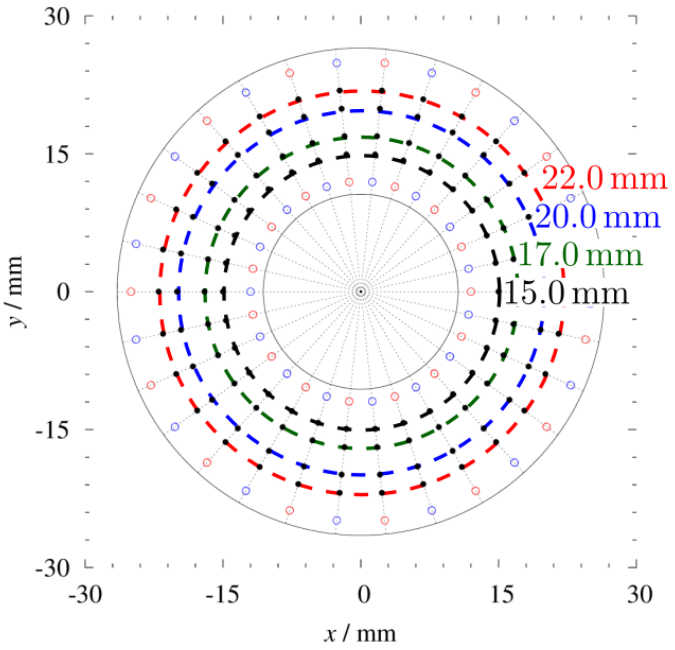

Figure 4.10: Relationship between air-core transformer structure and radius plotted in Fig. 4.9.

the inner and outer sides. The spatial phase difference of the non-uniformity displayed in the results is consistent with the structure of the air-core transformer. The structure of the air-core transformer causes the non-uniformity in the internal magnetic flux density for the tangential direction.

4.4 Verification with numerical estimation

Herein, we verify the measured internal magnetic flux density distribution through a comparison with numerical estimation. We assume that the current distribution in the air-core transformer could be represented by a set of straight conductors. The magnetic flux density of a straight conductor at a point P is given by Eq. (4.3) from the Biot-Savart law.

$$B = \frac{\mu_0 \mathrm{I}}{4\pi r} (\cos\alpha + \cos\beta) \tag{4.3}$$

Where μ_0 denotes the permeability in a vacuum, I the excitation current, and r the distance between the straight conductor and point P. The values of α and β are defined in Fig. 4.11. Due to the air-core configuration, the internal magnetic flux density distribution becomes the sum of the magnetic flux density provided by each straight conductor. The

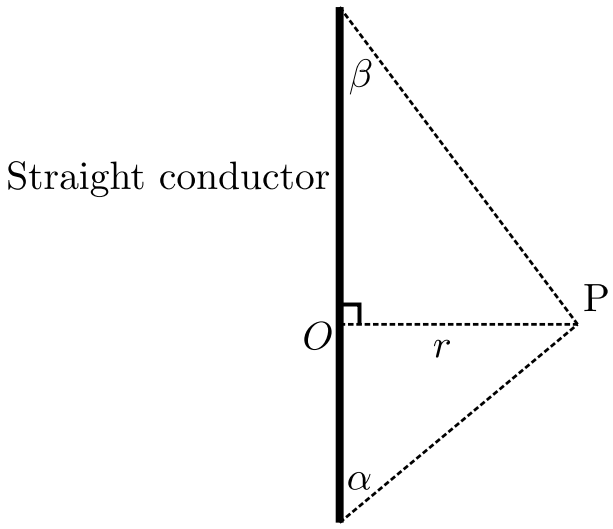

Figure 4.11: Definition of α and β.

detailed calculation is shown below.

First, we describe the method for estimating the magnetic flux density generated by the contact probe. The contact probe provides x and y components of the magnetic flux density because the contact probe and the estimation plane intersect vertically. Figure 4.12 shows a schematic of the relationship between the current flowing along the contact probe and the magnetic flux density. The magnitude of the magnetic flux density B at (x_0, y_0) can be estimated by Eq. (4.3). Based on this equation and Fig. 4.12, x and y components of the magnetic flux density can be determined by Eqs. (4.4a) and (4.4b), when the estimated position is in the first quadrant.

$$B_x = -\frac{\left|\frac{y_0}{x_0}\right|}{\sqrt{1+\left(\frac{y_0}{x_0}\right)^2}}B \qquad (x_0 > 0, y_0 > 0) \tag{4.4a}$$

$$B_y = \frac{1}{\sqrt{1+\left(\frac{y_0}{x_0}\right)^2}}B \qquad (x_0 > 0, y_0 > 0) \tag{4.4b}$$

In other quadrants, we can obtain the magnetic flux density by modifying the sign of Eqs. (4.4a) and (4.4b) based on Fig. 4.12. By translating the obtained magnetic flux density to the position of the contact probe, the magnetic flux density can be obtained at each point.

Next, we describe the method of estimating the magnetic flux density generated by the PCB. The PCB pattern has a fan-like shape. For simplicity, this pattern is approximated

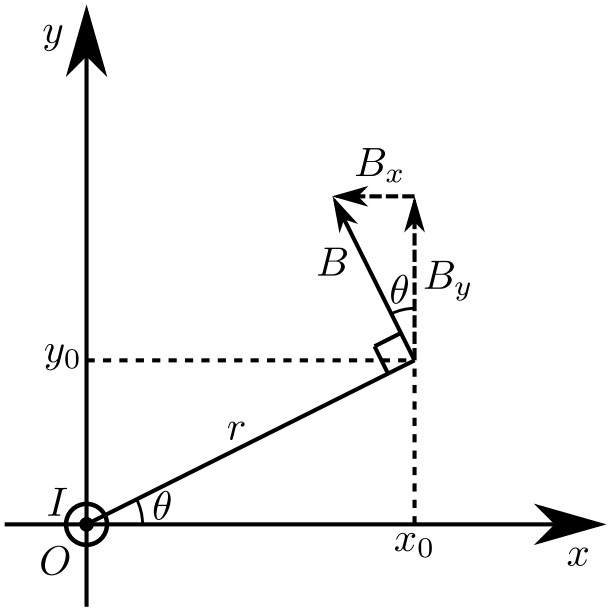

Figure 4.12: Schematic of relationship between current flowing along contact probe and magnetic flux density.

as a straight conductor. The PCB provides x, y, and z components of the magnetic flux density because the PCB and the estimation plane do not intersect vertically. We consider the magnetic flux density as provided by a straight conductor parallel to the x-axis. The magnetic flux density exists only in y and z components under this condition. The magnetic flux density of the y component is given by Eq. (4.5).

$$B_y = \frac{B}{\sqrt{1 + \left(\frac{y_0}{z_0}\right)^2}} \tag{4.5}$$

Therefore, by translating the obtained magnetic flux density to the position of the contact probe, the magnetic flux density is obtained at each point.

Figure 4.13 shows the contour plot of the internal magnetic flux density distribution obtained by the numerical estimation. The internal magnetic flux density in Fig. 4.13 shows qualitatively similar features to Fig. 4.8(b). There is a discrepancy between the measured and modeled magnitudes of the magnetic flux density. This is due to the manufacturing accuracy of the search coil. In order to discuss the magnetic flux density quantitatively, the area-turn product of the search coil must inevitably be calibrated by a Helmholtz coil [77, 78]. On the other hand, it is of greater importance to investigate whether the spatial difference in the measured magnetic flux density corresponds to the

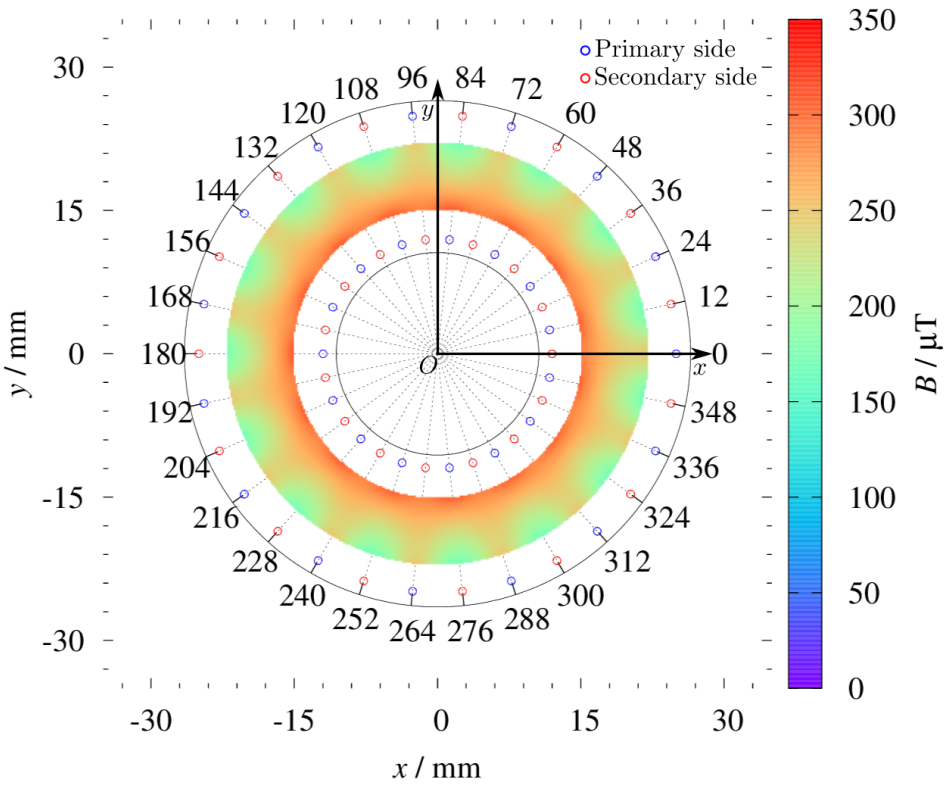

Figure 4.13: Numerically obtained internal magnetic flux density in air-core transformer. Numbers around the circle denote angle. Blue circles denote primary side contact probes, and red circles secondary side contact probes.

winding structure. The relative value becomes a more critical factor for choosing the winding structure, considering the magnetic flux density. Therefore, it is necessary to verify the relative value of the magnetic flux density.

Figure 4.14 shows the experimentally and numerically obtained magnetic flux density as a function of angle in the air-core transformer. The blue points show the experimental results, while the red points display the results of the numerical estimation. In order to compare the relative values, the results of the numerical estimation were multiplied by 1.5. The relative values of the experimental result and the numerical estimation are in good agreement for the spatial frequency as well as for the normalized amplitude at every radius value. This result supports the validity of the proposed measurement method.

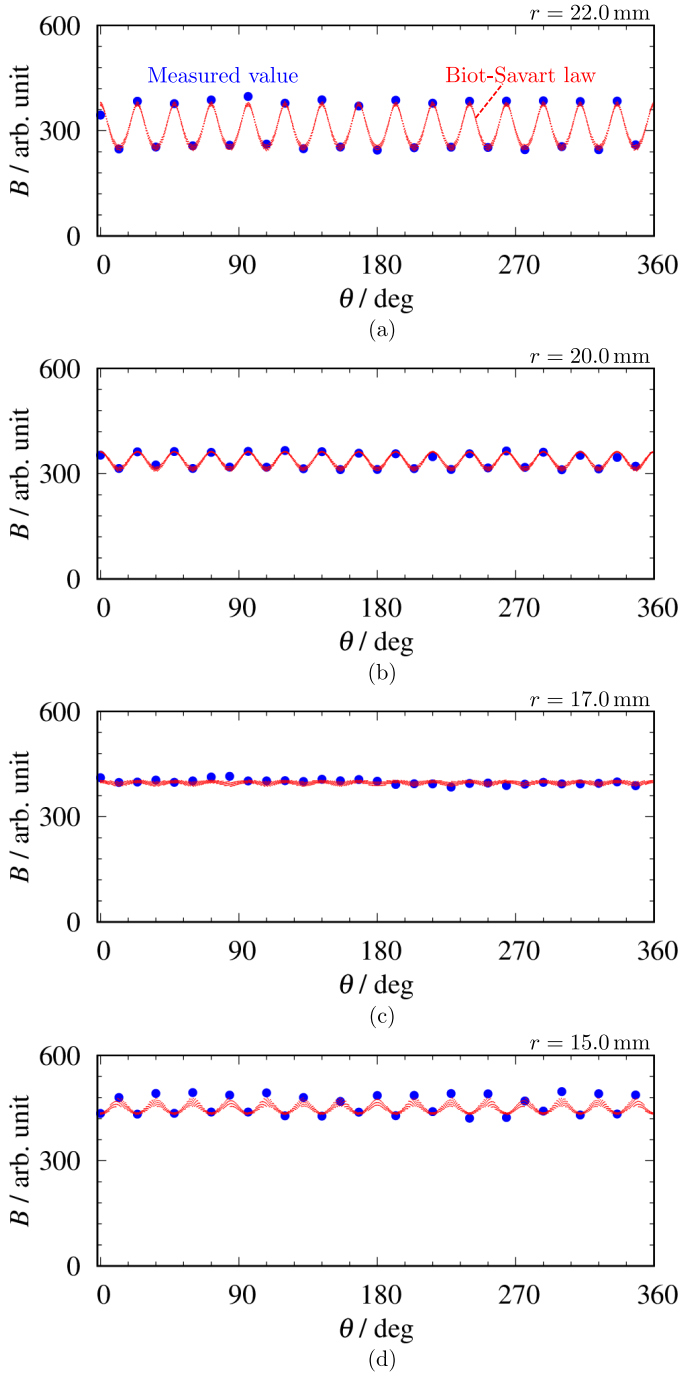

Figure 4.14: Comparison of experimental results and numerical estimation for internal magnetic flux density as a function of angle in air-core transformer for: (a) $r = 22.0\,\mathrm{mm}$, (b) $r = 20.0\,\mathrm{mm}$, (c) $r = 17.0\,\mathrm{mm}$, and (d) $r = 15.0\,\mathrm{mm}$. Blue points denotes experimental results, and red points results of numerical estimation. Results of the numerical estimation were multiplied by 1.5 to compare relative values.

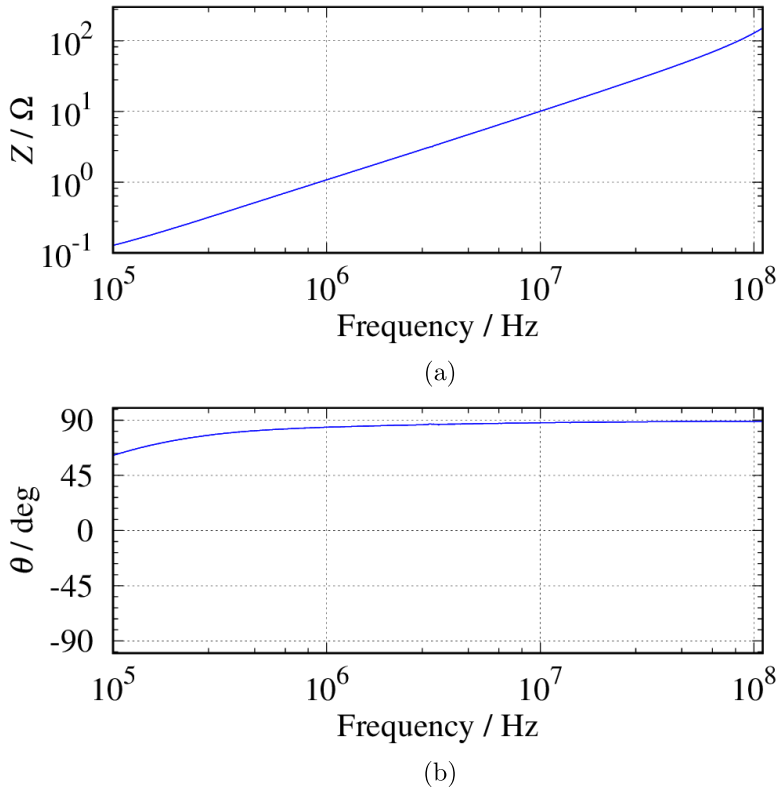

Figure 4.15: Frequency response of search coil: (a) impedance and (b) phase.

4.5 Effect of measurement equipment impedance

First, we discuss the effect of the parasitic capacitance in the fabricated search coil. Figure 4.15 shows the frequency response of the fabricated search coil. The frequency response was measured with an impedance analyzer (Keysight Technologies, 4294A). As shown in Fig. 4.15(a), the impedance exhibits a linear response to frequencies. The phase is approximately 90 degrees from 1 to 110 MHz. Therefore, the fabricated search coil acts as a magnetic component in that frequency range.

Figure 4.16 shows the comparison of the measured waveforms in various excitation frequencies. The blue line indicates the measured magnetic flux density at 100 kHz, the red line at 1 MHz, and the green line at 10 MHz. For the excitation at 10 MHz, we used another bipolar power supply (NF CORPORATION, HSA4101), which can operate up to 10 MHz. That is because the bipolar power supply (HSA4011) described in Section 4.2 can only apply a sinusoidal wave in the frequency ranging up to 1 MHz. Time axis is normalized by excitation frequencies in order to compare them. In Fig. 4.16(a), the

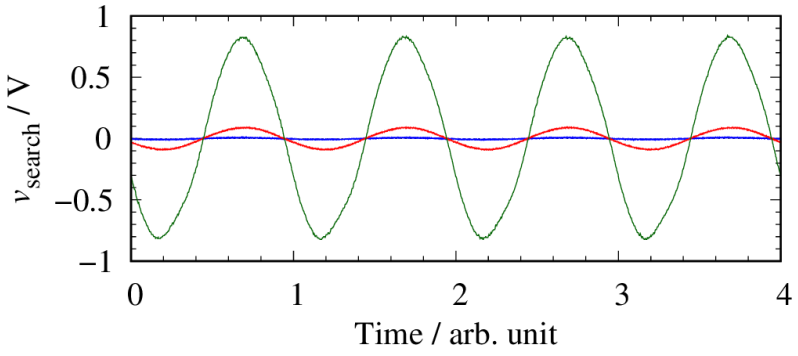

(a)

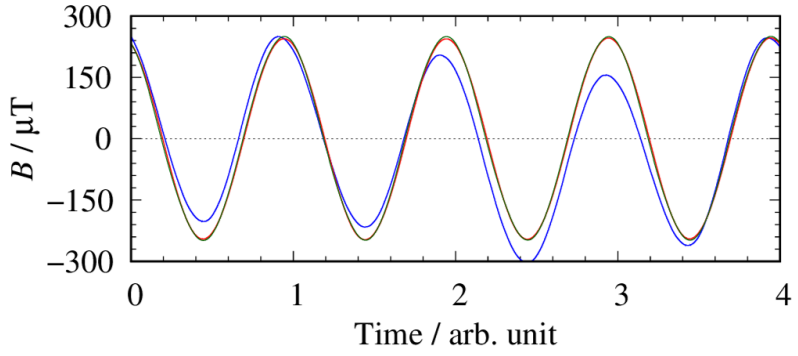

(b)

Figure 4.16: Comparison of measured waveforms in various excitation frequencies: (a) search coil voltage and (b) magnetic flux density. Blue line denotes measured waveforms at 100 kHz, red line at 1 MHz, and green line at 10 MHz. Time axis is normalized by excitation frequencies to compare them.

search coil voltage can be clearly confirmed at 1 and 10 MHz, while it cannot be confirmed at 100 kHz. This is consistent with the explanation in Section 4.2. In Fig. 4.16(b), the magnetic flux density at 10 MHz is identical to measured waveforms at 1 MHz. That is because the search coil acts as a magnetic component at 10 MHz. On the other hand, the measured waveform at 100 kHz is not identical to them. The reason is that the isolated probe cannot measure the search coil output voltage correctly at several mV in addition to the search coil does not act as a magnetic component at 100 kHz. Therefore, the parasitic capacitance in the search coil can be neglected in the frequency ranging up to 110 MHz.

Next, we discuss the effect of the input impedance of an isolated probe. The isolated probe used in this dissertation can replace the sensor tip cable. For measuring in several tens of mV range, IVTIP1X and MMCX10X sensor tip cables are suitable and their specifications are listed in Table 4.1. IVTIP1X sensor tip cable was used in Section 4.3.

Table 4.1: List of specifications of sensor tip cable

Sensor tip cable	Differential input voltage	Input impedance
IVTIP1X	±1 V (2X range)	1 MΩ||35 pF
MMCX10X	±5 V (1X range)	10 MΩ||6 pF

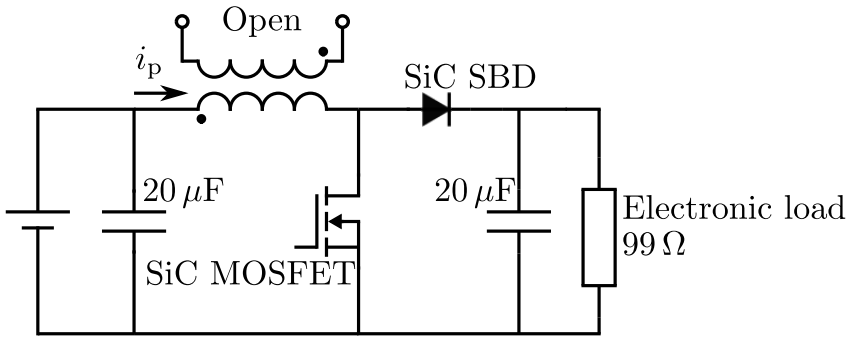

Figure 4.17: A schematic of experimental circuit to excite an air-core transformer in high-frequency switching conditions.

Although it is more suitable than MMCX10X for measuring in several tens of mV range, it could not be suitable for high-frequency measurement because its input impedance is larger than the impedance of MMCX10X.

Since the developed method is used to analyze the behavior of the magnetic flux of power converters, this section investigates the effect of the impedance of the probe based on the measurement results when the air-core transformer is excited with a waveform containing harmonic components. Figure 4.17 shows the experimental circuit. The circuit topology is a boost type with the transformer as a reactor. The triangular current including harmonic components flows through the air-core transformer. The air-core transformer is the same one used in Chapter 2 and 3. A SiC MOSFET (ROHM, SCT3120AL) is adopted as a active switching device and a SiC SBD (ROHM, SCS206AM) as a rectifying device. The SiC MOSFET is driven with an isolated gate driver (Silicon Labs., Si8235).

Figure 4.18 shows the photographs of the experiment. For the purpose of this section, the search coil shown in Fig. 4.18(c) is used. Six types of the search coil are fabricated. The number of turns is set at three to eight turns for each search coil, and the cross section at 2.6 mm^2 for every search coil. The cross section was determined on the basis of the results of Section 4.3. The search coil is combined with the base, implemented into the air-core transformer as shown in Figs. 4.18(b) and (d). Since the search coil and base

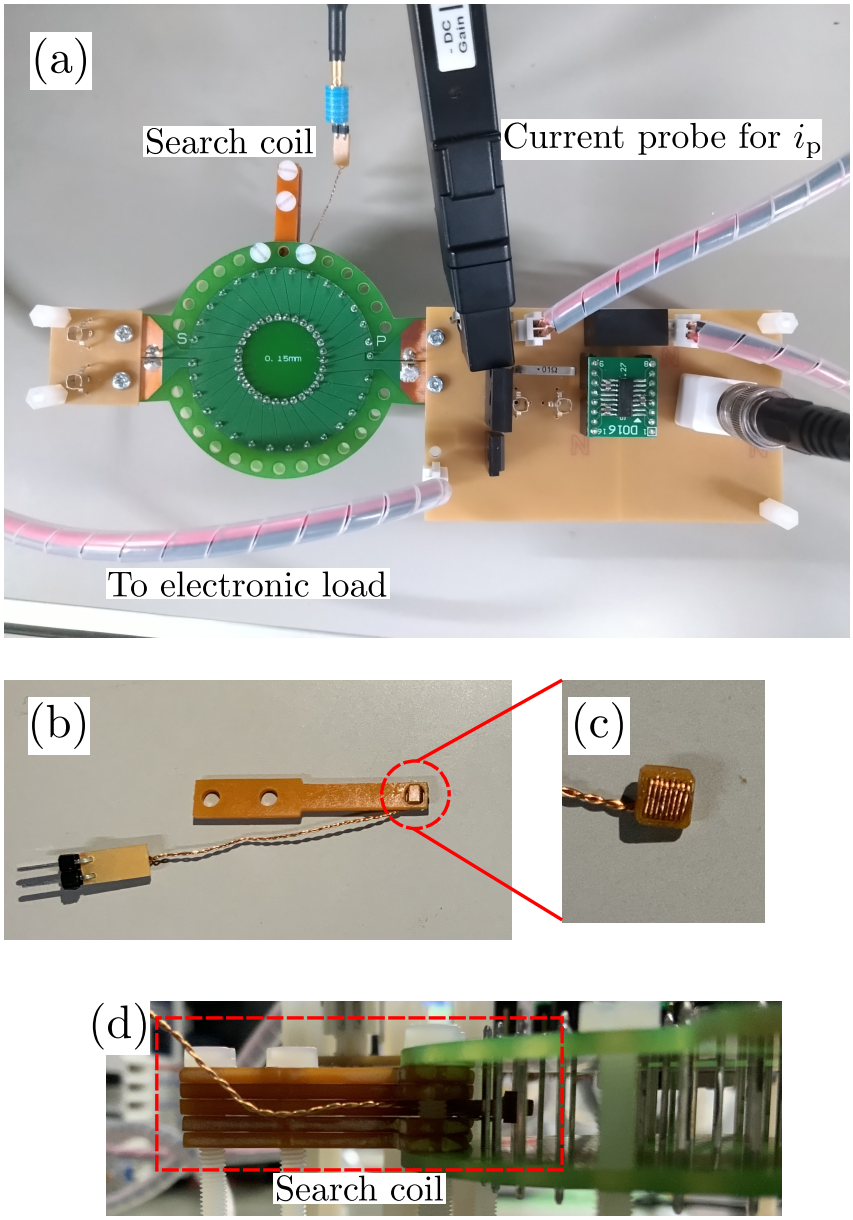

Figure 4.18: Photographs of experiment: (a) experimental circuit, (b) search coil with base, (c) fabricated search coil, and (d) implemented into air-core transformer.

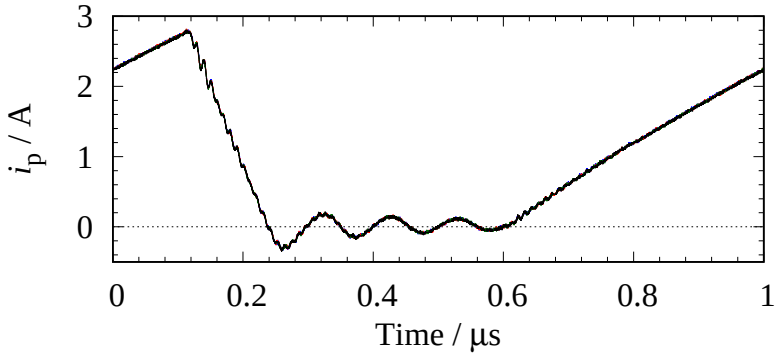

Figure 4.19: Comparisons of experimentally obtained waveforms of input current. The blue line shows the current when measuring with the three turns search coil and IVTIP1X, the red line the current when measuring with the three turns search coil and MMCX10X, the green line the current when measuring with the eight turns search coil and IVTIP1X, and the black line the current when measuring with the eight turns search coil and MMCX10X.

are separable, the direction of the search coil can be changed. The magnetic flux density coil can be measured with one search coil for the tangential and normal components.

The setting of the experiment is described as follows. A peak value of the input current i_p is set to 2.8 A and the switching frequency of the SiC MOSFET at 1 MHz with duty ratio of 50%. The search coil is located at (r, θ, z)=(15.0 mm, 90 deg, 5.6 mm). The internal magnetic flux density is measured for the tangential component. The excitation current is measured with a current probe (Tektronix, TCP0030A). The above measurements were carried out for each combination of the search coil and the sensor tip cable.

Figure 4.19 shows the comparisons of experimentally obtained waveforms of the input current. The blue line shows the current when measuring with the three turns search coil and IVTIP1X, the red line the current when measuring with the three turns search coil and MMCX10X, the green line the current when measuring with the eight turns search coil and IVTIP1X, and the black line the current when measuring with the eight turns search coil and MMCX10X. It can be seen that all the measured waveforms are identical. This indicates that the inserted search coil do not change the excitation conditions.

Figure 4.20 shows the comparisons of the experimentally obtained waveforms of the search coil voltage. The search coil voltages are normalized by each number of turns. Since the search coil voltage is proportional to the number of turns, the normalized search coil voltage theoretically becomes the same voltage. The above figure shows the comparison of

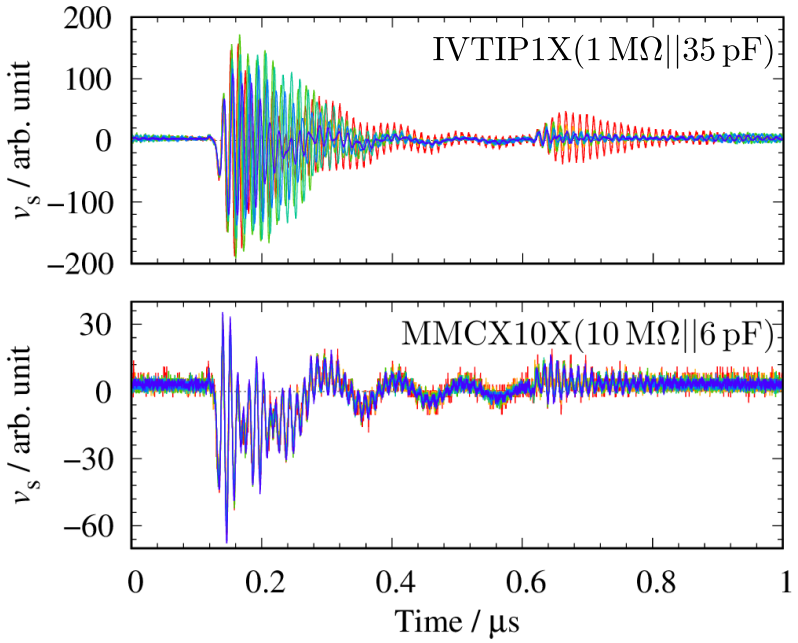

Figure 4.20: Comparisons of experimentally obtained waveforms of search coil voltage. The above figure shows the comparison of search coil voltage measured with IVTIP1X, and the below one the comparison of search coil voltage measured with MMCX10X.

search coil voltage measured with IVTIP1X, while the one below describes the comparison of search coil voltage measured with MMCX10X. It can be seen that the high-frequency oscillations of the search coil voltage are not identical in IVTIP1X. It is seen that all the search coil voltage are identical in MMCX10X. This indicates that the input impedance of the sensor tip cable cannot neglected in IVTIP1X. Therefore, the search coil voltage is measured with MMCX10X in the following chapters.

4.6 Summary

In this chapter, we developed a measurement method for the internal magnetic flux density distribution in an air-core transformer. The magnetic flux density was measured with the fabricated search coil. We verified the validity of the developed method with the internal magnetic flux density distribution measured under 1 MHz sinusoidal excitation. The magnetic flux density was found to be non-uniform in the air-core transformer. The non-uniformity was caused by the transformer structure and not by the measurement method. The obtained distribution was verified through a comparison of with numerical

estimation by the Biot-Savart law. As a result, it was found that the distribution can be measured accurately by the developed method. In addition, the effect of the measurement equipment impedance was discussed. It was found that the parasitic capacitance of the search coil can be neglected. We confirmed that the sensor tip cable (MMCX10X) is suitable for evaluating the air-core transformer in high-frequency power converter applications. In this experiment, interesting high-frequency oscillations were confirmed in the search coil voltage. This is discussed in the next chapter in detail.

The internal magnetic flux density distribution has never been investigated experimentally in detail for various technical reasons. Therefore, the internal magnetic flux density has only been studied as a black box even though it is a key factor governing the performance of a transformer. The measurements given in this chapter are also significant in terms of carrying the investigation of the internal magnetic flux density a stage further. For example, the distribution obtained in this chapter can be used as a reference when analyzing the behavior of magnetic flux in the high-frequency range. The internal magnetic flux density distribution in this dissertation does not depend on the excitation waveform and frequency, as long as there is current flow along the winding. When the current distribution changes for some reasons, such as the impacts of stray capacitances, the magnetic flux density also changes. That is, we can investigate the behavior in the high-frequency range by comparing the distribution given in this chapter with one obtained from high-frequency measurement.

Chapter 5

High-frequency oscillation of internal magnetic flux density

This chapter investigates the behavior of the internal magnetic flux density under high-frequency switching conditions. The high-frequency oscillation is confirmed in the search coil voltage from the results of Chapter 4. The frequency of the oscillation is estimated to be several tens of megahertz. Since the air-core transformer has the resonance in the frequency range of several tens of megahertz, the oscillation is most likely caused by the characteristics of the air-core transformer. As mentioned in Chapter 4, it has been reported that the magnetic flux density distribution changes around the resonant frequency [70]. The change in the distribution implies the change in the characteristics of the air-core transformer. This leads to unintended converter behavior. Therefore, it is important to investigate the cause of the oscillation for designing the air-core transformer and the power converter.

In Section 5.1, the experimental setup is described. In Section 5.2, the behavior of the internal magnetic flux density is discussed. The cause of the high-frequency oscillation is investigated in Section 5.3.

5.1 Experimental setup

The investigation is similar to the experiment in Chapter 4. The schematics and details of the experiment are described in Chapter 4. In the following, only the changes are described. The purpose of the experiment is different from Chapter 4. In this chapter, we focus on revealing the cause of the high-frequency oscillation. To confirm whether the high-frequency oscillation is unique to the air-core transformer, the air-core inductor,

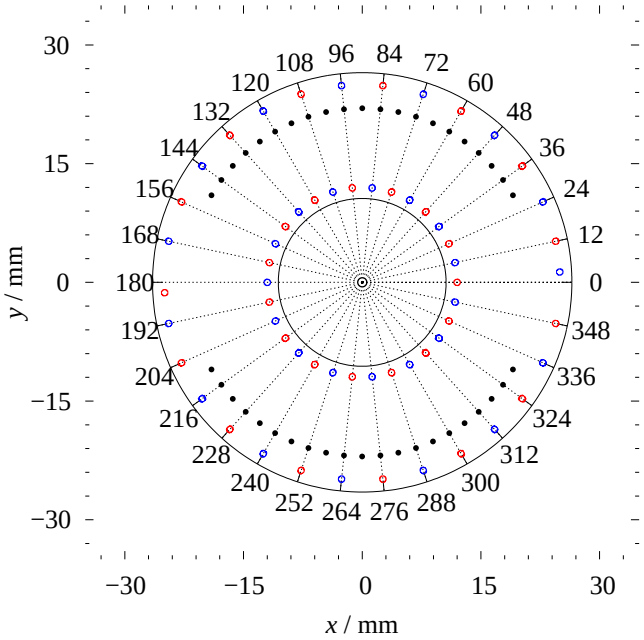

Figure 5.1: Measurement points in air-core transformer. Numbers around the circle denote angle. Blue circles denote primary side windings and red circles denote secondary side windings.

which is used in Chapter 3, is also tested under the same conditions. A peak value of the input current i_{p} is set to 3.5 A, and the switching frequency of the SiC MOSFET set to 1 MHz with duty ratio of 30%. Figure 5.1 shows the measurement points used in this chapter. The internal magnetic flux density is measured for the tangential and normal components.

5.2 Behavior of internal magnetic flux density

5.2.1 Air-core inductor

This subsection describes the measured results of the internal magnetic flux density in the air-core inductor. Figure 5.2 shows the experimentally obtained waveforms of the input current in the air-core inductor. Figures 5.2(a) and (b) show the waveforms when measuring the internal magnetic flux densities for the tangential and normal component at (r, θ, z)=(15.0 mm, 90 deg, 5.6 mm), respectively. In Fig. 5.2(a), the input current increased linearly during the on-state of the SiC MOSFET. The magnetic energy was stored

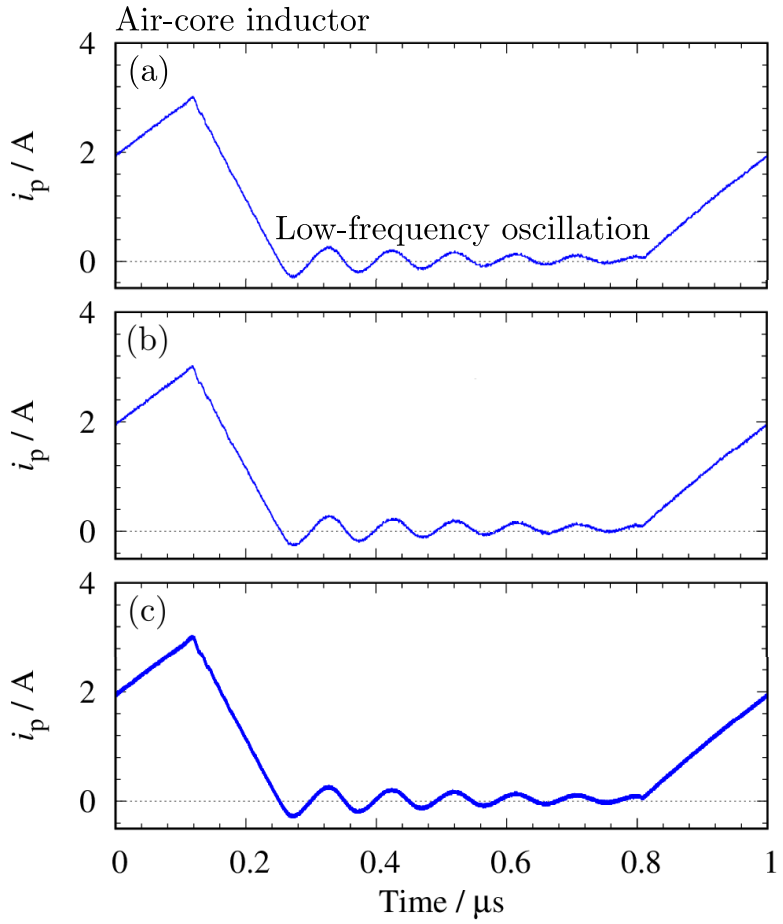

Figure 5.2: Experimentally obtained waveforms of input current in air-core inductor. (a) and (b) show the waveforms when measuring the internal magnetic flux densities for the tangent and normal component at (r, θ, z)=(22.0 mm, 90 deg, 5.6 mm), respectively. (c) shows a superposition of all the measured waveforms when measuring the internal magnetic flux density for the tangential component.

in the air-core inductor at the period. After the SiC MOSFET was turned off, the stored magnetic energy was supplied to the load. There was no magnetic energy in the air-core inductor after the input current reached zero. Then the input current oscillated at a low frequency. The similar waveform is confirmed in Fig. 5.2(b). These are typical waveforms that can be confirmed in a boost converter. Figures 5.2(c) shows a superposition of all the measured waveforms when measuring the internal magnetic flux density for the tangential component. It can be seen that all the measured waveforms are identical. This indicates that the position of the inserted search coil did not change the excitation conditions.

Figure 5.3 shows the experimentally obtained waveforms of the search coil voltage

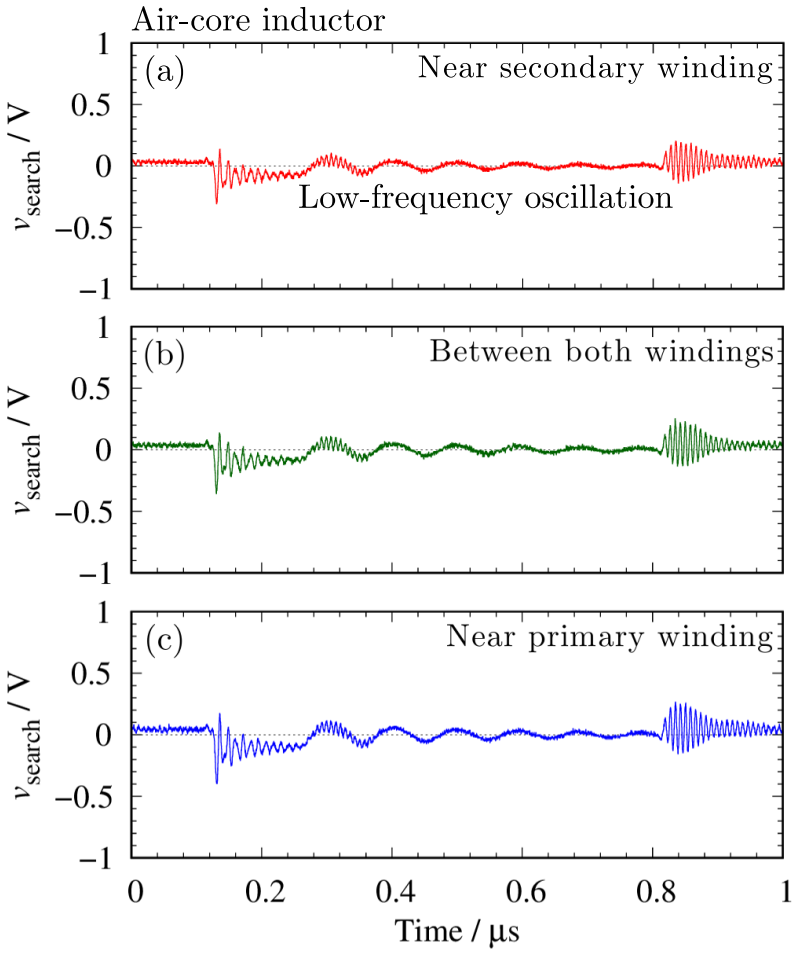

Figure 5.3: Experimentally obtained waveforms of search coil voltage for tangential component in air-core inductor. The red line shows the waveforms measured at (r, θ, z)=(22.0 mm, 84 deg, 5.6 mm), the green line the measured waveform at (r, θ, z)=(22.0 mm, 90 deg, 5.6 mm), and the blue line the measured waveform at (r, θ, z)=(22.0 mm, 96 deg, 5.6 mm).

for the tangential component in the air-core inductor. The red line shows the measured waveform at (r, θ, z)=(22.0 mm, 84 deg, 5.6 mm), the green line the measured waveform at (r, θ, z)=(22.0 mm, 90 deg, 5.6 mm), and the blue line the measured waveform at (r, θ, z)=(22.0 mm, 96 deg, 5.6 mm). The search coil voltages oscillated at a low frequency. It corresponds to the oscillation in the input current. Immediately after turning the SiC MOSFET on and off, the search coil voltage oscillated at high frequency. However, the high-frequency oscillation is different from the waveforms measured in Chapter 4.

Figure 5.4 shows the experimentally obtained waveforms of the search coil voltage for the normal component in the air-core inductor. The red line shows the measured

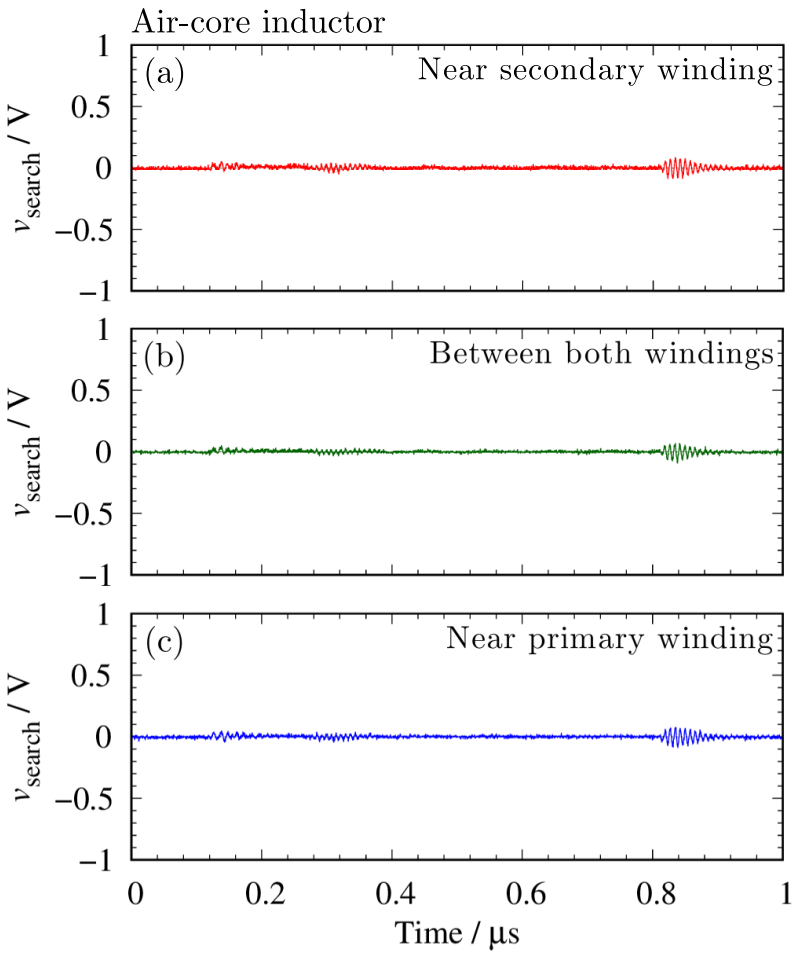

Figure 5.4: Experimentally obtained waveforms of search coil voltage for normal component in air-core inductor. The red line shows the waveforms measured at (r, θ, z)=(22.0 mm, 84 deg, 5.6 mm), the green line the measured waveform at (r, θ, z)=(22.0 mm, 90 deg, 5.6 mm), and the blue line the measured waveform at (r, θ, z)=(22.0 mm, 96 deg, 5.6 mm).

waveform at (r, θ, z)=(22.0 mm, 84 deg, 5.6 mm), the green line the measured waveform at (r, θ, z)=(22.0 mm, 90 deg, 5.6 mm), and the blue line the measured waveform at (r, θ, z)= (22.0 mm, 96 deg, 5.6 mm). Unlike the tangential component, the search coil voltage cannot be clearly confirmed. This indicates that the magnetic flux density for the tangential component is dominant in the air-core inductor as with the results of Chapter 4. Therefore, we only discuss the tangential component.

Figure 5.5 shows the magnetic flux density for the tangential component calculated from the search coil voltage in the air-core inductor. The blue lines show the waveforms measured near the primary winding such as at (r, θ, z)=(22.0 mm, 96 deg, 5.6 mm), the

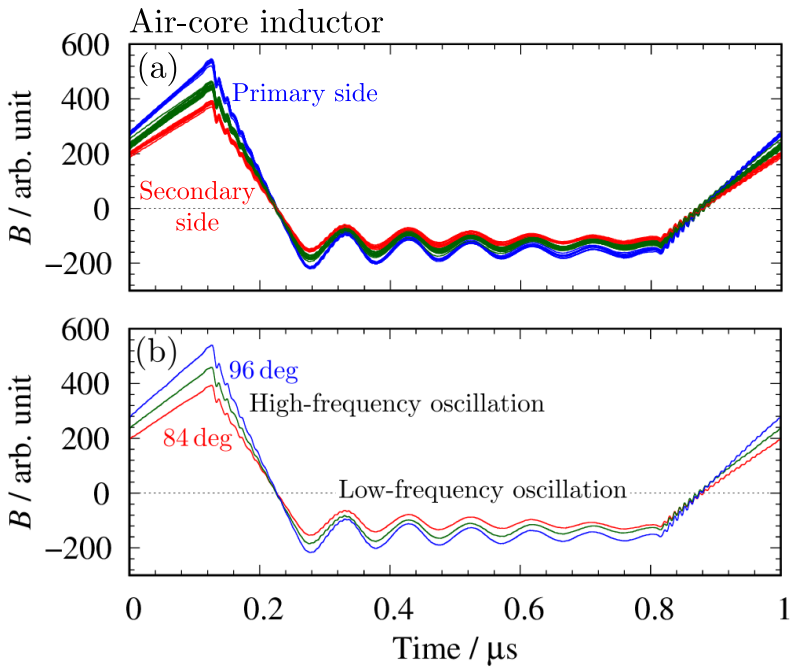

Figure 5.5: Magnetic flux density for tangential component calculated from search coil voltage in air-core inductor. The blue lines show the waveforms measured near the primary winding such as at (r, θ, z)=(22.0 mm, 96 deg, 5.6 mm), the green lines the waveforms measured between the primary and secondary windings such as at (r, θ, z)=(22.0 mm, 90 deg, 5.6 mm), the red lines the waveforms measured near the secondary winding such as at (r, θ, z)=(22.0 mm, 84 deg, 5.6 mm). (b) shows the excerpt of the waveforms measured at 84 to 96 deg.

green lines the waveforms measured between the primary and secondary windings such as at (r, θ, z)=(22.0 mm, 90 deg, 5.6 mm), the red lines the waveforms measured near the secondary winding such as at (r, θ, z)=(22.0 mm, 84 deg, 5.6 mm). Note that the magnetic flux densities are plotted with an arbitrary unit because the search coil can measure only the variation of the magnetic flux density. It can be seen that the magnetic flux densities are classified into three types. In each type, the magnetic flux density showed the same waveform. Hereinafter, we discuss the magnetic flux density based on the waveform measured at 84, 90, and 96 deg as an example of each type. Figure 5.5(b) shows the excerpt of the waveforms measured at 84 to 96 deg. The magnetic flux density showed a similar waveform to the input current, while the high-frequency oscillation occurred. Here, let us check Fig. 5.2 again. It can be seen that there are traces of high-frequency oscillations in the input current. The search coil is more sensitive to high-frequency signals than the current probe due to the characteristics of the measurement method. This is

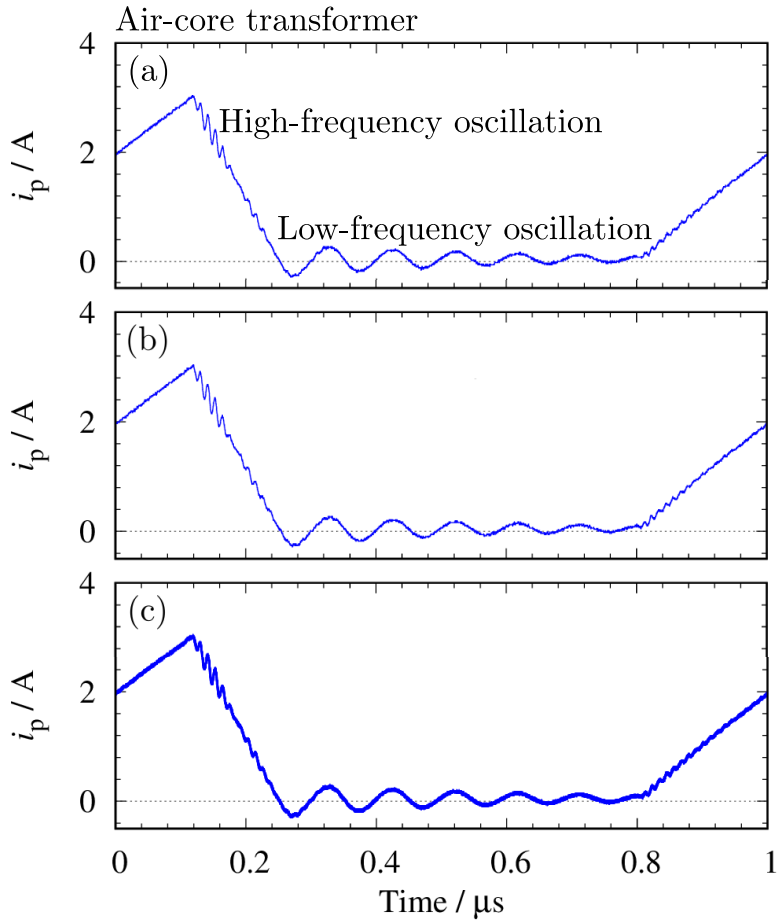

Figure 5.6: Experimentally obtained waveforms of input current in air-core transformer. (a) and (b) show the waveforms when measuring the internal magnetic flux densities for the tangent and normal component at (r, θ, z)=(22.0 mm, 90 deg, 5.6 mm), respectively. (c) shows a superposition of all the measured waveforms when measuring the internal magnetic flux density for the tangential component.

why the high-frequency oscillations appeared more clear in the magnetic flux density than the input current. The amplitude of the search coil voltage is larger as the measured point approaches the primary winding from the secondary winding as with the search coil voltage. This is also consistent with the results of Chapter 4.

5.2.2 Air-core transformer

This subsection describes the measured results of the internal magnetic flux density in the air-core transformer. Figure 5.6 shows the experimentally obtained waveforms of the input current in the air-core transformer. Figures 5.6(a) and (b) show the waveforms

when measuring the internal magnetic flux densities for the tangential and normal component at (r, θ, z)=(22.0 mm, 90 deg, 5.6 mm), respectively. In Fig. 5.6(a), the input current showed the similar waveform to Fig. 5.2. However, the high-frequency oscillation can be confirmed clearly after the MOSFET is turned off. The similar waveform is confirmed in Fig. 5.6(b). The oscillation is not seen in the air-core inductor. This implies that the high-frequency characteristics of the air-core transformer affect the switching operation. Figures 5.2(c) shows a superposition of all the measured waveforms when measuring the internal magnetic flux density for the tangential component. It can be seen that all the measured waveforms are identical. This indicates that the position of the inserted search coil did not change the excitation conditions even though the high-frequency oscillation occurs.

Figure 5.7 shows the experimentally obtained waveforms of the search coil voltage for the tangential component in the air-core transformer. The red line shows the measured waveform at (r, θ, z)=(22.0 mm, 84 deg, 5.6 mm), the green line the measured waveform at (r, θ, z)=(22.0 mm, 90 deg, 5.6 mm), and the blue line the measured waveform at (r, θ, z)=(22.0 mm, 96 deg, 5.6 mm). Unlike the air-core inductor, the large high-frequency oscillation is confirmed. The amplitude of the high-frequency oscillation is the largest in Fig. 5.7(a). In the air-core inductor, the search coil voltage measured near the primary winding was the largest, regardless of the frequency component. This implies that the behaviors of the magnetic flux density changes.

Figure 5.8 shows the experimentally obtained waveforms of the search coil voltage for the normal component in air-core transformer. The red line shows the measured waveform at (r, θ, z)=(22.0 mm, 84 deg, 5.6 mm), the green line the measured waveform at (r, θ, z)=(22.0 mm, 90 deg, 5.6 mm), and the blue line the measured waveform at (r, θ, z)= (22.0 mm, 96 deg, 5.6 mm). The search coil voltage cannot be confirmed, except for the high-frequency oscillation in Fig. 5.8(b). The high-frequency oscillation seemingly occurs owing to the high-frequency characteristics of the air-core transformer. In this subsection, we only discuss the tangential component in order to compare with the result of the air-core inductor. Note that this fact is important to discuss the high-frequency flyback converter designed in Chapter 6.

Figure 5.9 shows the magnetic flux density for the tangential component calculated from the search coil voltage in the air-core transformer. The blue lines show the waveforms measured near the primary winding such as at (r, θ, z)=(22.0 mm, 96 deg, 5.6 mm), the

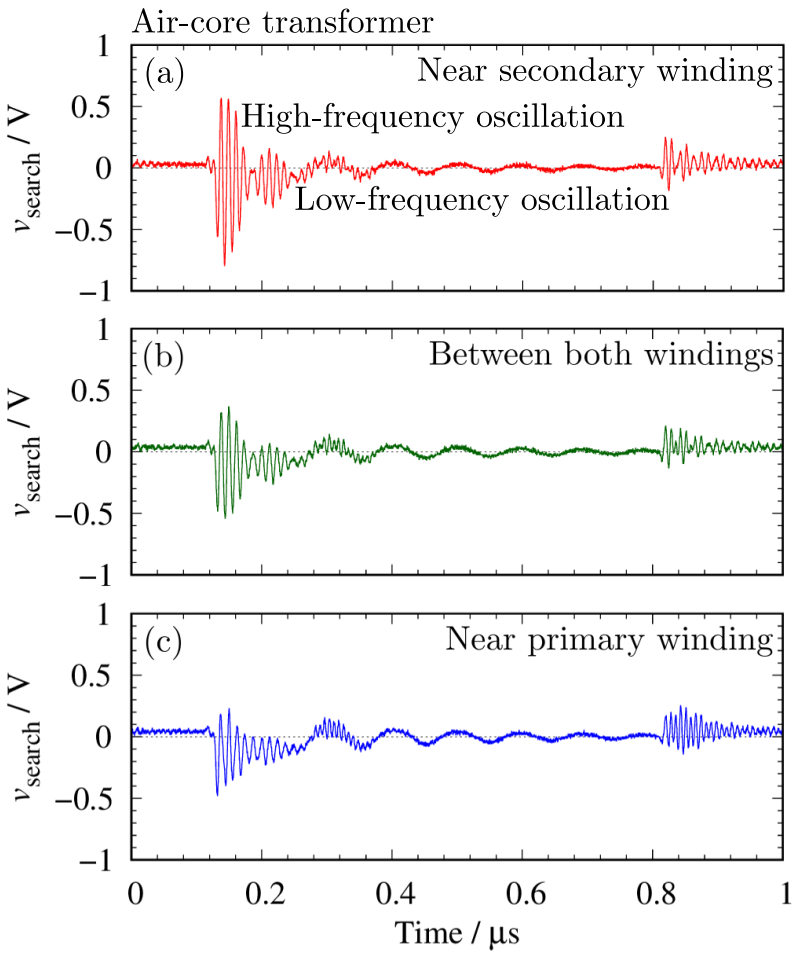

Figure 5.7: Experimentally obtained waveforms of search coil voltage for tangential component in air-core transformer. The red line shows the waveforms measured at (r, θ, z)=(22.0 mm, 84 deg, 5.6 mm), the green line the measured waveform at (r, θ, z)=(22.0 mm, 90 deg, 5.6 mm), and the blue line the measured waveform at (r, θ, z)=(22.0 mm, 96 deg, 5.6 mm).

green lines the waveforms measured between the primary and secondary windings such as at (r, θ, z)=(22.0 mm, 90 deg, 5.6 mm), the red lines the waveforms measured near the secondary winding such as at (r, θ, z)=(22.0 mm, 84 deg, 5.6 mm). As with the air-core inductor, the magnetic flux densities are classified into three types, showing the same waveform in each type. Hereinafter, we discuss the magnetic flux density based on the waveform measured at 84, 90, and 96 deg as an example of each type. Figure 5.5(b) shows the excerpt of the waveforms measured at 84 to 96 deg. The magnetic flux density showed the similar waveform to the input current. The amplitude of the magnetic flux density is larger as the measured point approaches the primary winding from the secondary winding,

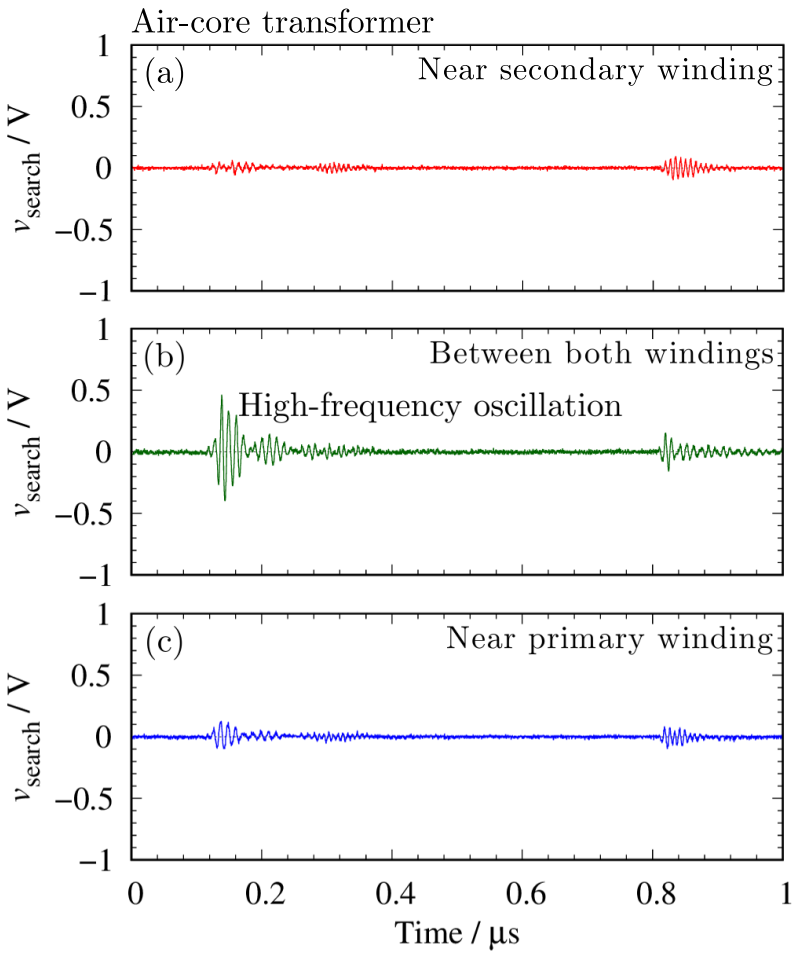

Figure 5.8: Experimentally obtained waveforms of search coil voltage for normal component in air-core transformer. The red line shows the waveforms measured at (r, θ, z)=(22.0 mm, 84 deg, 5.6 mm), the green line the measured waveform at (r, θ, z)=(22.0 mm, 90 deg, 5.6 mm), and the blue line the measured waveform at (r, θ, z)=(22.0 mm, 96 deg, 5.6 mm).

while the amplitude of the high-frequency oscillation is smaller. This indicates that the behavior of the magnetic flux density changes in that frequency. The change also appeared in the secondary winding voltage.

Figure 5.10 shows the comparison of the primary voltage with the secondary voltage measured in the air-core transformer. The red line shows the primary voltage and the blue line the secondary voltage. The primary voltage was calculated from the difference between the input voltage and the drain-source voltage of the SiC MOSFET, and the secondary voltage calculated from the difference between the measured voltages of the two passive probes. In periods I and III, the voltage amplitude is larger in the primary

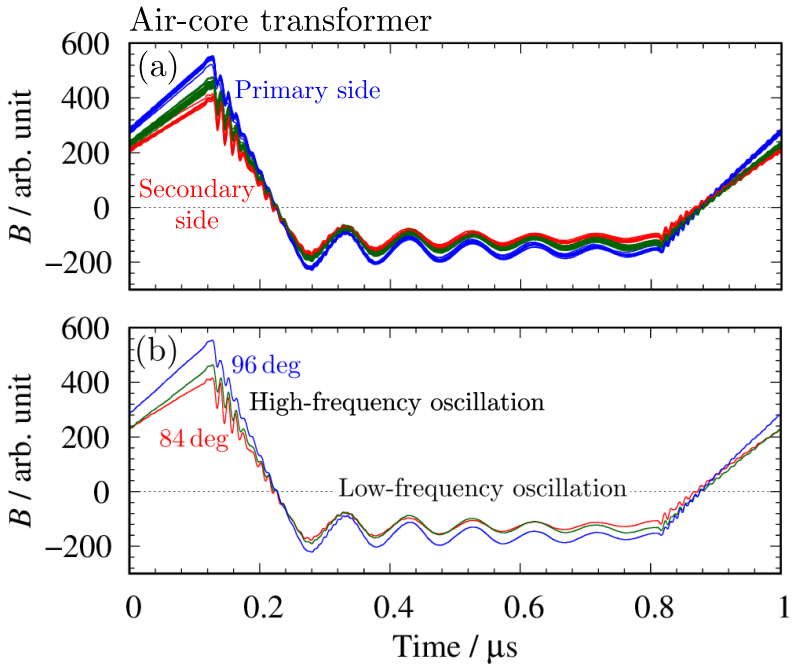

Figure 5.9: Magnetic flux density for tangential component calculated from search coil voltage in air-core transformer. The blue lines show the waveforms measured near the primary winding such as at (r, θ, z)=(22.0 mm, 96 deg, 5.6 mm), the green lines the waveforms measured between the primary and secondary windings such as at (r, θ, z)=(22.0 mm, 90 deg, 5.6 mm), the red lines the waveforms measured near the secondary winding such as at (r, θ, z)=(22.0 mm, 84 deg, 5.6 mm). (b) shows the excerpt of the waveforms measured at 84 to 96 deg.

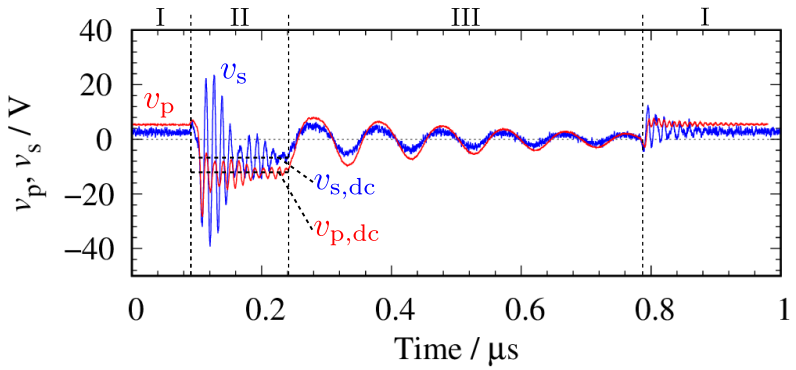

Figure 5.10: Comparison of primary voltage with secondary voltage measured in air-core transformer. The red line shows the primary voltage, and the blue line the secondary voltage. $v_{p,dc}$ and $v_{s,dc}$ denote the DC component in the period II, respectively.

side than in the secondary side. However, the magnitude relationship is reversed in period II although the DC components keep the magnitude relationship. The coupling coefficient of the fabricated air-core transformer is one or less because its turn ratio is set to one. The secondary voltage cannot become larger than the primary voltage theoretically. This indicates that factors other than the self-inductance and mutual inductance cause the high-frequency oscillation.

5.3 Cause of high-frequency oscillation

This section investigates the cause of the high-frequency oscillation. Figure 5.11 shows the frequency response of $Z_{\mathrm{PP}',\mathrm{open}}$ and the frequency spectrum obtained from the search coil voltage measured at (r, θ, z)=(22.0 mm, 96 deg, 5.6 mm). Two peaks can be confirmed in the frequency range of several tens of megahertz. That is because there is a beat in the search coil voltage as shown in Fig. 5.7(b). The higher peak frequency coincides with the second resonance frequency of the frequency response. This implies that one of the causes of high-frequency oscillation is the second resonance frequency in the air-core transformer.

Suppose that another peak is caused by the parasitic inductance of the experimental circuit. The additional experimental circuits were fabricated in order to investigate the validity of this hypothesis. This section focuses on two parasitic inductances, L_{p1} and L_{p2}, as shown in Fig. 5.12. The same experiment as described in Section 5.1 is carried out for the additional circuits. Figure 5.13 shows the frequency spectrum of the search voltage and the photographs of the additional fabricated experimental circuit. The parasitic inductance was implemented by changing the width of the wiring. The parasitic inductance is the smallest in Fig. 5.13(a) and the largest in Fig. 5.13(d). From the frequency spectrum, the higher peak frequency remains at the same frequency, while the lower peak frequency shifts to the lower frequency side. This indicates that the lower peak frequency depends on the parasitic inductance in the experimental circuit. Therefore, we conclude that the high-frequency oscillation is caused by the second resonance of the frequency response in the air-core transformer and the parasitic inductance in the experimental circuit. This conclusion also indicates that the high-frequency oscillation of the search coil in the air-core inductor (Fig. 5.3) was seemingly caused by the parasitic inductance because the high-frequency oscillation depends on it.

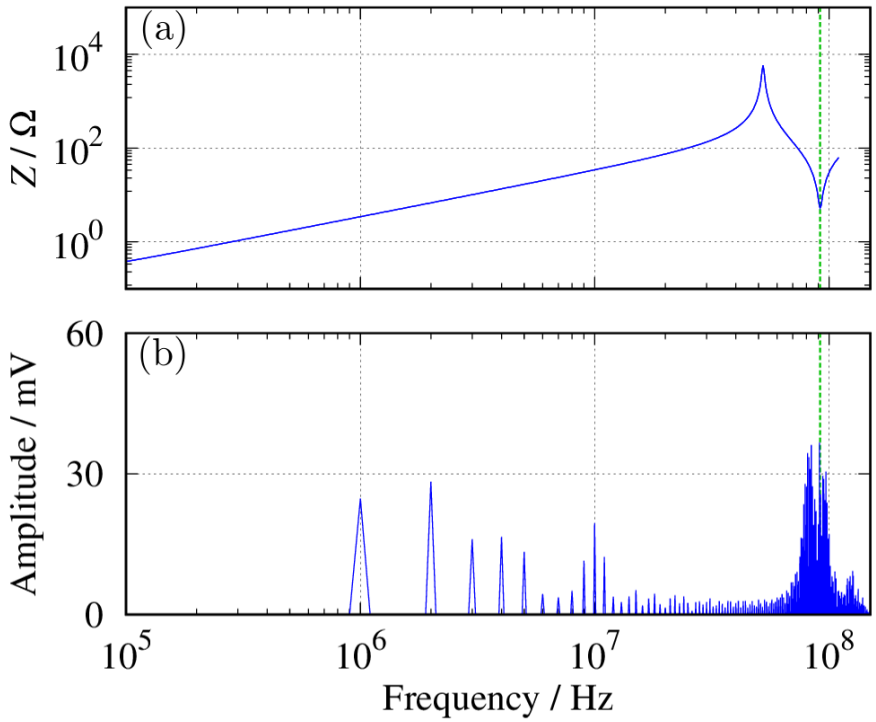

Figure 5.11: Frequency response of $Z_{\mathrm{PP'},\mathrm{open}}$ and frequency spectrum obtained from search coil voltage.

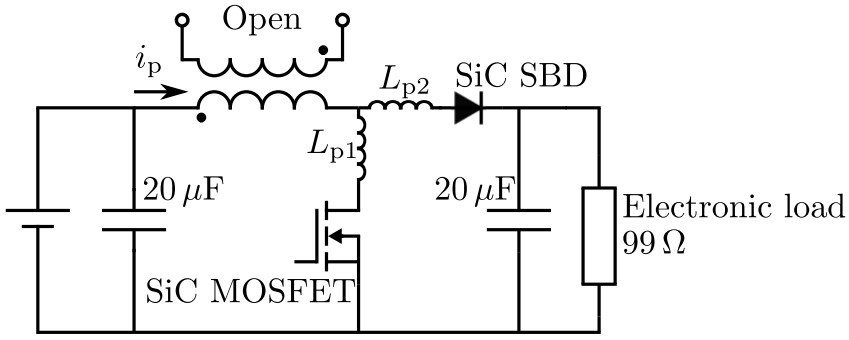

Figure 5.12: A schematic of experimental circuit to investigate effect of parasitic inductance.

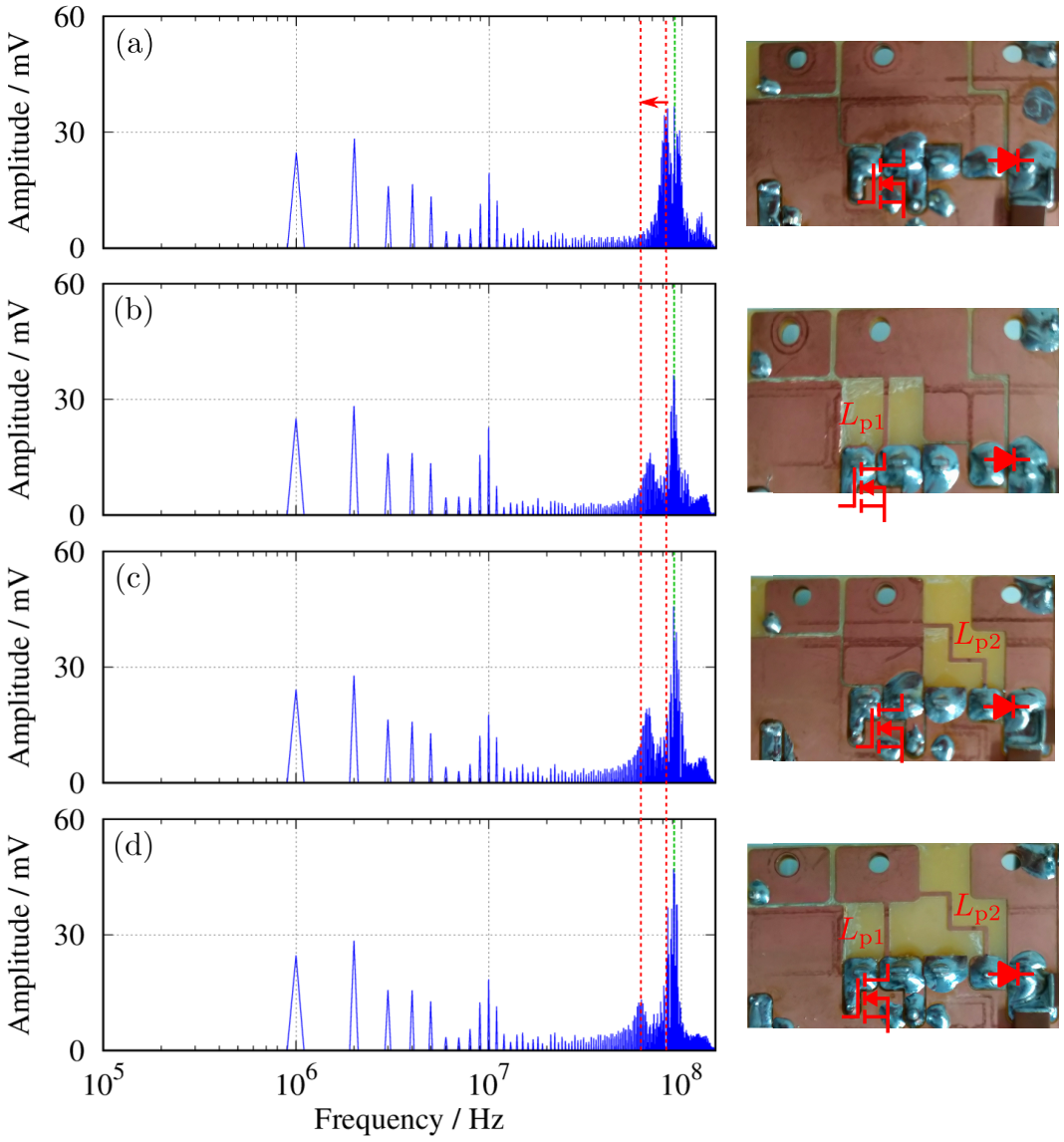

Figure 5.13: Frequency spectrum of search voltage and photographs of additional fabricated experimental circuit: (a) original circuit, (b) circuit increased L_{p1}, (c) circuit increased L_{p2}, and (d) circuit increased L_{p1} and L_{p2}.

5.4 Summary

This chapter investigated the high-frequency oscillation of the internal magnetic flux density under high-frequency switching conditions. The air-core transformer and the air-core inductor were excited by the current including many harmonic components. Compared with both waveforms of the magnetic flux density, it was found that the high-frequency oscillation is an unique phenomenon to the air-core transformer. The amplitude relationship changed when the magnetic flux density oscillated at high frequency. Then we discuss the cause of the high-frequency oscillation. From the comparison between the frequency spectrum of the search coil voltage and the frequency response of the air-core transformer, it was found that the high-frequency oscillation is caused by the resonance frequency of the transformer. Additional experiments were carried out for the additional circuits whose parasitic inductances were varied. As a result, it was found that the high-frequency oscillation also depends on the parasitic inductance in the experimental circuit.

The coupling coefficient of the air-core transformer is estimated to be about 0.6. Nevertheless, the secondary voltage was larger than the primary voltage when the high-frequency oscillation occurred. Similar phenomena can be observed in Tesla coil configuration [79–83]. The transformer is excited with a pulsed voltage in these studies. The high-frequency oscillation also includes a beat. Therefore, they have many points in common with the experimental results in this chapter. In those conditions, the energy is efficiently transferred from the primary to the secondary side. The transformer is excited under an open condition on the secondary side in a flyback converter during the on-state of the active switch. The excitation condition is similar to the experiment in this chapter. Above mentioned phenomena could be caused in a high-frequency flyback converter. This indicates that the use of the phenomena allows us to fabricate the high-efficiency flyback converter.

Chapter 6

Analysis and design of high-frequency flyback converter

In this chapter, we design the high-frequency flyback converter considering the phenomena observed in Chapter 5. In addition, the behavior of the internal magnetic flux density is investigated under the high-frequency operation. The air-core transformer in this dissertation has several resonant frequencies in the frequency range above 10 MHz. In Chapter 5, it was found that the internal magnetic flux density was affected by the second resonant frequency when the air-core transformer was excited with a waveform including many harmonic components. The above experiment was conducted under the open condition on the secondary side of the air-core transformer. In a flyback converter, the above condition corresponds to the case when the active switch on the primary side is turned on. It is very likely that the phenomena observed in Chapter 5 will occur in the high-frequency flyback converter as well. Therefore, it is necessary to design the high-frequency flyback converter considering the phenomena.

In Section 6.1, the principle of the active clamp flyback converter is introduced. Section 6.2 investigates the operation of the high-frequency flyback converter. Through these analyses, we summarize the problem in the high-frequency operation. In Section 6.3, we improve the power conversion efficiency in the high-frequency flyback converter. In Section 6.4, we investigate the behavior of the magnetic flux density in the high-frequency flyback converter.

6.1 Active clamp flyback converter

In general, air-core transformers have a lower coupling coefficient than transformers with magnetic materials. The coupling coefficient of the fabricated air-core transformer is estimated to be 0.615 in this dissertation. The coupling coefficient of the transformer used in the flyback converter needs to be at least 0.9 or more. The transformer with a low coupling coefficient has a large leakage flux. This implies that the energy retained on the primary side increases in the flyback converter when the active switch is turned off. The retained energy is handled in the active switch as surge voltage. The surge voltage becomes large as the leakage flux increases. The large surge voltage lead to breaking the active switch. Therefore, the flyback converter with the air-core transformer needs a circuit to handle the energy due to the large leakage flux.

One such circuit topology is the active clamp flyback converter [25, 84–88]. Figure 6.1 shows the schematic of the active clamp flyback converter. The active clamp circuit consists of the clamp capacitor C_{clamp} and auxiliary switch S_{aux} for handling the energy due to the leakage flux. For details of the operation, please refer to [84]. It has been reported that this topology can improve the power conversion efficiency for the flyback converter using the transformer with the magnetic materials. However, few reports are available on the flyback converter with the air-core transformer. In particular, the detailed investigation of the behavior of the internal magnetic flux density has limited reports regardless of whether magnetic materials are used in the transformers or not. We firstly analyze the operation of the active clamp flyback converter with the air-core transformer based on the search coil voltage.

6.2 Operation analysis of high-frequency operation

Figures 6.2 and 6.3 show the schematic and photograph of the fabricated active clamp flyback converter. A SiC MOSFET (ROHM, SCT3120AL) is adopted as a active switching device and a SiC SBD (ROHM, SCS206AM) as a rectifying device. The SiC MOSFET is driven with an isolated gate driver (Silicon Labs., Si8235). The power source is generated with a DC power supply (TAKASAGO, ZX-S-400MA) and an electronic load (Keisoku Giken, LN-300C) is used as dummy load.

The settings of the experiment are described as follows. The switching frequency of S_{main} is set to be 5 MHz with the constant duty ratio. Figure 6.4 shows the measurement

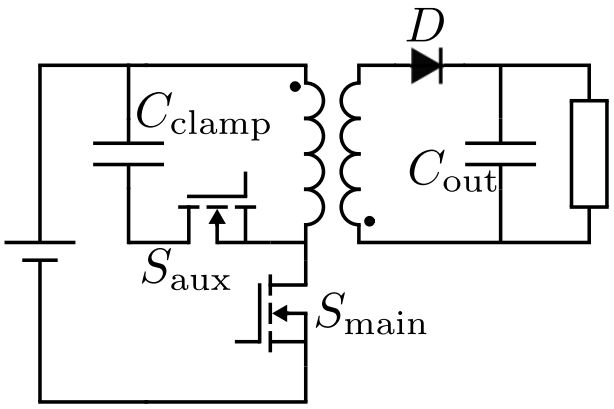

Figure 6.1: A schematic of active clamp flyback converter.

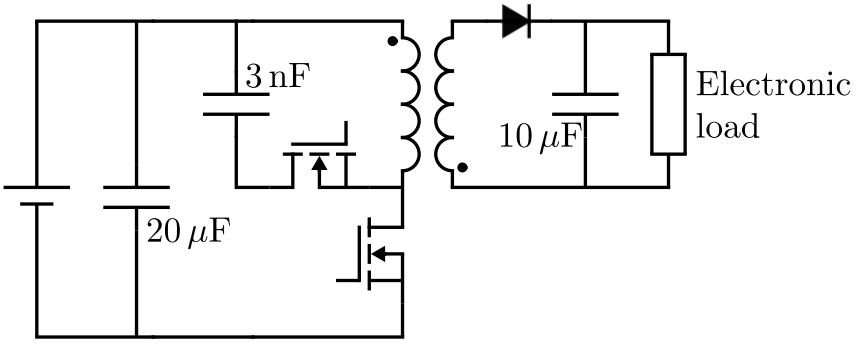

Figure 6.2: A schematic of fabricated active clamp flyback converter.

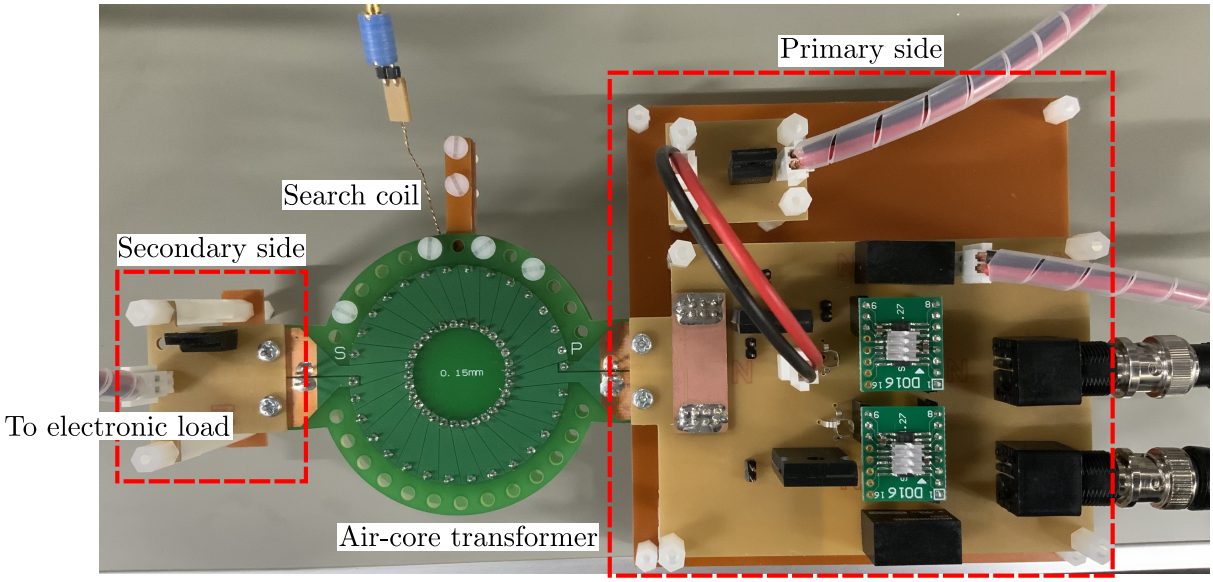

Figure 6.3: Photograph of fabricated active clamp flyback converter with air-core transformer.

points used in this study. The search coil voltage is measured for the tangential and normal components. The input and output power are measured with the DC power supply and the electronic load. The load impedance is varied from 1 to 100 Ω.

Figure 6.5 shows the output characteristics of the fabricated active clamp flyback converter operated at 5 MHz. The blue points show the input power, the red points the output power, and the green points the power conversion efficiency. The average power conversion efficiency is estimated to be about 50%. Half of the input power is lost in the converter. In general, switching losses is the main cause of loss in a power converter. However, it is not practical to assume that most of the above losses are due to the switching losses. This implies that there are causes other than switching loss that significantly decreases the power conversion efficiency. We discuss the search coil voltage in order to reveal the cause of the low power conversion efficiency.

As with Chapter 5, we discuss the search coil voltage measured at 84, 90, and 96 deg. Figure 6.6 shows the measured search coil voltage when the output load is set to be 14 Ω. It can be seen that the tangential component is dominant in the search coil voltage. In Fig. 6.6(b), it can be seen that the high-frequency oscillation occurs during the on-state of S_{main}. The DC component becomes larger as the measured point approaches the primary winding from the secondary winding. Nevertheless, the magnitude relationship of the high-frequency oscillation is reversed as with the result in Chapter 5. In Fig. 6.6(c), the high-frequency oscillation for the normal component is the largest in the search coil voltage measured at 90 deg. These are also consistent with the result in Chapter 5 and indicates that the high-frequency oscillation is caused by the second resonant frequency of the air-core transformer. The second resonant frequency of the air-core transformer is estimated to be 93.1 MHz. The frequency of the oscillation is estimated to be about 30 MHz at most. The difference implies that the second resonant frequency changes when a circuit is connected to the secondary side of the air-core transformer. From the result of the measurement of $Z_{\mathrm{PP'},\mathrm{short}}$ in Chapter 2, the frequency response of the air-core transformer changes depending on the secondary winding conditions. Therefore, we investigate the frequency response of the air-core transformer, including the secondary circuit.

Figure 6.7 shows the measurement setup of the frequency response in the air-core transformer with the secondary circuit. The frequency response is measured using an impedance analyzer (Keysight Technologies, 4294A). The output of the secondary circuit is opened or connected to a DC power supply (Matsusada, P4K-36). The DC power

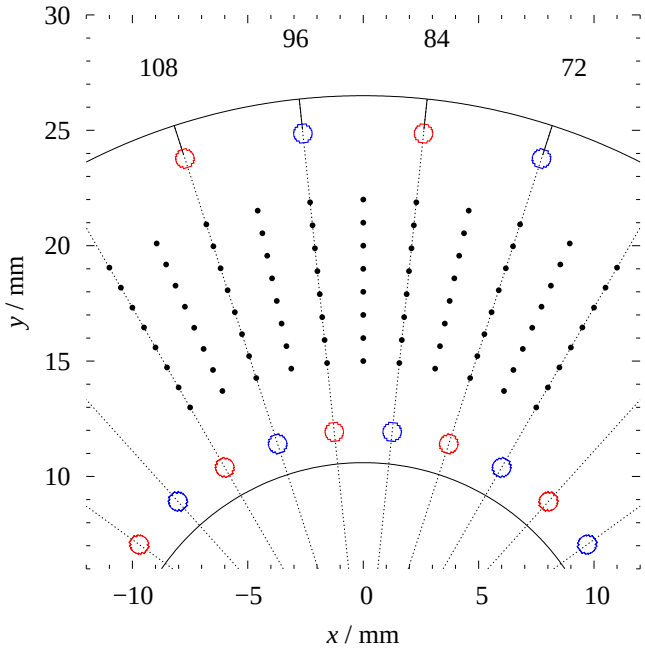

Figure 6.4: Measurement points in air-core transformer. Numbers around the circle denote angle. Blue circles denote primary side windings, and red circles denote secondary side windings.

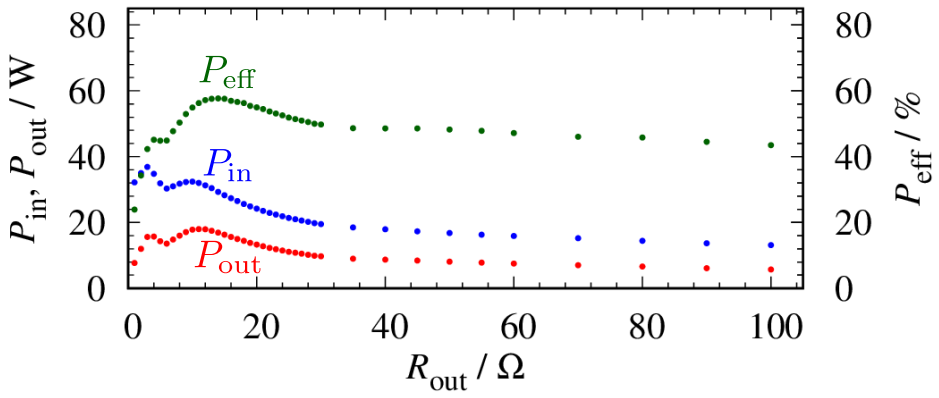

Figure 6.5: Output characteristics of fabricated active clamp flyback converter. The blue points show the input power, the red points the output power, and the green points the power conversion efficiency.

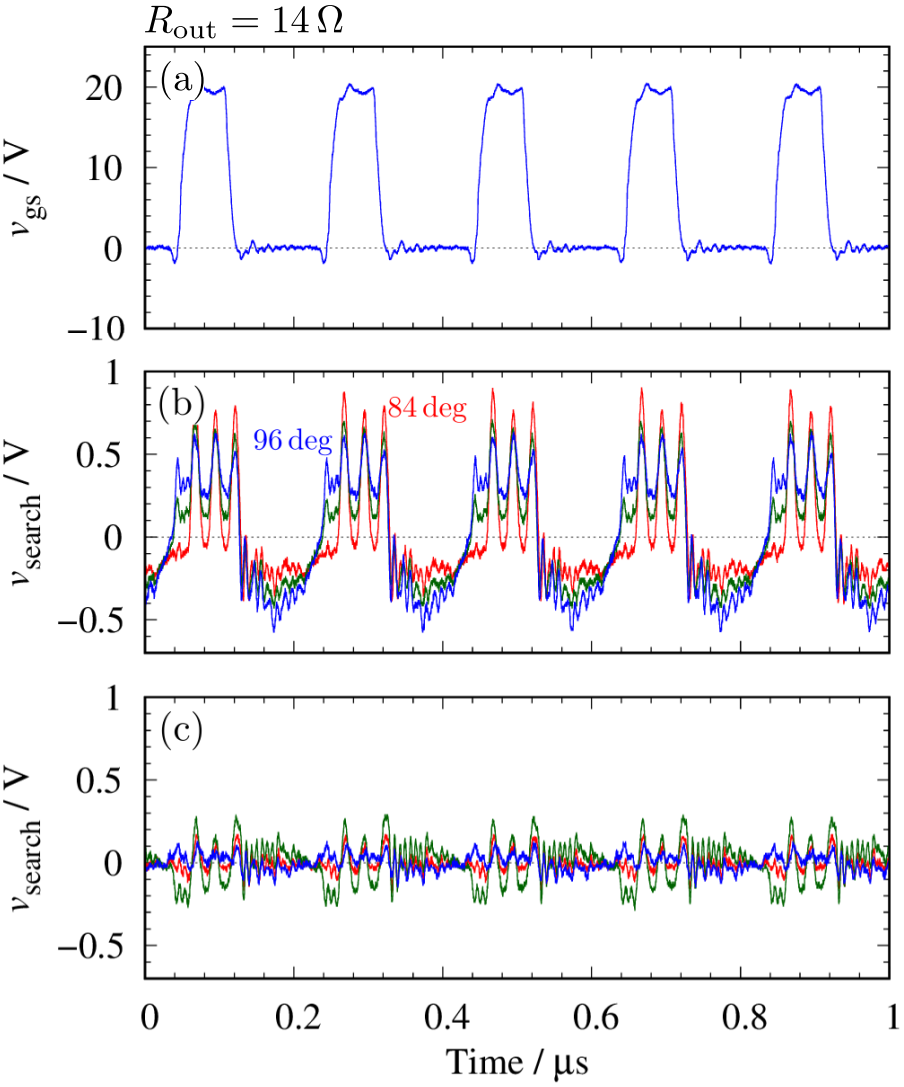

Figure 6.6: Experimentally obtained waveforms of search coil voltage:(a) gate-source voltage of S_{main}, (b) tangential component, and (c) normal component. The output load is set to $14\,\Omega$.

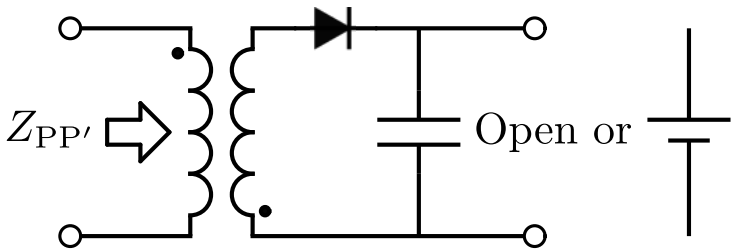

Figure 6.7: A measurement setup of frequency response in air-core transformer with secondary circuit.

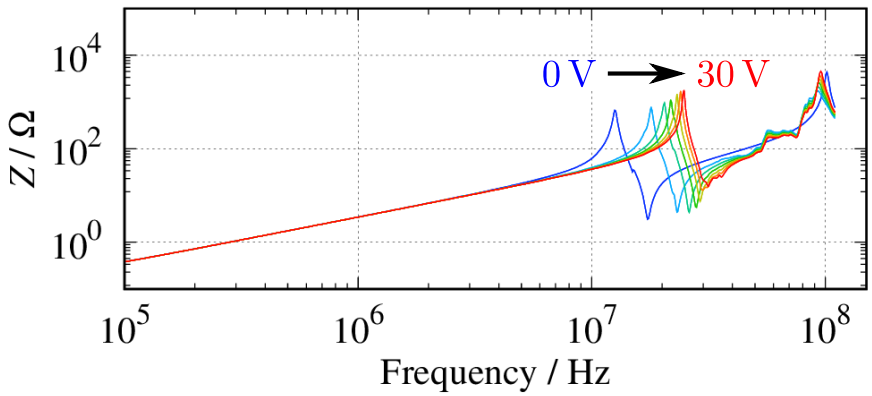

Figure 6.8: Output voltage dependence of frequency response in air-core transformer with secondary circuit.

supply mimics the output voltage of the active clamp flyback converter. The DC voltage is varied from 0 (open condition) to 30 V.

Figure 6.8 shows the output voltage dependence of the frequency response in the air-core transformer with the secondary circuit. As the output voltage increases, the resonant frequency shifts to a higher frequency. This indicates that the frequency response changes depending on the operating condition of the active clamp flyback converter. Figure 6.9(a) shows the output voltage characteristics of the fabricated active clamp flyback converter. When the output load is set to be 14 Ω, the output voltage is measured as 15 V. The frequency response is shown in Fig. 6.9(b) at that voltage and the frequency spectrum of the search coil voltage shown in Fig. 6.9(c). In Fig. 6.9(c), two peaks are confirmed. One peak corresponds to the switching frequency and another peak to the high-frequency oscillation. Compared with Fig. 6.9(b), the higher peak frequency is the same as the second resonant frequency in the order of magnitude. Therefore, the high-frequency oscillation in Fig. 6.6 is caused by the second resonant frequency.

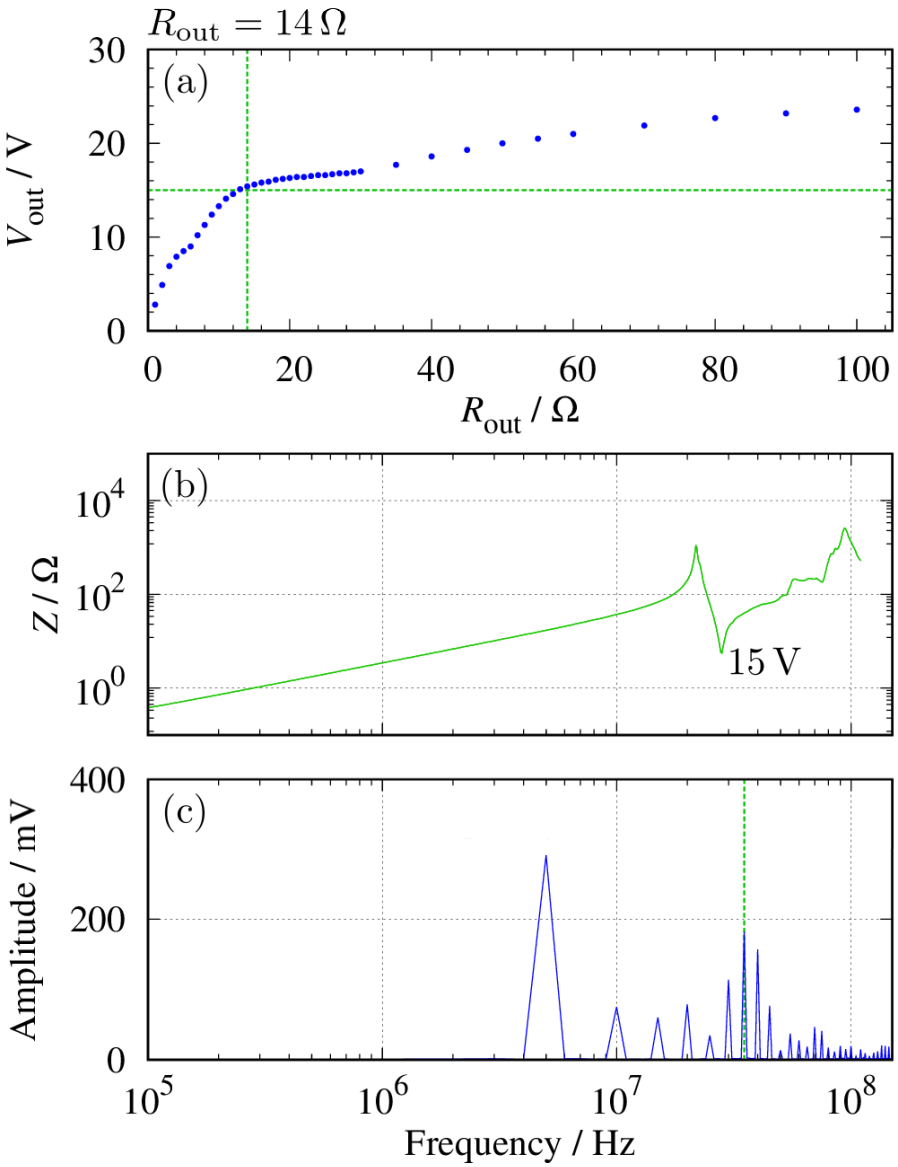

Figure 6.9: Output voltage characteristics of fabricated active clamp flyback converter, frequency response, and frequency spectrum.

Then we discuss the cause of the second resonant frequency. The second resonant frequency was changed by the secondary circuit. The secondary circuit consists of the SiC SBD and the output capacitor. Assuming that the parasitic inductance in the secondary circuit can be negligible, either the SiC SBD, the output capacitor, or both changed the second resonant frequency. The frequency of the second resonant is estimated to be about 20 MHz under the open condition. If the output capacitor changed the second resonant frequency, the inductance must be several tens of pH. That is, the output capacitor is not the cause. The SiC SBD has a junction capacitance. It is the order of several hundred pF in SCS206AM. In that case, the inductance is calculated to be several hundred nH. It is the same as the inductance of the air-core transformer in the order of magnitude. Therefore, the second resonant frequency was seemingly changed by the effect of the junction capacitance of the SiC SBD. As the output voltage increases, the second resonant frequency shifted to a higher frequency. The junction capacitance of the SiC SBD decreases as the voltage across the diode increases. When the output voltage increases, the voltage across the SiC SBD also increases because the diode has to block the output voltage and the secondary side voltage of the air-core transformer. That is, the junction capacitance of the SiC SBD decreases as the output voltage increases. The decrease in the junction capacitance leads to shifting the second resonant frequency to a higher frequency. The above description is consistent with the experiment. Therefore, the second resonant frequency depends on the junction capacitance of the SiC SBD.

Finally, we discuss the effect of the high-frequency oscillation on decreasing the power conversion efficiency based on the circuit simulation. The circuit simulation is conducted using a commercial circuit simulator (SIMetrix Technologies, SIMetrix Ver. 7.2). The equivalent circuit derived in Chapter 3 is used as the air-core transformer model. Figure 6.10 shows the simulated waveforms of the primary and secondary current in the active clamp flyback converter. The both currents oscillate during the on-state of S_{main}. The oscillations correspond to that of the search coil voltage. In particular, the oscillation on the secondary side indicates that the secondary circuit is not able to rectify the secondary current. This is seemingly why the power conversion efficiency decreases. The high-frequency oscillation of the primary current corresponds to that of the secondary current. The oscillation of the primary current can be confirmed in [89–91]. In these studies, it is highly likely that the secondary current also oscillates. However, the oscillation has been negligible because the effect has been regarded as sufficiently small due

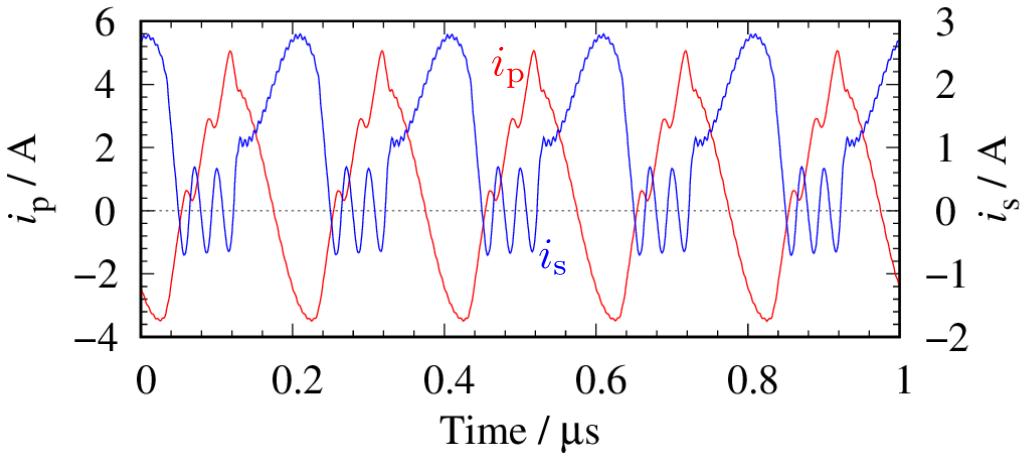

Figure 6.10: Simulated waveforms of primary and secondary current. The red line shows the primary current and the blue line the secondary current.

to the low switching frequency. As the switching frequency increases, the effect becomes larger as shown in this study. Therefore, it is necessary to consider the oscillation in order to design of high-frequency flyback converter.

6.3 Improvement of power conversion efficiency

In this section, we aim at improving the power conversion efficiency of the high-frequency flyback converter. In previous section, it was found that the secondary circuit cannot rectify the high-frequency current. The frequency of the high-frequency oscillation is estimated to be about 30 MHz. The SiC SBD is not able to rectify the current in that frequency range [56]. The frequency of the oscillation depends on the second resonant frequency in the impedance of the air-core transformer including the secondary circuit. The SiC SBD can rectify the current in the frequency range below 10 MHz. Therefore, the second resonant frequency must be shifted to below 10 MHz.

In this dissertation, we shift the second resonant frequency by adding the capacitor C_{rect} to the secondary circuit. The capacitance of C_{rect} is set to be 1 nF. Figure 6.11 shows the measurement setup of the frequency response in the fabricated air-core transformer with the modified secondary circuit. The same experiment in Section 6.2 is performed on the modified secondary circuit. Figure 6.12 shows the comparison of the frequency response with and without the capacitor C_{rect}. By adding the capacitor, the resonant frequency is shifted to a lower frequency. Figure 6.13 shows the comparison of the sim-

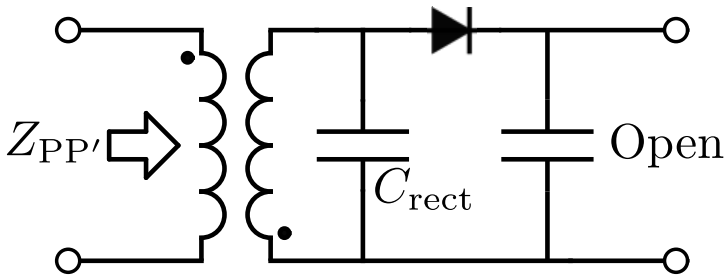

Figure 6.11: A measurement setup of frequency response in air-core transformer with modified secondary circuit.

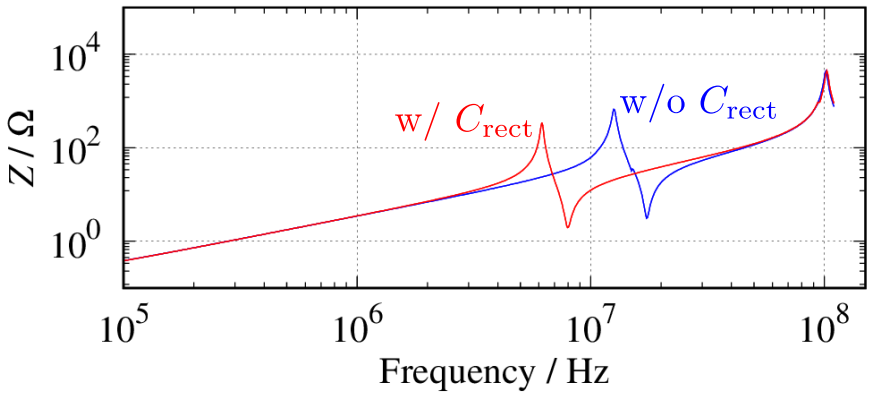

Figure 6.12: Comparison of frequency response with and without capacitor C_{rect}.

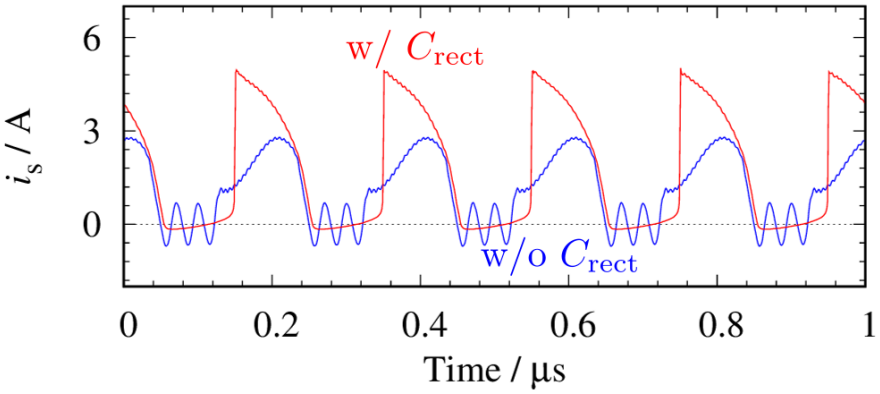

Figure 6.13: Comparison of simulated waveforms of secondary current with and without capacitor C_{rect}.

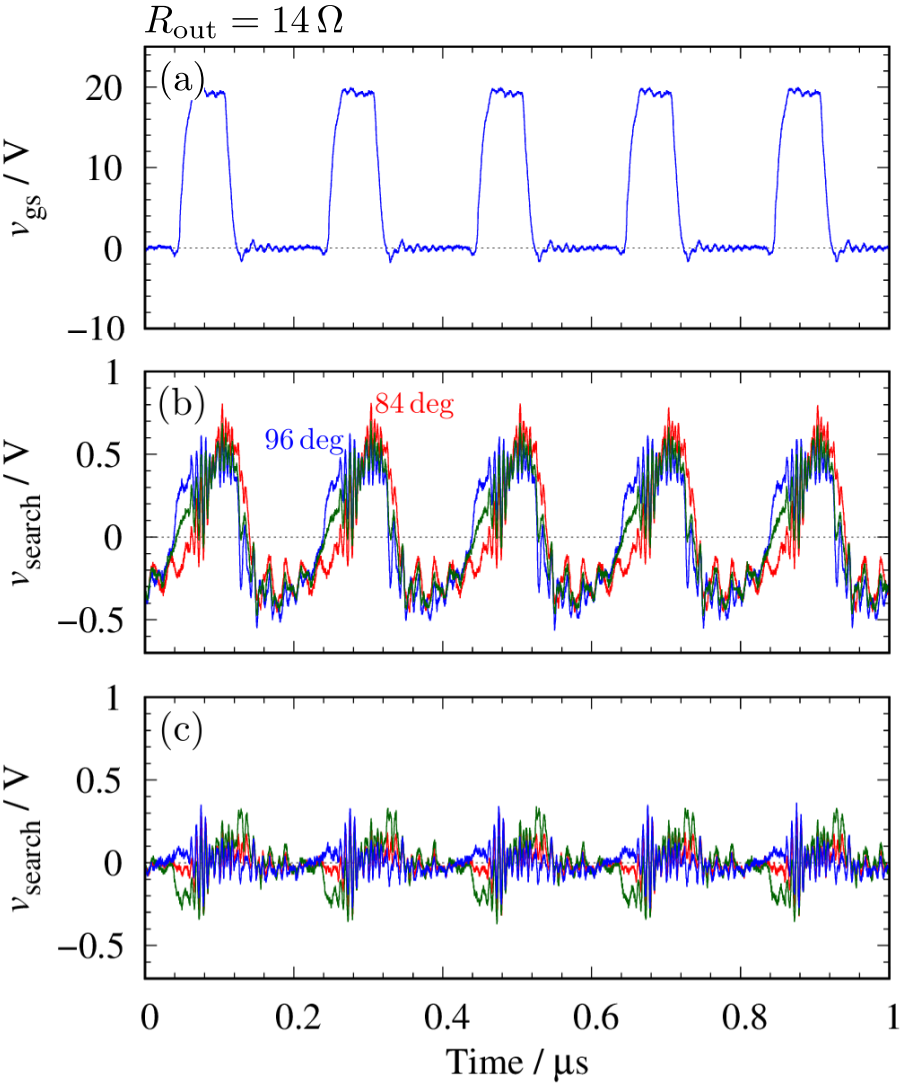

Figure 6.14: Experimentally obtained waveforms of search coil voltage in modified secondary circuit:(a) gate-source voltage of S_{main}, (b) tangential component, and (c) normal component. The output load is set to 14 Ω.

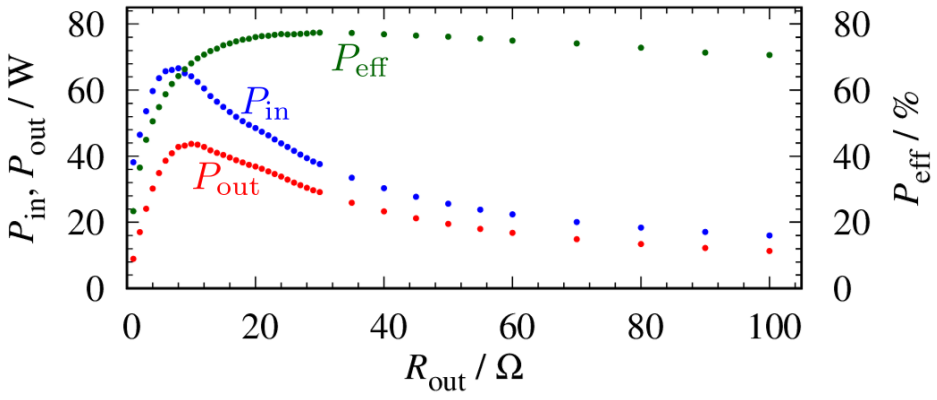

Figure 6.15: Output characteristics of fabricated active clamp flyback converter with modified secondary circuit. The blue points show the input power, the red points the output power, and the green points the power conversion efficiency.

ulated waveforms of the secondary current with and without the capacitor C_{rect}. The high-frequency oscillation disappears in the modified secondary circuit. Therefore, the proposed secondary circuit can rectify the secondary current in the high-frequency operation.

Figure 6.14 shows the experimentally obtained waveforms of the search coil voltage in the flyback converter with the modified secondary circuit. The high-frequency oscillation which oscillates at 30 MHz cannot be confirmed. It indicates that the high-frequency oscillation caused by the second resonant frequency disappears by the modified secondary circuit. However, the more high-frequency oscillation is observed. This is not seemingly caused by the second resonant frequency because the frequency is not of the same order of magnitude as it. The cause is issues in the future.

Finally, we demonstrate the 5 MHz operation active clamp flyback converter with the modified secondary circuit. Figure 6.15 shows the output characteristics of the fabricated active clamp flyback converter operated at 5 MHz. The blue points show the input power, the red points the output power, and the green points the power conversion efficiency. The power conversion efficiency is improved by adding the proposed circuit, being confirmed about above 80%. In addition, the input and output power increase. This shows the effectiveness of the proposed circuit and supports the above description.

6.4 Behavior of magnetic flux density in active clamp flyback converter

This section discusses the behavior of the magnetic flux density in active clamp flyback converter. We investigate the magnetic flux density when the output load is set to 55 Ω in addition to 14 Ω. Figures 6.16 and 6.17 show the experimentally obtained waveforms of the magnetic flux density in the active clamp flyback converter without the proposed secondary circuit. The blue line shows the magnetic flux density measured near the primary winding, the green line the magnetic flux density measured between the primary and secondary winding, and the red line the magnetic flux density measured near the secondary winding. The output load is set to 14 and 55 Ω, respectively. In (a) of Figs. 6.16 and 6.17, the magnetic flux density increases as the measured point approaches the primary winding from the secondary winding. While, the high-frequency oscillation decreases as the measured point approaches the primary winding from the secondary winding. In (b) of Figs. 6.16 and 6.17, the magnetic flux density measured at 90 deg is the largest in the normal component. These are consistent with the results of Chapter 5.

Figures 6.18 and 6.19 show the experimentally obtained waveforms of the magnetic flux density in the active clamp flyback converter with the proposed secondary circuit. The blue line shows the magnetic flux density measured near the primary winding, and the green line the magnetic flux density measured between the primary and secondary winding, and the red line the magnetic flux density measured near the secondary winding. The output load is set to 14 and 55 Ω, respectively. Compared with (a) of Figs. 6.16 and 6.17, it can be seen that the high-frequency oscillation disappears. The magnetic flux density near the secondary winding increased. In particular, the magnetic flux density was larger near the secondary winding than near the primary winding in Fig. 6.17. This indicates that the input power is efficiently transferred from the primary winding to the secondary winding via the magnetic flux. From Fig. 6.13, it can only be seen that the high-frequency oscillation, which is the cause of the decreases in the power conversion efficiency, disappeared. This shows the limit of the investigation based on the physical quantity obtained from the terminal. The power conversion efficiency is larger in 55 Ω condition than in 14 Ω condition. On the contrary the output power is larger in 14 Ω condition than in 55 Ω condition. The relationship of the power conversion efficiency can be explained based on the amplitude of the magnetic flux density for the tangential

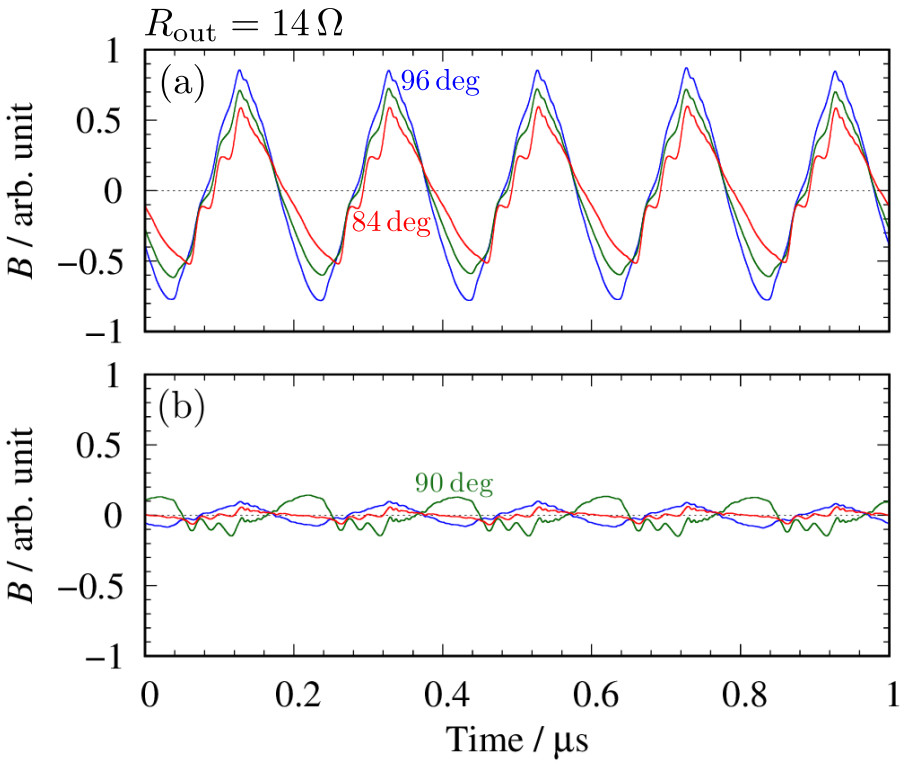

Figure 6.16: Experimentally obtained waveforms of magnetic flux density in active clamp flyback converter without proposed secondary circuit. The blue line shows the magnetic flux density measured near the primary winding, and the green line the magnetic flux density measured between the primary and secondary winding, and the red line the magnetic flux density measured near the secondary winding. The output load is set to $14\,\Omega$.

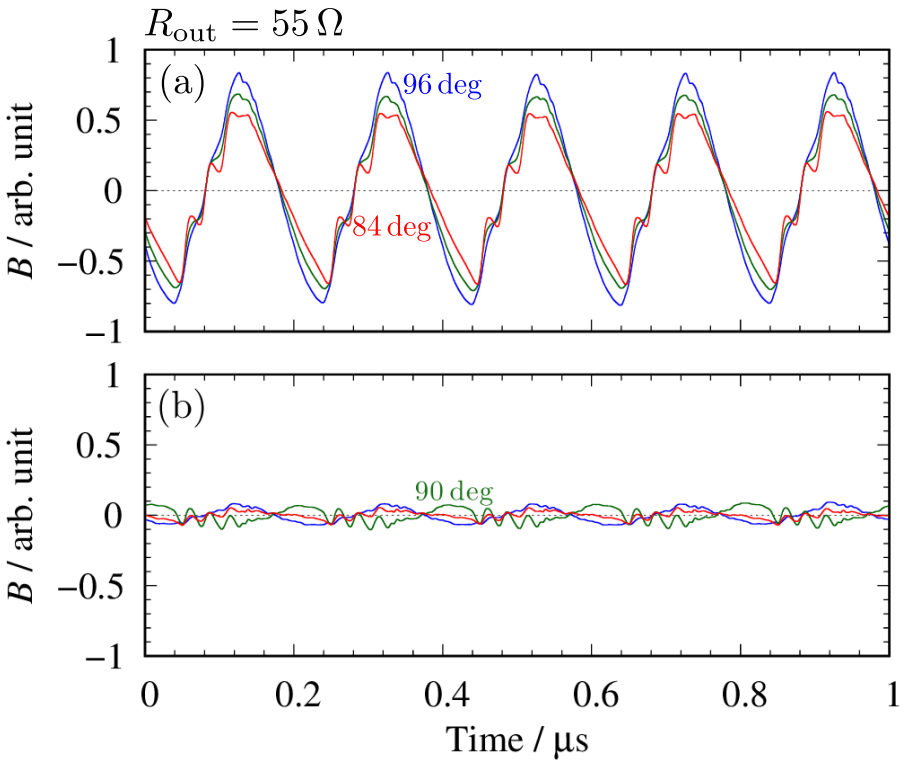

Figure 6.17: Experimentally obtained waveforms of magnetic flux density in active clamp flyback converter without proposed secondary circuit. The blue line shows the magnetic flux density measured near the primary winding, and the green line the magnetic flux density measured between the primary and secondary winding, and the red line the magnetic flux density measured near the secondary winding. The output load is set to $55\,\Omega$.

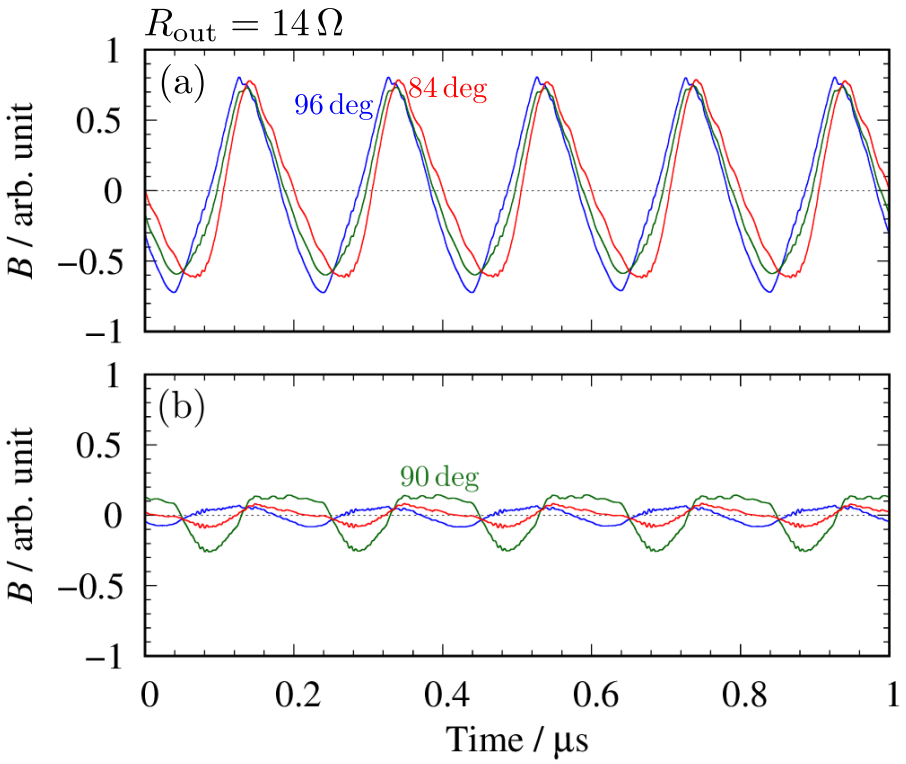

Figure 6.18: Experimentally obtained waveforms of magnetic flux density in active clamp flyback converter with proposed secondary circuit. The blue line shows the magnetic flux density measured near the primary winding, and the green line the magnetic flux density measured between the primary and secondary winding, and the red line the magnetic flux density measured near the secondary winding. The output load is set to 14 Ω.

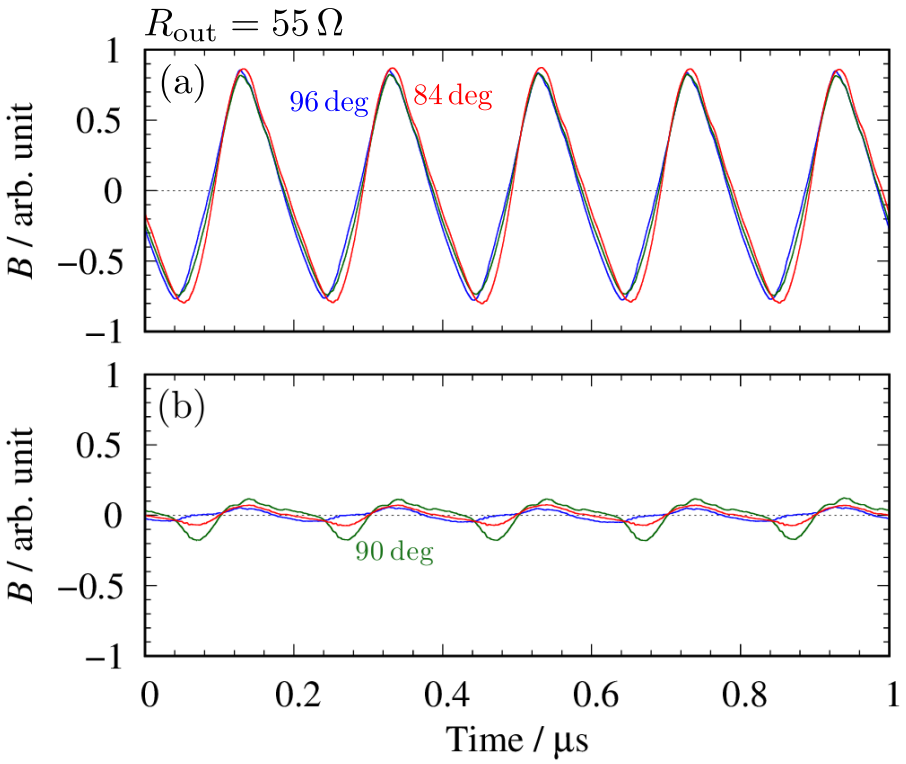

Figure 6.19: Experimentally obtained waveforms of magnetic flux density in active clamp flyback converter with proposed secondary circuit. The blue line shows the magnetic flux density measured near the primary winding, and the green line the magnetic flux density measured between the primary and secondary winding, and the red line the magnetic flux density measured near the secondary winding. The output load is set to $55\,\Omega$.

component. Regarding the output power, it is necessary to focus on another factor as well.

We focus on the phase difference between the magnetic flux density near the primary and secondary side and the rotating magnetic flux density. A transformer can only transfer AC power from the primary side to the secondary side. In general, the amount of transferred AC power depends on the phase difference between the input and output. This also holds for transformers. Let us check Figs. 6.18 and 6.19 again. The phase difference between 84 and 96 deg is larger in 14 Ω condition than in 55 Ω condition. This is why the output power is larger in 14 Ω condition than in 55 Ω condition.

Let us focus on the rotating magnetic flux density. Figure 6.20 shows the trajectory of the magnetic flux density in the active clamp flyback converter with proposed secondary circuit when the output load is set to 14 Ω. Most of the trajectories are linear, while some of them are elliptical. The elliptical trajectory indicates that the magnetic flux density rotates. The direction of rotation is periodically switched. It can be seen that the cycle of switched direction corresponds to the transformer structure. Figure 6.21 shows the comparisons of the experimentally obtained waveforms of the magnetic flux density for the tangential and the normal components in the active clamp flyback converter with the proposed secondary circuit. The blue line shows the tangential component and the red line the normal component. The output load is set to 14 Ω. It can be seen that the phase is the same between the tangential and normal component because the zero-cross point is the same in Figs. 6.21(a) and (c). On the other hand, the phase difference occurs between the tangential and normal components in Fig. 6.21(b), in which the magnetic flux density rotates. This implies that the phase difference is related to the rotating magnetic flux density.

Figure 6.22 shows the trajectory of the magnetic flux density in the active clamp flyback converter with proposed secondary circuit when the output load is set to 55 Ω. As with Fig. 6.20, most of the trajectories are linear, while some of them are elliptical. However, the area of the trajectory is smaller in Fig. 6.22 than in Fig. 6.20. Figure 6.23 shows the comparisons of the experimentally obtained waveforms of the magnetic flux density for the tangential and the normal components in the active clamp flyback converter with the proposed secondary circuit. The blue line shows the tangential component and the red line the normal component. The output load is set to 55 Ω. The phase relationship is the same as Fig. 6.21. However, the phase difference is smaller between the tangential

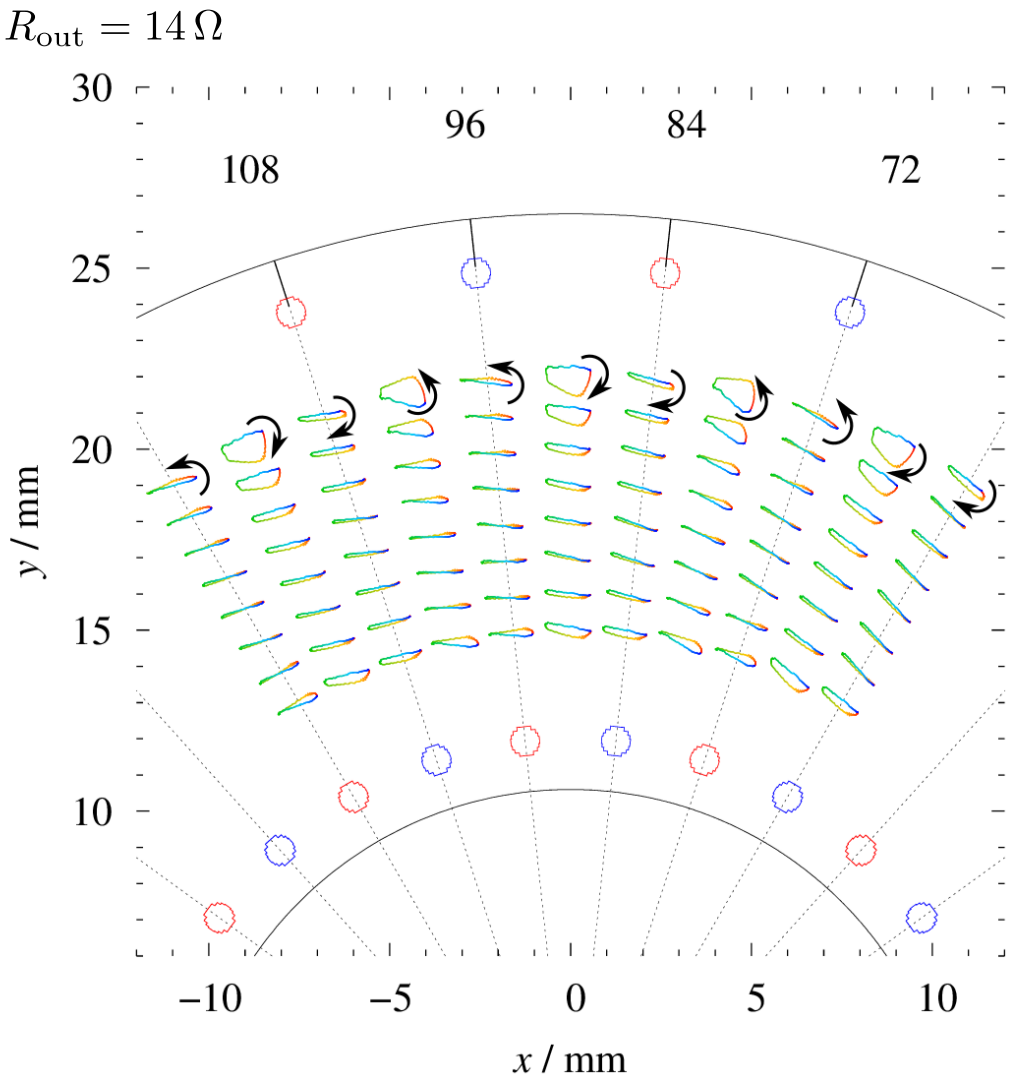

Figure 6.20: Trajectory of magnetic flux density in active clamp flyback converter with proposed secondary circuit. The output load is set to 14 Ω.

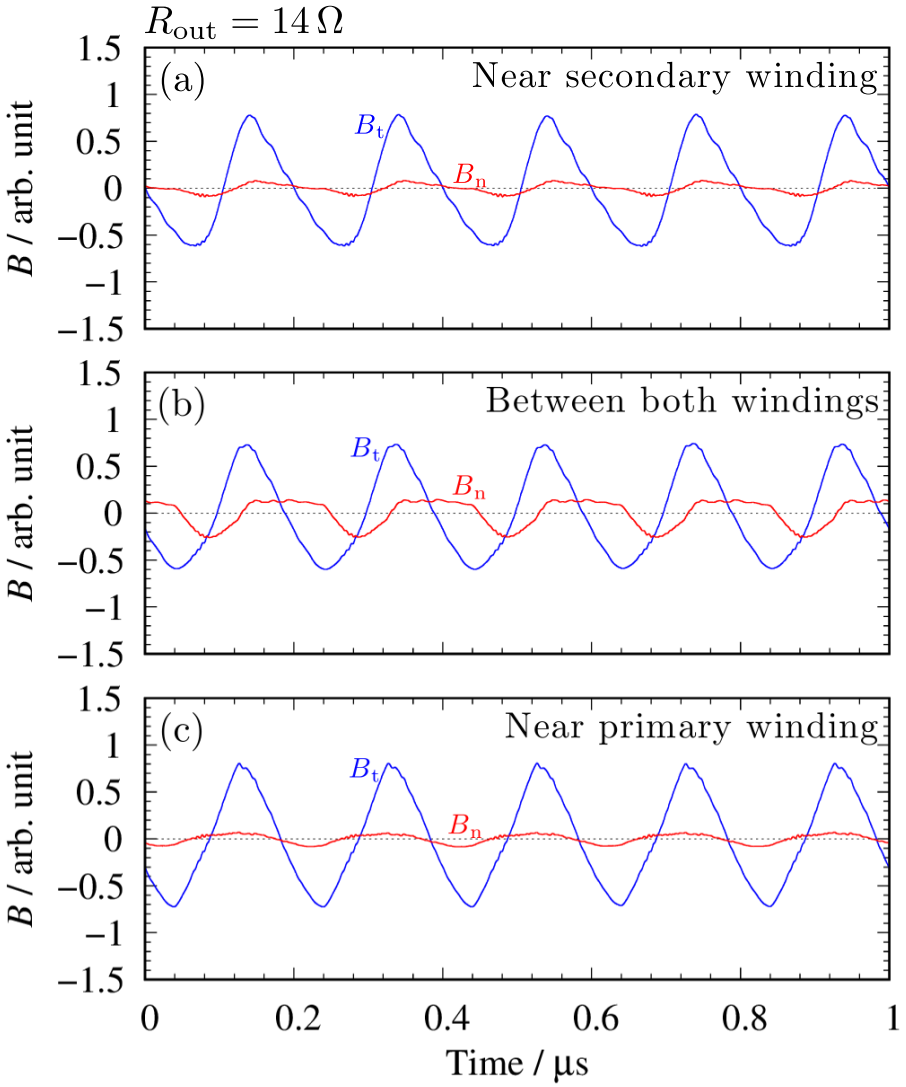

Figure 6.21: Comparisons of experimentally obtained waveforms of magnetic flux density for tangential and normal components in active clamp flyback converter with proposed secondary circuit. The blue line shows the tangential component and the red line the normal component. The output load is set to 14 Ω.

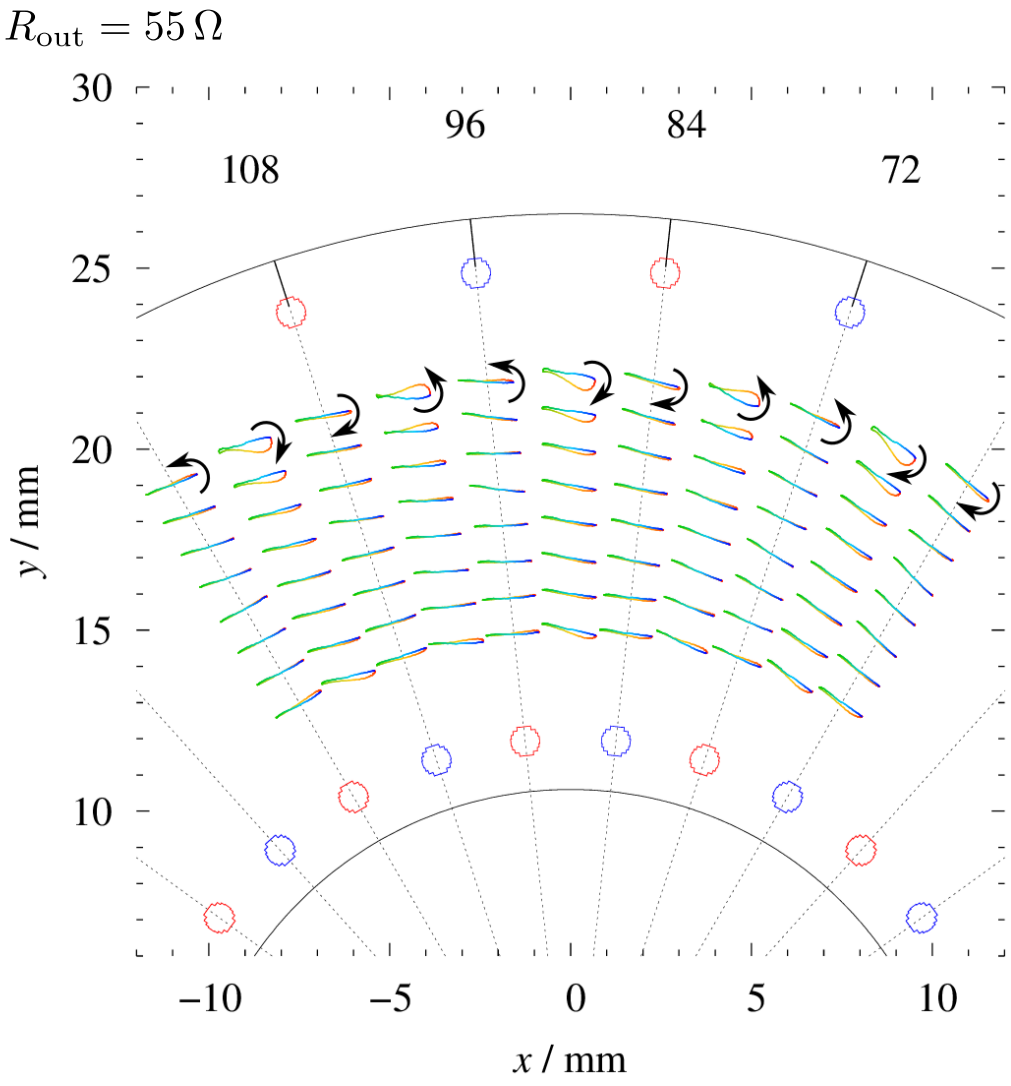

Figure 6.22: Trajectory of magnetic flux density in active clamp flyback converter with proposed secondary circuit. The output load is set to 55 Ω.

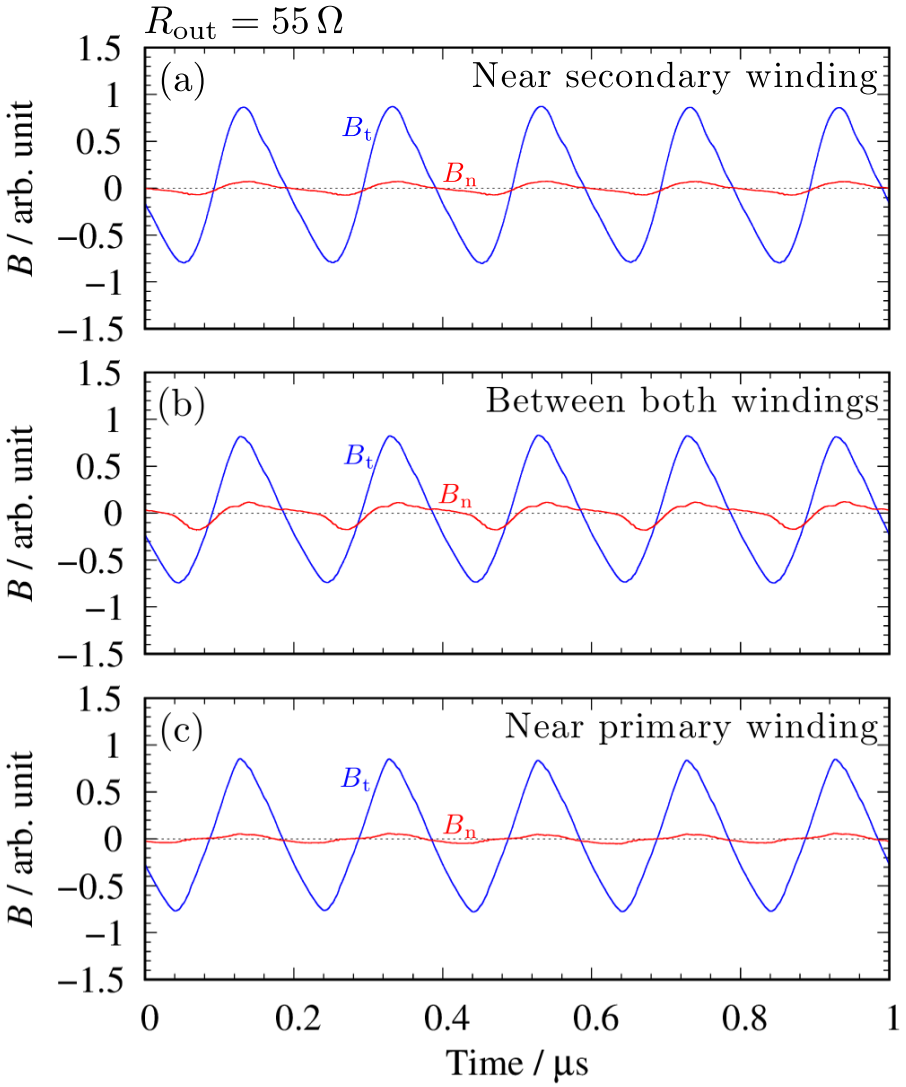

Figure 6.23: Comparisons of experimentally obtained waveforms of magnetic flux density for tangential and normal components in active clamp flyback converter with proposed secondary circuit. The blue line shows the tangential component and the red line the normal component. The output load is set to 55 Ω.

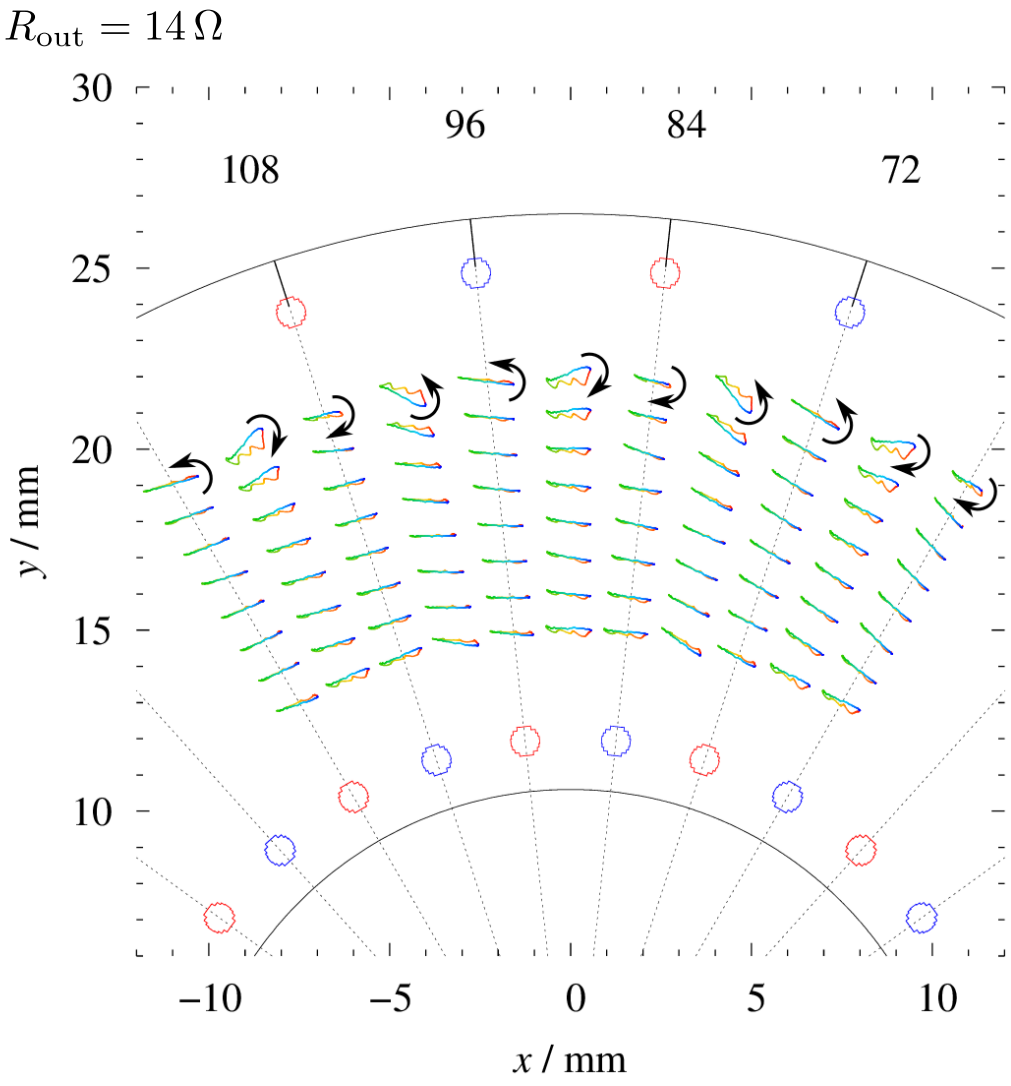

Figure 6.24: Trajectory of magnetic flux density in active clamp flyback converter without proposed secondary circuit. The output load is set to 14 Ω.

and normal components in Fig. 6.23(b) than in Fig. 6.21(b). Since the output power is larger in 14 Ω condition than in 55 Ω condition, the area of the trajectory seemingly corresponds to the amount of the output power.

In order to investigate the validity of the above hypothesis, let us look at another trajectory of the magnetic flux density. Figure 6.24 shows the trajectory of the magnetic flux density in the active clamp flyback converter without proposed secondary circuit when the output load is set to 14 Ω. As with the previous trajectories, most of the trajectories are linear, while some of them are elliptical. However, the trajectory meanders because the magnetic flux density oscillates at high frequency. As a result, the area of the trajectory becomes smaller than other trajectories. The output power in this configuration is the smallest in the depicted trajectories. Therefore, the are of the trajectory corresponds to the output power of the flyback converter. These results indicate that it is important for designing the high-frequency flyback converter to investigate the normal component, which is not dominant in the low-frequency region.

6.5 Summary

In this chapter, we designed the high-frequency flyback converter considering the phenomena observed in Chapter 5. An active clamp circuit was introduced into the flyback converter in order to deal with the energy remained in the primary side owing to the large leakage flux of the air-core transformer. The input-output characteristics of the active clamp flyback converter operated at 5MHz were measured. It was found that the power conversion efficiency was about 50%. We discussed the cause of the low power conversion efficiency. As a result, it was found that the high-frequency oscillation caused by the second resonance frequency of the air-core transformer decreased the power conversion efficiency. To improve the power conversion efficiency, the secondary circuit was modified. The second resonant frequency was shifted to the lower frequency side which can be rectified by the SiC SBD. By using the proposed circuit, the power conversion efficiency of the flyback converter was improved by more than 20%. In addition, the behavior of the internal magnetic flux density was also discussed in the high-frequency flyback converter. As a result, the rotating magnetic flux density was confirmed. It was also clarified that the area of the orbit corresponds to the output power of the converter. As of now, flyback converters have been designed based on the impedance obtained from the terminals,

i.e., the scalar quantity. For the analysis of the rotating magnetic flux, it is essential to measure and evaluate the magnetic flux density as a vector quantity. The results of this chapter suggest the possibility of taking the design theory of high frequency flyback converters to the next stage by understanding the behavior of the magnetic flux density as a vector quantity.

Chapter 7

Conclusions and future directions

This dissertation analyzed the air-core transformer for a high-frequency flyback converter. The air-core transformer was analyzed based on its frequency response, equivalent circuit, and internal magnetic flux density. In particular, the equivalent circuit and the measurement method for the internal magnetic flux density are unique to this dissertation. These methods can provide useful knowledge not only about flyback converters but also about other isolated power converters. This chapter first summarizes the contributions of each chapter, and then presents the design guidelines for air-core transformers based on them. After that, future directions are discussed.

7.1 Conclusions

In Chapter 2, we analyzed the fundamental characteristics of the fabricated air-core transformer based on its frequency response. Several resonances were confirmed in the frequency range of several tens of megahertz. These resonances strongly depended on the transformer structure, specifically, the copper coverage and the relative angle between the terminals. The inductance component, the self-inductance and the mutual inductance, did not change significantly in any of the structures. This implies that the basic function of the air-core transformer does not strongly depend on the copper coverage and the relative angle. In other words, the high- and low-frequency characteristics can be designed separately to some extent.

In Chapter 3, we constructed the high-frequency equivalent circuit of the air-core transformer based on the frequency response measured in Chapter 2. The equivalent circuit was expressed as a distributed model. That is because the frequency response

indicates that the distribution of physical quantities in the air-core transformer must be taken into account in addition to the parasitic capacitance. The equivalent circuit represented the experimental results accurately. This enables the circuit simulation in the megahertz frequency range.

In Chapter 4, we developed the method for the internal magnetic flux density distribution in the air-core transformer. From the results of Chapter 2 and 3, it is indispensable for analyzing the high-frequency characteristics of the air-core transformer to investigate the distribution of the physical quantity. In this dissertation, we focus on the internal magnetic flux density. The magnetic flux density was measured with the fabricated search coil. The internal magnetic flux density distribution was measured and analyzed when the air-core transformer was excited by a 1 MHz sinusoidal waveform. As a result, we confirmed the validity of the measurement method. In addition, the effect of the measurement equipment was discussed on the measured waveforms. In the process, the interesting high-frequency oscillation was confirmed. The proposed measurement method is expected to clarify the behavior of the internal magnetic flux density in high-frequency switching power supplies.

In Chapter 5, we analyzed the behavior of the internal magnetic flux density under high-frequency switching conditions. The magnetic flux density was measured using the method developed in Chapter 4. The interesting high-frequency oscillation appears in the magnetic flux density under high-frequency switching conditions as with Chapter 4. The high-frequency oscillation shows a different distribution from the low-frequency oscillation. This implies a change in the coupling coefficient at that frequency. The cause of the high-frequency oscillation was investigated, and it was found that the oscillation was caused by the second resonant frequency of the air-core transformer. Similar phenomena can be observed in Tesla coil. Tesla coil can transfer the energy from the primary to the secondary winding efficiently despite the low coupling coefficient. This indicates in the high-frequency flyback converter that the high-efficiency flyback converter can be fabricated by using the oscillation.

In Chapter 6, we designed the high-frequency flyback converter with the air-core transformer. The active clamp was introduced into the flyback converter in order to deal with the energy that retained on the primary side owing to the large leakage flux. The fabricated active clamp flyback converter was operated at 5 MHz and the input-output characteristics were measured. The power conversion efficiency was as low as 50%. To improve

the power conversion efficiency, we discussed the behavior of the search coil voltage. It was found that the low power conversion efficiency was caused by the second resonant frequency, which cannot be rectified by the SiC SBD. The secondary circuit was modified and the power conversion efficiency was increased by more than 20%. In addition, the behavior of the internal magnetic flux density was discussed in the high-frequency flyback converter. The rotating magnetic flux density was confirmed. It was found that the area of the trajectory corresponds to the output power of the converter. This indicates that the possibility of taking the design theory of high-frequency flyback converters to the next stage by understanding the behavior of the magnetic flux density as a vector quantity.

Based on the above discussion, design guidelines for air-core transformers are presented. The following are some of the findings of this study that are deeply related to the design of air-core transformers.

- The high-frequency characteristics can be designed by changing the structure of the air-core transformer while maintaining the basic function.
- The air-core transformer oscillates at the second resonant frequency when it is excited with a waveform including harmonic components.
- The second resonant frequency depends on the characteristics of the circuit connected to the secondary side.

When the switching frequency is in the low tens of megahertz, the high-frequency operation is limited by the high-frequency characteristics of the circuit connected to the secondary side. In the case of this dissertation, the high-frequency characteristics of the SiC SBD correspond to it. As the copper coverage is increased, the resonant frequency shifts to the lower frequency side. It can be inferred that an air-core transformer with high coverage is seemingly unsuitable for high-frequency operation. In reality, the high-frequency characteristics of an air-core transformer can be practically negligible because the semiconductor devices do not operate in the frequency range lower than the second resonant frequency. Therefore, the high-frequency characteristics of the air-core transformer can be practically negligible. This allows for a certain degree of flexibility in determining the transformer structure, such as giving priority to copper coverage and efficiency of device placement in the circuit. On the other hand, when the switching frequency is in the latter half of tens of megahertz or higher, the high-frequency characteristics of the air-core transformer cannot be negligible because it conflicts with the effect of the secondary-side

circuit. In such a case, a detailed investigation will be necessary, and this dissertation provides a clue to the investigation.

7.2 Future directions

In this dissertation, the second resonant frequency was successfully utilized by adding a capacitor to the secondary side circuit owing to the poor high-frequency characteristics of the SiC SBD. From the results in Chapter 3, the air-core transformer can be analyzed in the frequency below 10 MHz based on lumped-element circuits theory. Adding the capacitor means that the second resonant frequency is shifted to a frequency that can be handled by the theory. If the second resonant frequency is used without shifting, an analysis that takes into account the effect of wavelength is necessary. This also means that it is possible to implement a circuit that takes into account the effect of wavelength. For example, in the microwave region, a rectifier circuit using a quarter-wavelength microstrip line is used. At the second resonant frequency, the coupling of the magnetic flux density changes, and power can be transferred from the primary to the secondary side with high efficiency. Therefore, by applying these circuits, it is possible to realize a high-efficient flyback converter even using an air-core transformer with a low-coupling coefficient.

In Chapters 5 and 6, it was shown that the investigations based on the internal magnetic flux density are effective for the analysis of the high-frequency operation. In a toroidal structure, we can discuss the operation of the transformer in the low-frequency range by only the tangential component of the magnetic flux density because the normal component is not a major component. However, in the high-frequency region in which the second resonant frequency occurs, the normal component of the flux density also plays an important role because the magnetic flux density rotates. There is no way to discuss transformer operation considering the above phenomena based on the impedance obtained from the terminals. Thus, reconsidering the behavior of magnetic flux density in transformers from the viewpoint of vector quantities is an important issue in the application of high-frequency power converters.

The equivalent circuit in Chapter 3 is an LC ladder circuit, and the coupling between the primary and secondary windings is represented by the mutual inductance and the mutual capacitance. The mutual inductance and mutual capacitance represent the coupling due to the magnetic and electric fields, respectively. The equivalent circuit in this

dissertation shows the same resonance as that shown in Chapter 2, even when the magnetic coupling is set to zero and only the electric coupling is considered. This suggests that the same phenomenon occurs when a dielectric is inserted between two lines that are not coupled by a magnetic field. So far, the insulation of flyback converters has been discussed only focusing on the magnetic coupling. In high-frequency flyback converters, it is difficult to avoid the effect of the second resonant frequency. The above suggestion shows the limitation of the discussion ignoring the electrical coupling in high-frequency flyback converters. In this sense, the study in this dissertation provides an opportunity to reconsider isolation by transformers, which is an important issue for the future.

Finally, we discuss another important issue in a flyback converter. Flyback converters can easily provide multiple outputs by increasing the number of windings in the transformer. However, since the windings are mutually coupled, fluctuations in the output of one winding lead to fluctuations in the output of the other windings. This problem is called cross regulation [92–96]. Many investigations have been reported so far. Most of them are based on the impedance of the transformer. Some studies are based on magnetic circuits, but the magnetic flux is assumed to be in an ideal state. When the output fluctuates, the operating waveform contains many high-frequency components depending on the circuit conditions. The transformer would be strongly affected by the second resonant frequency shown in this dissertation depending on the frequency components. The behavior of the magnetic flux changes at that frequency as well. The method given in this dissertation allows us to investigate the cross regulation considering the above. In addition, the study will provide general knowledge on circuits including coupling. An example of a circuit with coupling is the series-parallel circuit of a power converter described in the introduction. In these respects, the methods and findings given in this dissertation are important for pushing the investigation of circuits with coupling to the next stage.

Bibliography

[1] M. Faraday, "V. Experimental Researches in Electricity," *Philosophical Transactions of the Royal Society of London*, vol. 122, pp. 125–162, 1832.

[2] F. Uppenborn, *History of the Transformer*. London; New York: E. & F. N. Spon, 1889.

[3] B. Choi, *PWM Dc-to-Dc Power Conversion*. John Wiley & Sons, Ltd, 2013.

[4] S. F. Tie and C. W. Tan, "A Review of Energy Sources and Energy Management System in Electric Vehicles," *Renewable and Sustainable Energy Reviews*, vol. 20, pp. 82–102, 2013.

[5] L. Kumar and S. Jain, "Electric Propulsion System for Electric Vehicular Technology: A Review," *Renewable and Sustainable Energy Reviews*, vol. 29, pp. 924–940, 2014.

[6] M. Pahlevani and P. K. Jain, "Soft-Switching Power Electronics Technology for Electric Vehicles: A Technology Review," *IEEE Journal of Emerging and Selected Topics in Industrial Electronics*, vol. 1, no. 1, pp. 80–90, 2020.

[7] W. A. Tabisz, M. M. Jovanovic, and F. C. Lee, "Present and Future of Distributed Power Systems," in *Proceedings of 1992 7th Annual Applied Power Electronics Conference and Exposition*, 1992, pp. 11–18.

[8] Y. Huang and C. K. Tse, "Circuit Theoretic Classification of Parallel Connected DC-DC Converters," *IEEE Transactions on Circuits and Systems I: Regular Papers*, vol. 54, no. 5, pp. 1099–1108, 2007.

[9] D. Ma, W. Chen, and X. Ruan, "A Review of Voltage/Current Sharing Techniques for Series-Parallel-Connected Modular Power Conversion Systems," *IEEE Transactions on Power Electronics*, vol. 35, no. 11, pp. 12383–12400, 2020.

[10] W. Chen, X. Ruan, H. Yan, and C. K. Tse, "DC/DC Conversion Systems Consisting of Multiple Converter Modules: Stability, Control, and Experimental Verifications," *IEEE Transactions on Power Electronics*, vol. 24, no. 6, pp. 1463–1474, 2009.

[11] T. Kimoto, "Material Science and Device Physics in SiC Technology for High-Voltage Power Devices," *Japanese Journal of Applied Physics*, vol. 54, no. 4, p. 040103, 2015.

[12] J. A. Cooper, M. R. Melloch, R. Singh, A. Agarwal, and J. W. Palmour, "Status and Prospects for SiC Power MOSFETs," *IEEE Transactions on Electron Devices*, vol. 49, no. 4, pp. 658–664, 2002.

[13] J. Millán, P. Godignon, X. Perpiñá, A. Pérez-Tomás, and J. Rebollo, "A Survey of Wide Bandgap Power Semiconductor Devices," *IEEE Transactions on Power Electronics*, vol. 29, no. 5, pp. 2155–2163, 2014.

[14] M. Ishida, Y. Uemoto, T. Ueda, T. Tanaka, and D. Ueda, "GaN Power Switching Devices," in *Proceedings of the 2010 International Power Electronics Conference - ECCE ASIA -*, 2010, pp. 1014–1017.

[15] U. K. Mishra, L. Shen, T. E. Kazior, and Y. Wu, "GaN-Based RF Power Devices and Amplifiers," *Proceedings of the IEEE*, vol. 96, no. 2, pp. 287–305, 2008.

[16] J. L. Hudgins, G. S. Simin, E. Santi, and M. A. Khan, "An Assessment of Wide Bandgap Semiconductors for Power Devices," *IEEE Transactions on Power Electronics*, vol. 18, no. 3, pp. 907–914, 2003.

[17] R. C. N. Pilawa-Podgurski, A. D. Sagneri, J. M. Rivas, D. I. Anderson, and D. J. Perreault, "Very-High-Frequency Resonant Boost Converters," *IEEE Transactions on Power Electronics*, vol. 24, no. 6, pp. 1654–1665, 2009.

[18] Z. L. Zhang, Z. Dong, X. W. Zou, and X. Ren, "A Digital Adaptive Driving Scheme for eGaN HEMTs in VHF Converters," *IEEE Transactions on Power Electronics*, vol. 32, no. 8, pp. 6197–6205, 2017.

[19] Z. Zhang and K. D. T. Ngo, "Multi-Megahertz Quasi-Square-Wave Flyback Converter Using eGaN FETs," *IET Power Electronics*, vol. 10, no. 10, pp. 1138–1146, 2017.

[20] Z. Zhang, K. Xu, Z. Xu, J. Xu, X. Ren, and Q. Chen, "GaN VHF Converters with Integrated Air-Core Transformers," *IEEE Transactions on Power Electronics*, vol. 34, no. 4, pp. 3504–3515, 2019.

[21] N. Satoh, H. Otake, T. Nakamura, and T. Hikihara, "A Flyback Converter Using Power MOSFET to Achieve High Frequency Operation Beyond 13.56 MHz," in *Proceedings of 2015 41st Annual Conference of the IEEE Industrial Electronics Society*, 2015, pp. 001376–001381.

[22] Z. Zhang, K. D. T. Ngo, and J. L. Nilles, "A 30-W Flyback Converter Operating at 5 MHz," in *Proceedings of 2014 IEEE Applied Power Electronics Conference and Exposition*, 2014, pp. 1415–1421.

[23] K. Hashimoto, T. Okuda, and T. Hikihara, "A Flyback Converter with SiC Power MOSFET Operating at 10 MHz: Reducing Leakage Inductance for Improvement of Switching Behaviors," in *Proceedings of 2018 International Power Electronics Conference - ECCE ASIA -*, 2018, pp. 3757–3761.

[24] S. Park and J. Rivas-Davila, "Isolated Resonant DC-DC Converters with a Loosely Coupled Transformer," in *Proceedings of 2017 IEEE 18th Workshop on Control and Modeling for Power Electronics*, 2017, pp. 1–7.

[25] T. LaBella, B. York, C. Hutchens, and J. S. Lai, "Dead Time Optimization Through Loss Analysis of an Active-Clamp Flyback Converter Utilizing GaN Devices," in *Proceedings of 2012 IEEE Energy Conversion Congress and Exposition*, 2012, pp. 3882–3889.

[26] X. Cheng, W. Shao, Y. Zhang, J. Zeng, and Z. Zhang, "High Frequency and High Efficiency DC-DC Converter with Sensorless Adaptive-Sizing Technique," *IEICE Electronics Express*, vol. 17, no. 3, pp. 20190719–20190719, 2020.

[27] C. Jiang, C. Chai, Y. Yang, Y. Liu, and Y. Yang, "An IAOT Controlled Current-Mode Buck Converter with RC-Based Inductor Current Sensor," *IEICE Electronics Express*, vol. 17, no. 4, pp. 20190757–20190757, 2020.

[28] C. H. Huang and C. C. Chen, "A Fast and High Efficiency Buck Converter with Switch-on-Demand Modulator for Wide Load Range Applications," *IEICE Electronics Express*, vol. 8, no. 12, pp. 963–968, 2011.

[29] P. Shamsi and B. Fahimi, "Design and Development of Very High Frequency Resonant DC-DC Boost Converters," *IEEE Transactions on Power Electronics*, vol. 27, no. 8, pp. 3725–3733, 2012.

[30] D. J. Perreault, J. Hu, J. M. Rivas, Y. Han, O. Leitermann, R. C. N. Pilawa-Podgurski, A. Sagneri, and C. R. Sullivan, "Opportunities and Challenges in Very High Frequency Power Conversion," in *Proceedings of 2009 24th Annual IEEE Applied Power Electronics Conference and Exposition*, 2009, pp. 1–14.

[31] S. Orlandi, B. A. Allongue, G. Blanchot, S. Buso, F. Faccio, C. A. Fuentes, M. Kayal, S. Michelis, and G. Spiazzi, "Optimization of Shielded PCB Air-Core Toroids for High-Efficiency DC-DC Converters," *IEEE Transactions on Power Electronics*, vol. 26, no. 7, pp. 1837–1846, 2011.

[32] W. Liang, L. Raymond, and J. Rivas, "3-D-Printed Air-Core Inductors for High-Frequency Power Converters," *IEEE Transactions on Power Electronics*, vol. 31, no. 1, pp. 52–64, 2016.

[33] H. Thanh Le, Y. Nour, A. Han, F. Jensen, Z. Ouyang, and A. Knott, "Microfabricated Air-Core Toroidal Inductor in Very High-Frequency Power Converters," *IEEE Journal of Emerging and Selected Topics in Power Electronics*, vol. 6, no. 2, pp. 604–613, 2018.

[34] Y. Qu, W. Shu, and J. Chang, "An Air-Core Coupled-Inductor Based Dual-Phase Output Stage for Point-of-Load Converters," in *Proceedings of 2018 IEEE International Symposium on Circuits and Systems*, 2018, pp. 1–4.

[35] Z. Tong, W. D. Braun, and J. M. Rivas-Davila, "Design and Fabrication of Three-Dimensional Printed Air-Core Transformers for High-Frequency Power Applications," *IEEE Transactions on Power Electronics*, vol. 35, no. 8, pp. 8472–8489, 2020.

[36] H. B. Kotte, R. Ambatipudi, and K. Bertilsson, "High-Speed (MHz) Series Resonant Converter (SRC) Using Multilayered Coreless Printed Circuit Board (PCB) Step-Down Power Transformer," *IEEE Transactions on Power Electronics*, vol. 28, no. 3, pp. 1253–1264, 2013.

[37] J. M. Rivas, O. Leitermann, Y. Han, and D. J. Perreault, "A Very High Frequency DC-DC Converter Based on a Class Φ_2 Resonant Inverter," *IEEE Transactions on Power Electronics*, vol. 26, no. 10, pp. 2980–2992, 2011.

[38] C. Rindfleisch and B. Wicht, "Efficiency Impact of Air-Cored Inductors in Multi-MHz Power Converters," in *Proceedings of 2016 18th European Conference on Power Electronics and Applications - ECCE Europe* -, 2016, pp. 1–8.

[39] T. Akagi, S. Abe, M. Hatanaka, and S. Matsumoto, "An Isolated DC-DC Converter Using Air-Core Inductor for Power Supply on Chip Applications," in *Proceedings of 2015 IEEE International Telecommunications Energy Conference*, 2015, pp. 1–6.

[40] C. Liu, D. Mandal, Z. Yao, M. Sun, J. Todsen, B. Johnson, S. Kiaei, and B. Bakkaloglu, "A 50-V Isolation, 100-MHz, 50-mW Single-Chip Junction Isolated DC-DC Converter with Self-Tuned Maximum Power Transfer Frequency," *IEEE Transactions on Circuits and Systems II: Express Briefs*, vol. 66, no. 6, pp. 1003–1007, 2019.

[41] J. Reinert, A. Brockmeyer, and R. W. A. A. De Doncker, "Calculation of Losses in Ferro- and Ferrimagnetic Materials Based on the Modified Steinmetz Equation," *IEEE Transactions on Industry Applications*, vol. 37, no. 4, pp. 1055–1061, 2001.

[42] P. L. Dowell, "Effects of Eddy Currents in Transformer Windings," *Proceedings of the Institution of Electrical Engineers*, vol. 113, no. 8, pp. 1387–1394, 1966.

[43] N. Vidal, J. M. Lopez-Villegas, and J. A. Del Alamo, "Analysis and Optimization of Multi-Winding Toroidal Inductors for Use in Multilayered Technologies," *IEEE Access*, vol. 7, pp. 93537–93544, 2019.

[44] C. R. Sullivan, W. Li, S. Prabhakaran, and S. Lu, "Design and Fabrication of Low-Loss Toroidal Air-Core Inductors," in *Proceedings of 2007 IEEE Power Electronics Specialists Conference*, 2007, pp. 1754–1759.

[45] G. Zulauf, W. Liang, and J. Rivas-Davila, "A unified model for high-power, air-core toroidal pcb inductors," in *2017 IEEE 18th Workshop on Control and Modeling for Power Electronics (COMPEL)*, 2017, pp. 1–8.

[46] S. Orlandi, B. Allongue, G. Blanchot, S. Buso, F. Faccio, C. Fuentes, M. Kayal, S. Michelis, and G. Spiazzi, "Optimization of Shielded PCB Air-Core Toroids for High Efficiency DC-DC Converters," in *Proceedings of 2009 IEEE Energy Conversion Congress and Exposition*, 2009, pp. 2073–2080.

[47] K. H. Liu and F. C. Y. Lee, "Zero-Voltage Switching Technique in DC/DC Converters," *IEEE Transactions on Power Electronics*, vol. 5, no. 3, pp. 293–304, 1990.

[48] R. J. Gutmann, "Application of RF Circuit Design Principles to Distributed Power Converters," *IEEE Transactions on Industrial Electronics and Control Instrumentation*, vol. IECI-27, no. 3, pp. 156–164, 1980.

[49] J. M. Rivas, Y. Han, O. Leitermann, A. D. Sagneri, and D. J. Perreault, "A High-Frequency Resonant Inverter Topology with Low-Voltage Stress," *IEEE Transactions on Power Electronics*, vol. 23, no. 4, pp. 1759–1771, 2008.

[50] Z. Tong, "3-D Printed Inductors and Transformer FEN Modeling," 2019. [Online]. Available: https://github.com/zikangtong/SUPER-Lab-Magnetics

[51] M. Miura-Mattausch, N. Sadachika, D. Navarro, G. Suzuki, Y. Takeda, M. Miyake, T. Warabino, Y. Mizukane, R. Inagaki, T. Ezaki, H. J. Mattausch, T. Ohguro, T. Iizuka, M. Taguchi, S. Kumashiro, and S. Miyamoto, "HiSIM2: Advanced MOSFET Model Valid for RF Circuit Simulation," *IEEE Transactions on Electron Devices*, vol. 53, no. 9, pp. 1994–2007, 2006.

[52] G. Gildenblat, X. Li, W. Wu, H. Wang, A. Jha, R. Van Langevelde, G. D. J. Smit, A. J. Scholten, and D. B. M. Klaassen, "PSP: An Advanced Surface-Potential-Based MOSFET Model for Circuit Simulation," *IEEE Transactions on Electron Devices*, vol. 53, no. 9, pp. 1979–1993, 2006.

[53] N. Phankong, T. Yanagi, and T. Hikihara, "Evaluation of Inherent Elements in a SiC Power MOSFET by its Equivalent Circuit," in *Proceedings of 2011 14th European Conference on Power Electronics and Applications*, 2011, pp. 1–8.

[54] M. Shintani, Y. Nakamura, M. Hiromoto, T. Hikihara, and T. Sato, "Measurement and Modeling of Gate–Drain Capacitance of Silicon Carbide Vertical Double-Diffused MOSFET," *Japanese Journal of Applied Physics*, vol. 56, no. 4S, p. 04CR07, 2017.

[55] T. Funaki, T. Kimoto, and T. Hikihara, "Evaluation of High Frequency Switching Capability of SiC Schottky Barrier Diode, Based on Junction Capacitance Model," *IEEE Transactions on Power Electronics*, vol. 23, no. 5, pp. 2602–2611, 2008.

[56] R. Maeda, T. Okuda, and T. Hikihara, "Analysis of Dynamic Characteristics of SiC Schottky Barrier Diodes at High Switching Frequency Based on Junction Capacitance," *Japanese Journal of Applied Physics*, vol. 57, no. 4S, p. 04FF01, 2018.

[57] J. G. Hayes, N. O'Donovan, and M. G. Egan, "The Extended T Model of the Multiwinding Transformer," in *Proceedings of 2004 IEEE 35th Annual Power Electronics Specialists Conference*, vol. 3, 2004, pp. 1812–1817.

[58] A. Dauhajre and R. D. Middlebrook, "Modelling and Estimation of Leakage Phenomena in Magnetic Circuits," in *Proceedings of 1986 17th Annual IEEE Power Electronics Specialists Conference*, 1986, pp. 213–226.

[59] W. G. Hurley and D. J. Wilcox, "Calculation of Leakage Inductance in Transformer Windings," *IEEE Transactions on Power Electronics*, vol. 9, no. 1, pp. 121–126, 1994.

[60] H. Y. Lu, J. G. Zhu, and V. S. Ramsden, "Comparison of Experimental Techniques for Determination of Stray Capacitances in High Frequency Transformers," in *Proceedings of 2000 IEEE 31st Annual Power Electronics Specialists Conference*, vol. 3, 2000, pp. 1645–1650.

[61] C. Liu, L. Qi, X. Cui, Z. Shen, and X. Wei, "Wideband Mechanism Model and Parameter Extracting for High-Power High-Voltage High-Frequency Transformers," *IEEE Transactions on Power Electronics*, vol. 31, no. 5, pp. 3444–3455, 2016.

[62] Hai Yan Lu, Jian Guo Zhu, and S. Y. R. Hui, "Experimental Determination of Stray Capacitances in High Frequency Transformers," *IEEE Transactions on Power Electronics*, vol. 18, no. 5, pp. 1105–1112, 2003.

[63] A. Keyhani, S. W. Chua, and S. A. Sebo, "Maximum Likelihood Estimation of Transformer High Frequency Parameters from Test Data," *IEEE Transactions on Power Delivery*, vol. 6, no. 2, pp. 858–865, 1991.

[64] H. Y. Lu, J. G. Zhu, V. S. Ramsden, and S. Y. R. Hui, "Measurement and Modeling of Stray Capacitances in High Frequency Transformers," in *Proceedings of 30th Annual IEEE Power Electronics Specialists Conference*, vol. 2, 1999, pp. 763–768.

[65] F. Blache, J. P. Keradec, and B. Cogitore, "Stray Capacitances of Two Winding Transformers: Equivalent Circuit, Measurements, Calculation and Lowering," in *Proceedings of 1994 IEEE Industry Applications Society Annual Meeting*, vol. 2, 1994, pp. 1211–1217.

[66] A. Schellmanns, J. P. Keradec, J. L. Schanen, and K. Berrouche, "Representing Electrical Behaviour of Transformers by Lumped Element Circuits: A Global Physical Approach," in *Conference Record of the 1999 IEEE Industry Applications Conference. 34th IAS Annual Meeting*, vol. 3, 1999, pp. 2100–2107.

[67] R. M. Foster, "A Reactance Theorem," *The Bell System Technical Journal*, vol. 3, no. 2, pp. 259–267, 1924.

[68] W. D. Cauer, "Verwirklichung Von Wechselstromwiderständen Vorgeschriebener Frequenzabhängigkeit," *Archiv für Elektrotechnik*, vol. 17, pp. 355–388, 1926.

[69] Z. Awang, *Microwave Systems Design*. Springer Singapore, 2014.

[70] R. Wang, H. F. Blanchette, M. Mu, D. Boroyevich, and P. Mattavelli, "Influence of High-Frequency Near-Field Coupling Between Magnetic Components on EMI Filter Design," *IEEE Transactions on Power Electronics*, vol. 28, no. 10, pp. 4568–4579, 2013.

[71] K. B. McEachron, "Magnetic Flux Distribution in Transformers," *Journal of the American Institute of Electrical Engineers*, vol. 41, no. 4, pp. 281–287, 1922.

[72] A. E. Kennelly and P. L. Alger, "Magnetic Flux Distribution in Annular Steel Laminae," *Transactions of the American Institute of Electrical Engineers*, vol. XXXVI, pp. 1113–1156, 1917.

[73] Y. Ohbuchi, T. Urabe, and Y. Sakurai, "Measurement of Flux Distribution in Toroidal and Multiaperture Cores," *IEEE Transactions on Magnetics*, vol. 7, no. 4, pp. 899–905, 1971.

[74] A. Moses, B. Thomas, and J. Thompson, "Power Loss and Flux Density Distributions in the T-Joint of a Three Phase Transformer Core," *IEEE Transactions on Magnetics*, vol. 8, no. 4, pp. 785–790, 1972.

[75] I. Daut and A. J. Moses, "Some Effects of Core Building on Localised Losses and Flux Distribution in a Three-Phase Transformer Core Assembled from Powercore Strip," *IEEE Transactions on Magnetics*, vol. 26, no. 5, pp. 2002–2004, 1990.

[76] S. Tumanski, "Induction Coil Sensors—A Review," *Measurement Science and Technology*, vol. 18, no. 3, pp. R31–R46, 2007.

[77] R. C. Phillips and E. B. Turner, "Construction and Calibration Techniques of High Frequency Magnetic Probes," *Review of Scientific Instruments*, vol. 36, no. 12, pp. 1822–1825, 1965.

[78] E. L. Bronaugh, "Helmholtz Coils for Calibration of Probes and Sensors: Limits of Magnetic Field Accuracy and Uniformity," in *Proceedings of International Symposium on Electromagnetic Compatibility*, 1995, pp. 72–76.

[79] K. D. Skeldon, A. I. Grant, and S. A. Scott, "A High Potential Tesla Coil Impulse Generator for Lecture Demonstrations and Science Exhibitions," *American Journal of Physics*, vol. 65, no. 8, pp. 744–754, 1997.

[80] E. M. M. Costa, "Resonance on Coils Excited by Square Waves: Explaining Tesla Transformer," *IEEE Transactions on Magnetics*, vol. 46, no. 5, pp. 1186–1192, 2010.

[81] D. G. Bruns, "A Solid - State Low - Voltage Tesla Coil Demonstrator," *American Journal of Physics*, vol. 60, no. 9, pp. 797–803, 1992.

[82] Y. Brelet, A. Houard, L. Arantchouk, B. Forestier, Y. Liu, B. Prade, J. Carbonnel, Y. B. André, and A. Mysyrowicz, "Tesla Coil Discharges Guided by Femtosecond Laser Filaments in Air," *Applied Physics Letters*, vol. 100, no. 18, p. 181112, 2012.

[83] M. Denicolai, "Optimal Performance for Tesla Transformers," *Review of Scientific Instruments*, vol. 73, no. 9, pp. 3332–3336, 2002.

[84] R. Watson, F. C. Lee, and G. C. Hua, "Utilization of an active-Clamp Circuit to Achieve Soft Switching in Flyback Converters," *IEEE Transactions on Power Electronics*, vol. 11, no. 1, pp. 162–169, 1996.

[85] N. P. Papanikolaou and E. C. Tatakis, "Active Voltage Clamp in Flyback Converters Operating in CCM Mode Under Wide Load Variation," *IEEE Transactions on Industrial Electronics*, vol. 51, no. 3, pp. 632–640, 2004.

[86] G. Spiazzi, P. Mattavelli, and A. Costabeber, "High Step-up Ratio Flyback Converter with Active Clamp and Voltage Multiplier," *IEEE Transactions on Power Electronics*, vol. 26, no. 11, pp. 3205–3214, 2011.

[87] X. Huang, J. Feng, F. C. Lee, Q. Li, and Y. Yang, "Conducted EMI Analysis and Filter Design for MHz Active Clamp Flyback Front-End Converter," in *Proceedings of 2016 IEEE Applied Power Electronics Conference and Exposition*, 2016, pp. 1534–1540.

[88] X. Huang, J. Feng, W. Du, F. C. Lee, and Q. Li, "Design Consideration of MHz Active Clamp Flyback Converter with GaN Devices for Low Power Adapter Application," in *Proceedings of 2016 IEEE Applied Power Electronics Conference and Exposition*, 2016, pp. 2334–2341.

[89] B. Zhao, G. Wang, and D. Wang, "Analysis of High Frequency Flyback Converters for High-Voltage Low-Power Applications," in *Proceedings of 2019 International Vaccum Electronics Conference* 2019, pp. 1–3.

[90] P. Alou, A. Bakkali, I. Barbero, J. A. Cobos, and M. Rascon, "A Low Power Topology Derived from Flyback with Active Clamp Based on a Very Simple Transformer," in *Proceedings of 21st Annual IEEE Applied Power Electronics Conference and Exposition*, 2006, pp. 627–632.

[91] J. Zhang, X. Huang, X. Wu, and Z. Qian, "A High Efficiency Flyback Converter with New Active Clamp Technique," *IEEE Transactions on Power Electronics*, vol. 25, no. 7, pp. 1775–1785, 2010.

[92] K. Chalermyanont, P. Sangampai, A. Prasertsit, and S. Theinmontri, "High Frequency Transformer Designs for Improving Cross Regulation in Multiple-Output

Flyback Converters," in *Proceedings of 2007 7th International Conference on Power Electronics and Drive Systems*, 2007, pp. 53–56.

[93] Chuanwen Ji and K. M. Smedley, "Cross Regulation in Flyback Converters: Analytic Model," in *Proceedings of 30th Annual IEEE Power Electronics Specialists Conference*, vol. 2, 1999, pp. 920–925.

[94] C. Ji, K. M. Smith, and K. M. Smedley, "Cross Regulation in Flyback Converters: Solutions," in *Proceedings of 25th Annual Conference of the IEEE Industrial Electronics Society*, vol. 1, 1999, pp. 174–179.

[95] Yue-quan Hu, Jun Zhang, Wei Chen, and Chau-chun Wen, "Mathematical Modeling of Cross-Regulation Problem in Flyback Converters," in *Proceedings of 2001 IEEE 32nd Annual Power Electronics Specialists Conference*, vol. 4, 2001, pp. 2072–2077.

[96] D. Maksimovic and R. Erickson, "Modeling of Cross-Regulation in Multiple-Output Flyback Converters," in *Proceedings of 14th Annual Applied Power Electronics Conference and Exposition*, vol. 2, 1999, pp. 1066–1072.

List of Publications

Journal articles

1. K. Hashimoto, T. Okuda, and T. Hikihara, "Measurement of Internal Magnetic Flux Density Distribution in Air-Core Toroidal Transformer Under High-Frequency Excitation," *Review of Scientific Instruments*, vol. 91, no. 4, p. 044703, 2020.

2. K. Hashimoto and T. Hikihara, "Equivalent Circuit of Interleaved Air-Core Toroidal Transformer Derived from Analogy with Coupled Transmission Lines," *IEICE Electronics Express*, vol. 17, no. 21, p. 20200262, 2020.

3. K. Hashimoto and T. Hikihara, "Behavior of Internal Magnetic Flux Density Distribution Under High-Frequency Switching Conditions," in preparation.

Peer-reviewed international conference proceedings

3. K. Hashimoto, T. Okuda, and T. Hikihara, "A Flyback Converter with SiC Power MOSFET Operating at 10 MHz: Reducing Leakage Inductance for Improvement of Switching Behaviors," in *Proceedings of 2018 International Power Electronics Conference -ECCE Asia -*, no. 24H1-4, Niigata, Japan, May 20–24, 2018, pp. 3757-3761.

4. K. Hashimoto, T. Okuda, and T. Hikihara, "Investigation of Effect of Stray Capacitances in Air-Core Toroidal Transformer at High-Frequency Oscillation Based on Internal Magnetic Flux Density," in *Proceedings of 2020 IEEE International Symposium on Circuits and Systems*, no. A2L-G, Online, October 10–21, 2020, pp. 1–4.

Other conference proceedings and presentations

5. K. Hashimoto, T. Okuda, and T. Hikihara, "BH-Curve Measurement of Transformer for Modeling at High Frequency Application," in *Proceedings of Technical Meeting*

on Electronic Circuits, no. ECT-017-006, Fukuoka, Japan, January 19, 2017 (in Japanese).

6. K. Hashimoto, T. Okuda, and T. Hikihara, "A Study on Origin of Oscillation of Voltage Waveforms in Flyback Converter," in *Proceedings of 2017 Taiwan and Japan Conference on Circuits and Systems*, no. 1C-6, Okayama, Japan, August 21–23, 2017.

7. K. Hashimoto, T. Okuda, and T. Hikihara, "A Study on Oscillation of Voltage Waveforms in Flyback Converter," in *Proceedings of 2017 IEE-Japan Industry Applications Society Conference*, no. 1-2, Hokkaido, Japan, August 29–31, 2017 (in Japanese).

8. K. Hashimoto, T. Okuda, and T. Hikihara, "Improvement of Output Characteristics in 10-MHz Flyback Converter with SiC MOSFET by Reduction of Leakage Inductance," in *Proceedings of The 2018 Annual Meeting of The Institute of Electrical Engineers of Japan*, no. 4-023, Fukuoka, Japan, August 29–31, 2018 (in Japanese).

9. K. Hashimoto, T. Okuda, and T. Hikihara, "Development of Measurement System for Internal Magnetic Flux Density Distribution in Transformer," in *Proceedings of the 14th Advanced Power Semiconductors Seminar*, no. P04F, Yokohama, May 21, 2019 (in Japanese).

10. K. Hashimoto, T. Okuda, and T. Hikihara, "Oscillations of Internal Magnetic Flux Density in Air-Core Transformer by High-Frequency Switching," in *The papers of Technical Meeting on Semiconductor Power Converter, IEE Japan*, no. EDD-19-073/SPC-19-159, Miyagi, November 28, 2019 (in Japanese).